12-2011

Microstructural characterization of kinked germanate olivine grains

Alex Gregory Drue
University of Nevada, Las Vegas

MICROSTRUCTURAL CHARACTERIZATION OF KINKED GERMANATE OLIVINE GRAINS

By Alex Gregory Drue

A thesis submitted in partial fulfillment

of the requirements for the

Master of Science in Geoscience

Department of Geoscience

College of Science

The Graduate College

University of Nevada, Las Vegas

December 2011

THE GRADUATE COLLEGE

We recommend the thesis prepared under our supervision by

Alex Gregory Drue

entitled

Microstructural Characterization of Kinked Germanate Olivine Grains

be accepted in partial fulfillment of the requirements for the degree of

Master of Science in Geoscience
Department of Geoscience

Pamela Burnley, Committee Chair

Michael Wells, Committee Member

Sean Mulcahy, Committee Member

Andrew Cornelius, Graduate College Representative

Ronald Smith, Ph. D., Vice President for Research and Graduate Studies
and Dean of the Graduate College

December 2011

ABSTRACT

Microstructural Characterization of

Kinked Germanate Olivine Grains

by

Alex Gregory Drue

Dr. Pamela Burnley, Examination Committee Chair
Associate Professor of Geology
University of Nevada, Las Vegas

Olivine is the most common and the weakest mineral in the upper mantle. Thus the strength of olivine controls the rheology of the earth's upper mantle. The rheology of olivine in the upper mantle has important implications for mantle flow, mountain building, and rates of isostatic adjustment. Recent experimental measurements of the flow strength of deformed olivine polycrystals have assumed a homogeneous state of stress. X-ray synchrotron diffraction experiments have implied that this assumption is not always valid. Elastic Plastic Self Consistent (EPSC) modeling offers an approach to estimating the flow strength of olivine that does not assume a homogeneous stress state. However, for EPSC models of olivine to work properly, all single crystal deformation modes must be considered. Kinking is a deformation mechanism that can be incorporated into the EPSC model to potentially improve the accuracy of the model's output relative to lattice plane diffraction measurements. For this purpose, the geometry of kink bands from deformed Mg_2GeO_4 olivine polycrystals is characterized using Electron Backscatter Diffraction (EBSD). A range of kink angles is observed from 19º to 68º. The slip system associated with the kink bands in the Mg_2GeO_4 grains is (100) [001].

ACKNOWLEDGEMENTS

My journey in the UNLV Geoscience department has been an odyssey. I would like to thank UNLV for a challenging and rewarding course work experience. There have been many great adventures from the Old Woman Mountain to the Grand Canyon to the Brookhaven National Laboratory. I thank my adviser, Dr. Burnley, for sharing a part of her vast knowledge of experimental petrology with me and also for her support concerning the research project. For data acquisition, I would like to give special thanks to Dr. Mulcahy who helped me make orientation maps and made research fun. I thank all of the members of my committee for their contributions to the project. In particular, I thank the committee for useful and informative reviews, which raised many important questions. My family has always been there for me during the course of this project and I am forever grateful.

TABLE OF CONTENTS

LIST OF TABLES

LIST OF FIGURES

CHAPTER 4

CHAPTER 1

INTRODUCTION

Global and regional tectonics are affected by the rheology of the upper mantle, thus accurate determination of mantle flow strength is of fundamental importance. The flow strength of the upper mantle in the brittle-ductile transition zone determines the extent to which the lithosphere and asthenosphere are coupled. In order to accurately model plate tectonics, an understanding of the degree of coupling is critical in order to determine the impact that ridge push, mantle convection, and slab pull have on plate motion (Bird, 1998). In subduction zones, the coupling between the slab and the overlying upper mantle directly impacts orogenies by transmitting compressive stress to the continental interior (Royden, 1993). The angle of slab dip affects the hinterland by modulating the amount stress that is applied to the mantle lithosphere. Lower slab dip angles cause thrust faulting in the hinterland, while higher slab dip angles promote extension (Royden, 1993). Slab dip is dependent upon the contrast between the flow strength of the slab compared to the upper mantle (Billen and Hirth, 2007). The flow strength of the upper mantle determines the susceptibility of the continental lithosphere to convective erosion and Rayleigh-Taylor instabilities, which can cause continental delamination, leading to bouyancy driven uplift (Karato, 2009; Wells and Hoisch, 2008). The rheology of the upper mantle also defines the depth limit for earthquakes (Mei et al., 2010). In regions with glacial activity, the flow strength of the upper mantle contributes to the isostatic rebound of the crust, resulting in normal faulting in the deglaciated regions and thrust faulting in the surrounding area that was not glaciated (Stewart et al., 2000). Geochemical

heterogeneities in the mantle have also been related to the flow strength of the mantle. Areas of the mantle with higher viscosities limit the rate of mixing and often merge together to create distinct geochemical reservoirs (Manga, 1996). The flow strength of olivine is a reasonable approximation for the flow strength of the upper mantle because olivine makes up 60% to 70% of the upper mantle (Tommasi et al., 2000). Olivine is also the weakest mineral of the upper mantle, which makes its flow strength an important limiting factor on the overall flow strength of the upper mantle (Tommasi et al., 2000).

Deformation of the mantle is complex and knowledge of the mechanisms by which olivine deforms is necessary in order to predict how the mantle will respond to a given stress. Each type of deformation mechanism has unique flow properties. Microstructural studies on deformed dunite and lherzolite samples suggest that diffusion creep and dislocation creep are important deformation mechanisms in the mantle (Karato and Wu, 1993). Deformation maps describe the conditions in the mantle that deformation mechanisms are operative, which allows the flow strength of olivine to be predicted for a variety of tectonic environments. Many deformation experiments have been done on olivine polycrystals to create flow laws to incorporate into deformation maps. Flow laws relate stress to strain for deformed polycrystals and are limited by the accuracy in which the macroscopic stress can be related to macroscopic strain for deformed polycrystals. The equation, $\dot{\varepsilon} = A_P \sigma^2 \exp[-E_k(0)/RT\ (1-(\sigma/\sigma_p)^{1/2})]$ is an example of a flow law for dislocation creep (Mei et al., 2010). The variables in the equation are defined as: $\dot{\varepsilon}$ = strain rate, A_P = olivine material constant, σ = differential stress, $E_k(0)$ = zero-stress activation energy, R = ideal gas constant, T = temperature, and σ_p = Peierls stress.

Recently, computer models of polycrystalline deformation have provided a new way

to calculate flow laws. EPSC (Elastic Plastic Self Consistent) models are used to estimate the macroscopic stress in polycrystals being deformed for *in situ* diffraction experiments. An advantage of using EPSC models to estimate macroscopic stress is that they do not assume a homogeneous or Ruess state of stress, which has been assumed by previous methods. X-ray diffraction experiments on deformed polycrystals have shown that polycrystals do not always deform under a Ruess state of stress. EPSC models are appropriate for dislocation creep and approximate plastic deformation in olivine by simulating dislocation glide. Currently, EPSC models do not accurately model the yield point for olivine in deformed polycrystals, contributing to error in the estimation of flow laws. The accuracy of the ESPC model may be improved by including additional deformation mechanisms.

Kinking is a deformation mechanism that can be approximated in EPSC simulations, which may improve macroscopic stress estimates. Kinking is a strain accommodation mechanism that allows glide to occur in grains with hard orientations (Wollmershauser et al., 2010). Furthermore, kinked grains have been observed in deformed dunite and lherzolite samples for a wide range of conditions. Research has been limited concerning the crystallographic characterization of kink bands in olivine. The purpose of this study is to characterize the geometry of kink bands to facilitate the implementation of kinking into the EPSC model, which may improve stress and strain estimates for the macroscopic deformation of polycrystals. The kink angles and active slip systems associated with kinking for fifteen grains are determined in this study.

Deformation Mechanisms in Olivine

Diffusion creep and dislocation creep contribute to creep in the upper mantle for a variety of conditions. The applicability of flow laws for these deformation mechanisms

depends on the applied stress, temperature, pressure, grain size, water content, and composition (Hirth, 2002). Dislocation glide is predicted for high stresses and temperatures below $.6T_m$, where T_m is the melting point of olivine. At temperatures in excess of $.6T_m$ in moderate stresses, diffusion contributes to dislocation creep through processes including climb and recrystallization. Diffusion creep is the rate limiting deformation mechanism at low stresses and high temperatures near the melting point of olivine. Grain size is important, particularly for diffusion creep, which requires a small grain size. The importance of water content on deformation has been recognized. For example, the addition of water lowers the activation energy for dislocation creep and expands the dislocation creep field for conditions found in the upper mantle (Wang, 2010). Figure 1.1 shows a deformation map for olivine in a mid-ocean ridge environment, that includes grain boundary sliding, which is a diffusion mechanism at high stresses.

Diffusion creep is a deformation mechanism that involves the movement of atoms in and around polycrystals from areas of high stress to areas of lower stress when a differential stress is applied (Wang, 2010). When a differential stress is applied to a crystal or polycrystal, it results in a net flow of atoms leading to deformation. Diffusion occurs at higher temperatures and lower strain rates in the mantle because it is highly dependent on thermal energy. Nabarro-Herring creep, coble creep and grain boundary sliding are three diffusion creep mechanisms observed in deformation experiments. When diffusion occurs within a grain, Nabarro-Herring creep is predominant (Heege, 2004). Nabarro-Herring creep results in a net flow of atoms away from the principle stress direction resulting in the deformation of a grain. Inter-granular diffusion occurs in coble creep (Heege, 2004). During coble creep atoms move from grain boundaries with high

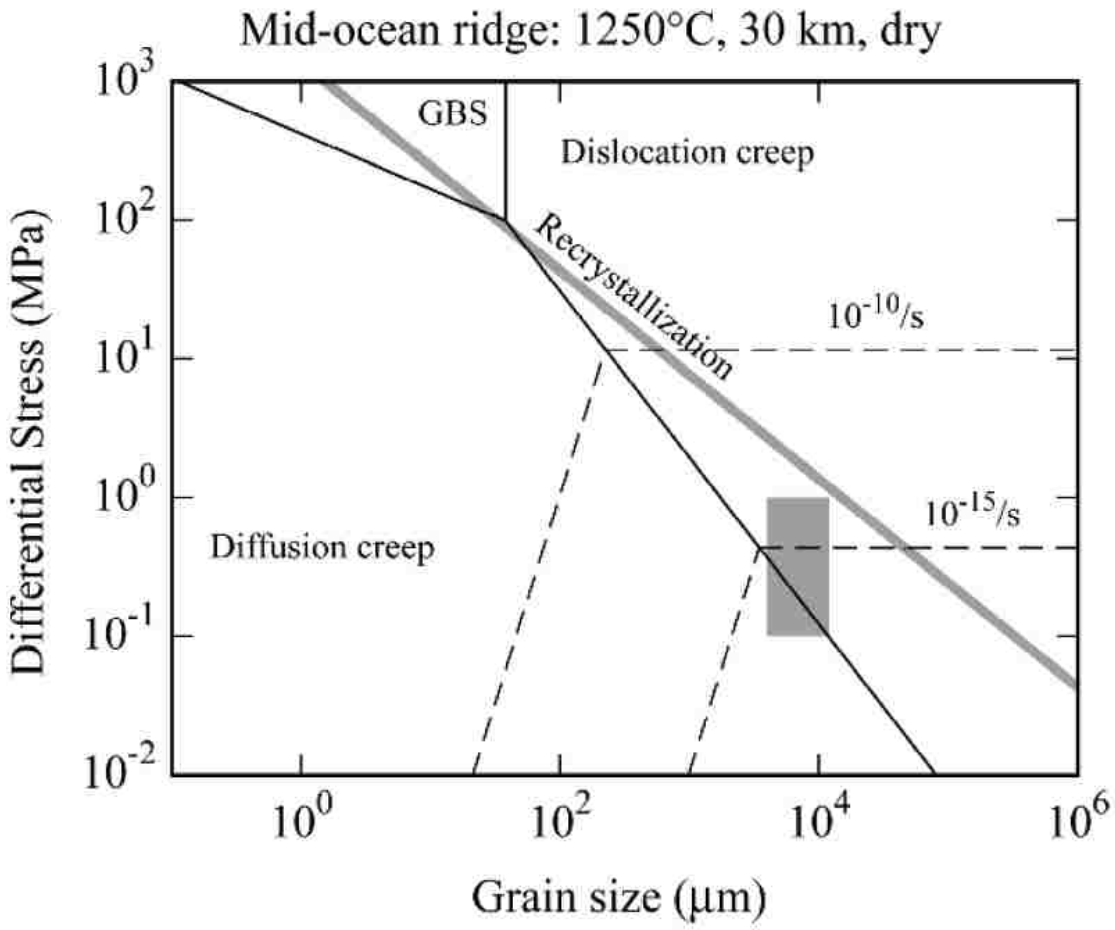

Figure 1.1. Deformation mechanisms for olivine in a mid-ocean ridge environment for conditions predicted in mantle (shaded). Hirth, 2002.

stresses to grain boundaries with lower stresses. Grain boundary sliding is a mechanism in which grains change shape and grains swap positions (Heege, 2004).

Dislocation creep is caused by the movement of linear defects or dislocations through the crystal lattice. Edge dislocations and screw dislocations are commonly observed in deformed polycrystals. Each type of dislocation is an area where the bond lengths in the crystal lattice are distorted, resulting in a simple shearing offset. A dislocation line (**u**) marks the boundary of the crystal lattice where the offset starts (Cordier, 2002). The Burgers vector (**b)** quantifies the amount of distortion that there is in the lattice spacing

from a dislocation. In an edge dislocation, **u** is perpendicular to **b** and in a screw dislocation, **u** is parallel to **b**. Figure 1.2 shows the lattice plane offset in an edge dislocation. Mixed dislocations are areas of dislocation that are that have both edge and screw components. Dislocations can be positive or negative. A Burgers vector that points in the opposite direction of another Burgers vector has the opposite sign.

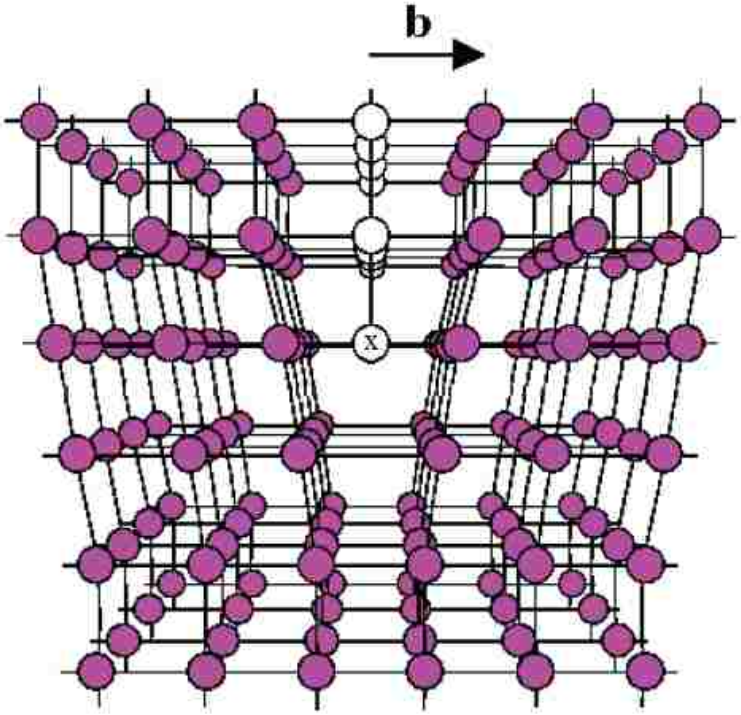

Figure 1.2. Geometry of an edge dislocation. The dislocation line (x) is parallel to the extra half plane of atoms and the Burgers vector is perpendicular to the dislocation line for an edge dislocation. Diagram adapted from Cordier, 2002.

When a differential stress is applied to a grain, macroscopic deformation occurs if there is a sufficient number of dislocations that propagate through the crystal lattice. A Frank-Read source creates new dislocations if pre-existing dislocations become pinned and form dislocation loops when a shear stress is applied (Cordier, 2002). Dislocation

loops contain new edge and screw dislocations. The most basic movement of dislocations in dislocation creep occurs when dislocations move along planes called glide planes through the crystal lattice during a process called dislocation glide (Cordier, 2002). A slip system includes a glide plane and a slip direction. According to the annotation in crystallography, a plane is bracketed by round brackets for one plane and curly brackets if there are multiple planes in a hemisphere. The slip direction is bracketed by square brackets for one direction and angle brackets for multiple directions.When multiple slip systems are active in a grain, dislocations often cross paths, which leads to the entanglement of dislocations at the intersections of slip planes (Kohlstedt, 2006). During work hardening, the entanglement of dislocations makes it harder for dislocation glide to continue and increases the amount of stress necessary to accomplish a given increment of strain.

The slip systems that operate during dislocation glide have been determined by examining deformed olivine optically and by electron microscopy (Cordier, 2002; Bai and Kohlstedt, 1992). Much of the data for the active slip systems as a function of temperature and pressure in olivine has been obtained from deformation experiments because many of the variables can be constrained (Durham et al., 2002; Ratteron et al., 2007; Bai and Kohlstedt, 1992). However, experimental data on the active slip systems has limitations. The strain rates in deformation experiments (10^{-3}/s-10^{-8}/s) are orders of magnitude faster than the actual strain rate of the mantle, which is 10^{-15}/s. Many experiments have been run at moderate stresses (Ratteron et al., 2007). Up until the recent proliferation of the multi-anvil apparatus, most experiments on the active slip systems in olivine were performed in confining pressures less than 3 GPa due to

technological limitations (Ratteron et al., 2007). Deformation experiments on olivine have been run over a wide range temperatures from ambient temperatures to temperatures above 1500º C. Experiments run below ~1000º C are commonly referred to as low temperature experiments and experiments above ~1000º C are high temperature experiments. The active slip systems in olivine change as a function of temperature and strain rate. For high temperature experiments with low strain rates, the following slip systems are active: (010) [100], (021) [100], (031) [100], (011) [100], and (001) [100] (Durinck et al., 2005). The most active slip system for olivine observed at high temperatures is (010) [100] (Dupas-Bruzek et al., 1998). Figure 1.3 shows the unit cell for fayalite in relation to the slip systems for olivine that have been observed with slip in the [100] direction.

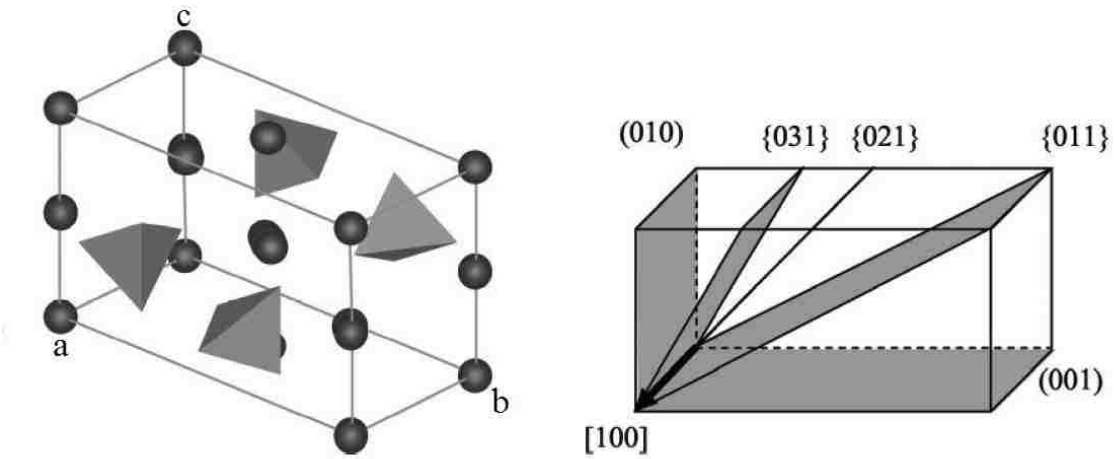

Figure 1.3. Slip systems for olivine. a) fayalite unit cell; b) slip planes with [100] slip. Diagram adapted from Cordier, 2002.

As the temperature decreases and strain rates increase, the following low temperature slip systems become active in olivine: (100) [001], (010) [001], and (110) [001] (Durinck et

al., 2005). The active slip systems at different temperatures and strain rates for deformation experiments are shown in figure 1.4. Experiments in multi-anvil apparatuses on dry olivine crystals at higher pressures have shown that the active systems in olivine are also a function of the confining pressure (Couvy et al., 2004). In deformation experiments run at confining pressures above 2.1 GPa, a transition from the (0*kl*) [100] slip systems to the (*hk*0) [001] slip systems has been observed at 7.6 GPa in experiments at similar temperatures and strain rates (Ochuchi et al., 2011; Ratteron et al., 2007). The experimental conditions in which the (0*kl*) [100] to (*hk*0) [001] transition has been observed are at differential stresses above 191 MPa and temperatures from 1220º C to 1400º C (Ochuchi et al., 2011).

Kinking is a deformation mechanism associated with dislocation creep that is often found in naturally and experimentally deformed olivine. Kinking may have an impact on the flow strength of olivine polycrystals, although little work has been done on the impact of kink band formation on deformation. Kink bands are areas of the crystal lattice in which there is a rotation of the crystal lattice relative to the original orientation for a given lattice in a plane of shear, which contains both lattice orientations (Barsoum, 1999). Figure 1.5 shows the lattice rotation relative to the original lattice plane orientation at a kink band boundary in a kinked grain. The kink boundary contains the axial plane, which is assumed to bisect the angle between the original orientation and rotated lattice planes. The applied shear stress in figure 1.5 is parallel to the glide planes. The kink band angle or rotation angle is the angle between the original and the rotated lattice plane. Kink bands form when a buckling of glide planes occurs, which results in curved glide planes in a localized area of the lattice (Barsoum et al., 1999). Within the buckled crystal lattice,

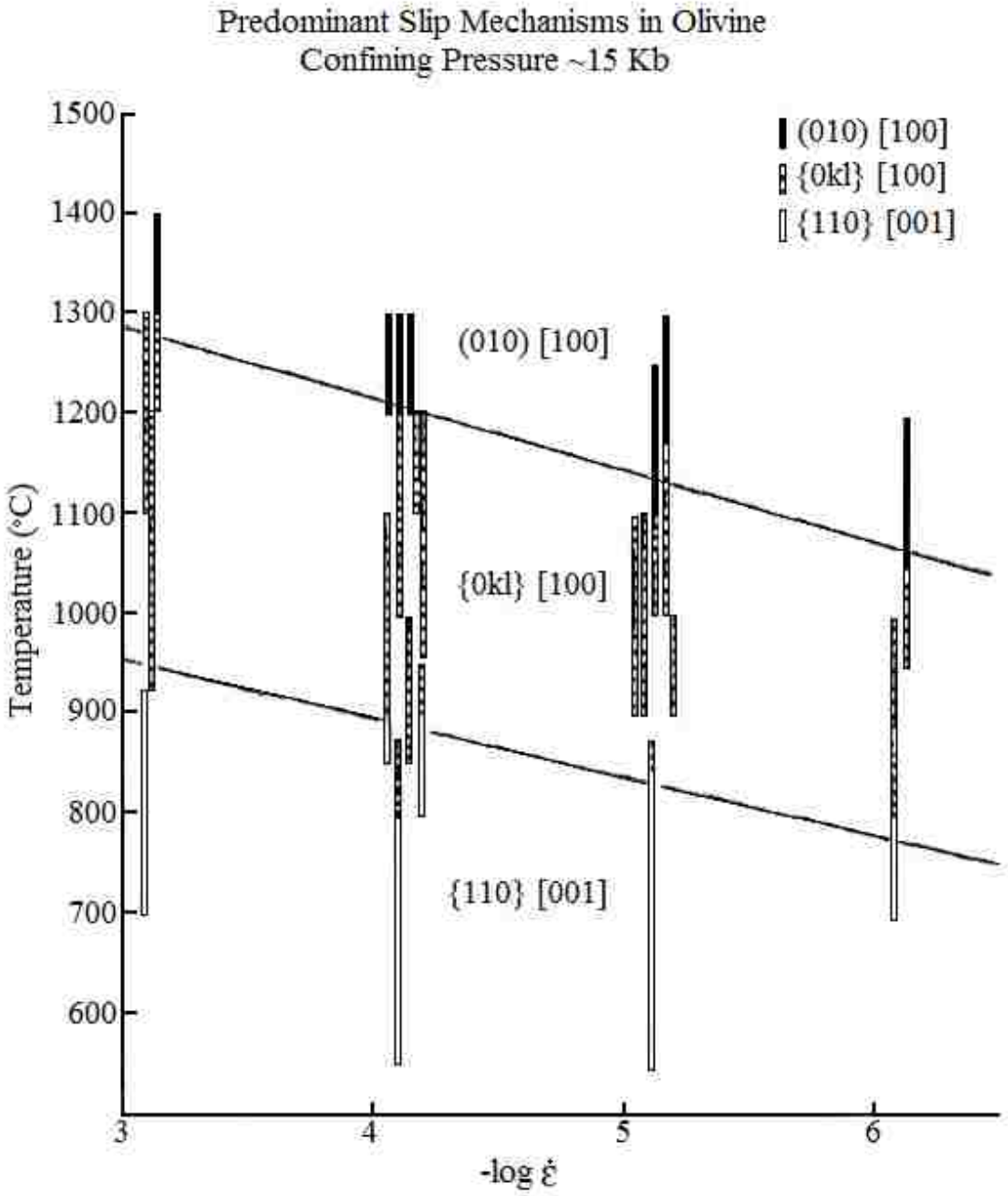

Figure 1.4. Temperatures and strain rates for predominant slip systems in olivine. The vertical bars represent the temperature range for samples that slip systems were determined for. Diagram adapted from Carter and Ave Lallemant, 1970.

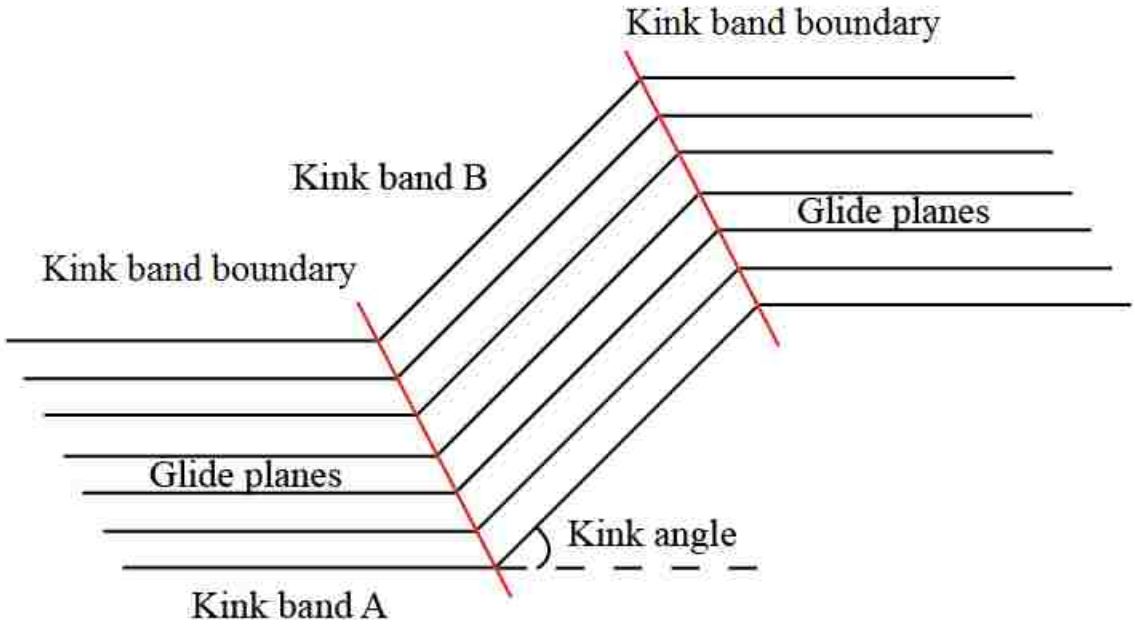

Figure 1.5. Kink band geometry

areas that have a high shear stress cause positive and negative dislocations to move in opposite directions, which leads to dislocation stacking and lattice plane offset at kink band boundaries (Barsoum et al., 1999). Barsoum et. al (1999) propose a model for kinked Ti_3SiC_2 grains in which the kink band boundary separates kink band domains with conjugate orientations that are rotated relative to the original orientation. The kink band boundary that separates the two conjugate orientations forms when the kink band boundaries from each of the conjugate orientations merge together. Figure 1.6 summarizes the stages of kink band formation according to the model proposed by Barsoum et al. (1999). Figure 1.6a shows two adjacent grains, S and P in their undeformed state. W is the part of grain P that buckles. In figure 1.6b, compression parallel to the glide planes in grain P causes the lattice to buckle into a cavity created in

grain S by glide. Dislocation arrays and dislocation walls form, which facilitates a plastic relaxation of the crystal lattice into the cavity shown in figure 1.6c. Dislocations separate from each other in areas of maximum shear stress, creating closely packed dislocation walls, which results in the formation of two new conjugate orientations with kink band boundaries at B, C, D, and F. Figure 1.6d shows the merger of kink band boundaries D and C, eliminating the original orientation. When the kink band boundaries merge, delamination cracks may form, separating the new kink band boundary

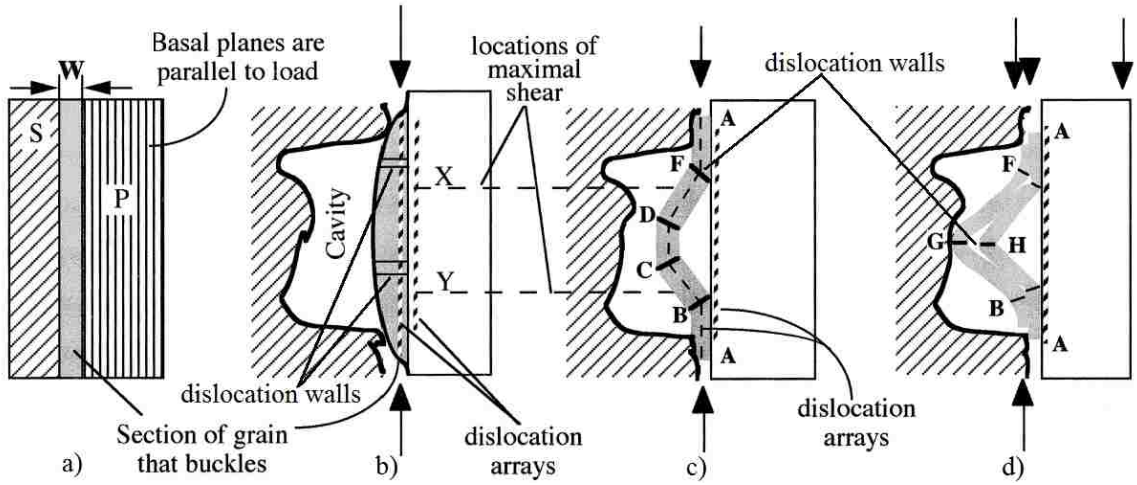

Figure 1.6. Stages of kink band formation. a) grain P and S before deformation; b) cavity formation in grain S and buckling of glide plane in grain P; c) plastic relaxation of grain S into cavity forming kink bands; d) merger of kink band boundaries forming adjacent conjugate kink band. Barsoum, 1999.

into two sections (G and H).

Naturally formed kink bands have been observed in ultramafic xenoliths from basalts and kimberlites, which are often fragments from the mantle. Not all ultramafic xenoliths are representative of actual clasts from the mantle and careful attention must be given to the texture of the xenoliths. Kinked olivine grains have also been observed in cognate and

cumulate xenoliths that are formed directly from the alkali basalt (Mercier and Nicolas, 1975). Xenoliths with a metamorphic and tectonic texture are hypothesized to be fragments of the mantle (Mercier and Nicolas, 1975). Numerous geologic environments yield basalts with xenoliths containing kinked olivine grains. These environments include hotspots, back-arcs, and rifts (Baldridge, 1979; Bjerg et al., 2004; Mercier and Nicolas, 1975). Oceanic crust and upper mantle material is often exposed in areas with allochthon sequences in ophiolite belts, which provides an additional source of xenoliths with kinked grains (Chernysov, 2005).

Mantle xenoliths with a variety of compositions and metamorphic textures contain kinked olivine grains. Kinked grains are most commonly found in lherzolite, harzburgite, and dunite xenoliths. Three metamorphic textures that are found in the mantle xenoliths are protogranular, porphyroclastic, and equigranular (Mercier and Nicolas, 1975). Kinked grains have been reported in all of metamorphic textures in mantle xenoliths. The protogranular texture has a coarse grain size with grains around 4 mm with curvilinear boundaries. The porphyroclastic texture shows more deformation with elongated porphyroclasts that can be up to 10 mm surrounded by a matrix of fine grained recrystallized polygonal neoblasts that are .5 mm. The porphyroclasts are often kinked and kinked grains occur in the porphyroclastic texture more often than in the other textures. The equigranular texture is a fine grained recrystallized texture with grains up to .7 mm that have straight boundaries that converge at triple points. Equilibration temperatures and pressures have been estimated for some porphyroclastic xenoliths containing kinked grains. Temperature estimates for the xenoliths range from 830º C to 1300º C, while the pressure estimates for the xenoliths vary from 10 kbar to 66.4 kbar

(Bjerg et al., 2004; Chernysov, 2005; Kopylova et al.,1999).

Kink bands have been observed in olivine and Mg_2GeO_4 olivine deformed in a wide range of experimental conditions for constant strain and creep experiments. Dry and wet experiments have produced kinked grains. Many different combinations of temperatures and strain rates have been used for deformation experiments on olivine that have produced kinked grains. Kinking has been observed in low temperature experiments below 1000º C and in high temperature experiments up to 1600º C. Strain rates for deformation experiments are typically from 10^{-3}/s to 10^{-8}/s.

Kinking contributes to deformation when both high and low temperature slip systems are active. The slip systems for kinking are the same for naturally and experimentally deformed samples. Both types of deformed samples show the high temperature to low temperature range for the slip systems associated with kinking. In the naturally deformed samples with kink bands, slip has been observed in (0*kl*) with most slip in (010) and (001) for samples deformed at high temperatures (Chernysov, 2005; Mercier and Nicolas, 1975). Natural samples estimated to have been deformed in lower temperatures show lattice slip in (100) and (110) (Mercier and Nicolas, 1975). The [100] slip direction for kinking is predominant at high temperatures and [001] slip is common in lower temperatures. For the kink bands found in experimental samples at high temperatures, kink band rotation is also in (0*kl*) along [100] with a preference for (010) [100] (Ave Lallemant, 1985; Carter and Ave Lallemant, 1970; Nicolas et al., 1973). In lower temperatures, rotation occurs in the (*hk*0) [001] slip system most commonly (Carter and Ave Lallemant, 1970; Nicolas et al., 1973). Most kinked grains from the experimental studies have shown slip on (110) and (010) (Carter and Ave Lallemant, 1970; Nicolas et

al., 1973). The slip systems that kinking has been observed on are summarized in table 1.1.

Table 1.1. Slip systems associated with kinking

Slip System for Kinking	Experimental Conditions
(100) [100], (010) [100], (010) [001]	T > 1000, P < 3 GPa, moderate strain rates
(110) [001], (010) [001]	T < 1000, P, < 3 GPa, moderate strain rates

Source: Data from Ave Lallemant, 1985; Carter and Ave Lallemant, 1970.

The average kink angles were measured for kinked olivine grains from eight deformed samples by Ave Lallemant (1985). The observed kink angles are: 8.54º, 5.38º, 7.04º, 5.79º, 44.73º, 13.84º, and 21.44º. The macroscopic strain for the samples with kinked grains varies from 16.7% to 58.5%.

At higher temperatures when diffusion processes start to contribute to the creep of olivine, climb and recrystallization become important deformation mechanisms in olivine (Kohlstedt, 2006). Climb is the process when edge dislocations change glide planes by moving up or down in the crystal lattice. A screw dislocation changes glide planes in a process known as cross-slip. Climb is an especially important deformation mechanism because climb helps to free dislocations that are entangled, promoting glide. Recrystallization has been observed in deformed and natural polycrystals. New grains form during recrystallization by subgrain rotation and grain boundary migration in order to reduce strain energy (Kaminski and Ribi, 2001). During subgrain rotation, the dislocation density becomes higher in a localized areas within a grain, which causes dislocation stacking and the formation of new grains that are free of strain (Kaminski and

Ribi, 2001). Grain boundary migration occurs when the grain boundaries of grains with low strain energy move into grains with a higher strain energy (Kaminski and Ribi, 2001).

Deformation Experiments and Macroscopic Stress Estimation

Understanding the relationship between stress and strain to create flow laws to model creep in the upper mantle is complicated by the fact that natural mantle samples do not reliably record all of the necessary variables in a flow law. The elastic constants for olivine are known. The temperature and pressure of equilibration can be determined using well established techniques of geothermobarametry. The shear strain experienced by naturally deformed mantle samples can be determined using kinematic techniques if there is a finite strain marker, however finite strain markers can be difficult to find in mantle xenoliths (Warren et al., 2008). Experimental petrologists are also currently working to create a lattice preferred orientation (LPO) model that relates LPOs observed in naturally deformed samples to shear strain by comparing the LPOs with experimental LPOs for given shear strains (Warren et al., 2008). There are no reliable techniques to determine the stress that naturally deformed polycrystals experienced during deformation, which has made it necessary to conduct deformation experiments on olivine polycrystals to constrain the stress in olivine polycrystals during deformation to relate stress to strain.

In deformation experiments, the known variables are typically confining pressure, temperature, strain rate, macroscopic strain, and stress. In order to determine the flow strength of olivine at a given temperature and pressure, the macroscopic stress supported by a sample must be determined for a known strain rate. There are numerous techniques for estimating the macroscopic stress including load cell measurements, dislocation density estimates, and most recently, direct estimates from lattice plane strain

measurements using x-ray diffraction. Depending on the type of confining medium, stress can be more or less accurately determined using an external load cell (Tullis and Tullis, 1986). In apparati with a solid confining medium the accuracy of the stress estimates is adversely affected because the solid medium takes up some of the force that is applied to the sample leading to erroneously high stress estimates. Some exploratory work has been done on relating the dislocation density in polycrystals to the applied stress. For stress estimates based on dislocation density, the dislocation density in a polycrystal is measured before and after a deformation experiment to make a stress estimate assuming a Reuss or homogeneous state of stress (Wang et al., 1988). The advantage of dislocation density stress estimates is that an *in situ* estimate of stress is made avoiding the error involved in using a load cell. One of the disadvantages of dislocation density estimates is that estimates are biased toward dislocation densities at peak temperature and pressure conditions (Wang et al., 1988). The density of dislocations can also vary from grain to grain, depending on orientation, which makes it necessary to obtain density measurements from a large number of grains to obtain a statistically reliable average (Wurzner et al., 2010).

Recently, the use of multi anvil apparati has become more widespread in deformation studies. Anvil designs allow *in situ* stress estimates to be made using x ray diffraction lattice plane strain data. The rotational Drickamer apparatus and the D-DIA apparatus are are both used. The D-DIA apparatus is a modified DIA apparatus that is used for deformation experiments at synchrotron sources. The DIA is a cubic multi-anvil apparatus with six anvils, four of which are arranged in an array that is in a plane perpendicular to the compression axis (Durham et al., 2002). These four anvils are

attached to wedge shaped thrust blocks. The two other anvils, which deform the top and bottom of the cube act parallel to the direction of compression and are attached to guide blocks that are designed to transmit stress to the thrust blocks (Figure 1.7a). During pressurization, a hydraulic ram drives the guide blocks together, pushing the anvils inward as the rams advance. The DIA apparatus produces a hydrostatic pressure up to 15 GPa (Durham et al., 2002). The D-DIA apparatus has two more rams that are incorporated into the upper and lower guide blocks (Figure 1.7b). These rams are independent of the rams that drive the guide blocks together and allow a differential stress to be generated for deformation experiments (Durham et al., 2002). The D-DIA apparatus is capable of generating strain rates from $2x10^{-2}$/s to $2x10^{-7}$/s (Durham et al., 2002).

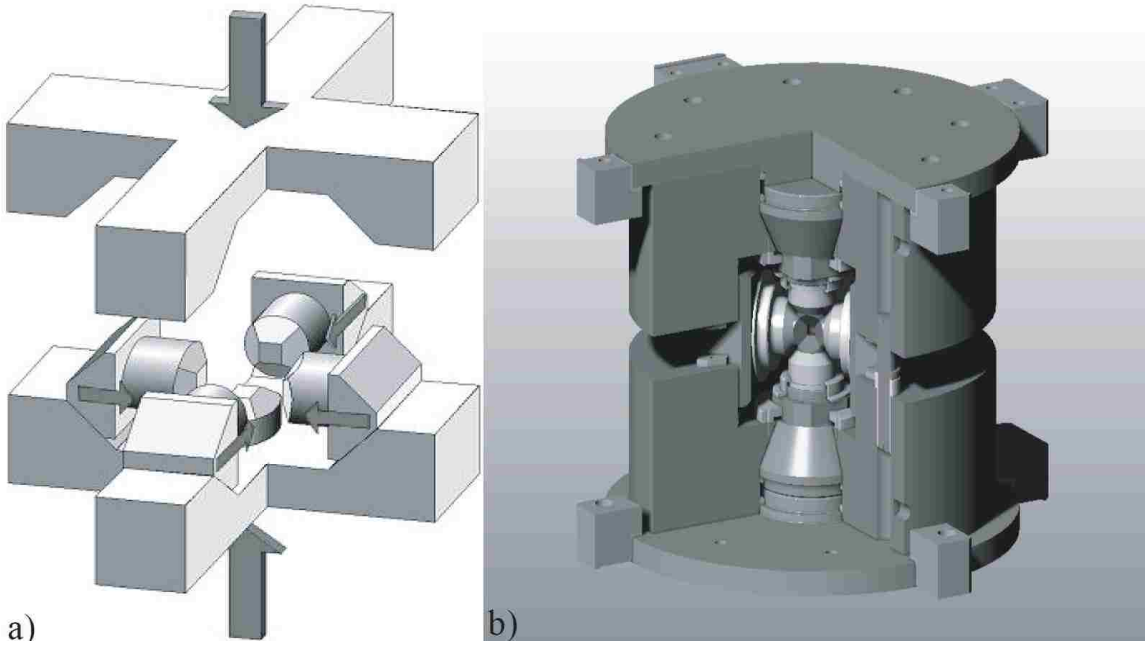

Figure 1.7. DIA and D-DIA. a) DIA; b) D-DIA. When a load is applied to both devices, the anvils are driven together-the D-DIA has embedded rams that can drive the anvils parallel to the applied stress together at a different rate than the others, allowing for a differential stress to be generated. Diagram adapted from Durham et al., 2002.

X-ray piezometry is a new technique using the D-DIA apparatus and other multi-anvil devices. X-ray synchrotron sources have made it possible to measure the lattice plane spacing in polycrystals *in situ* while a sample is being deformed in a multi-anvil apparatus. The gaps in between the anvils allow the x-rays to make it to the polycrystals during deformation experiments, allowing for an *in situ* strain measurement. Equations for the crystal symmetry of olivine have been developed that relate the lattice strain tensor (**ε**), stress tensor (**σ**), and an elastic compliance tensor (**s**) by the following equation: $\boldsymbol{\varepsilon} = {}^{3}\Sigma_{k=1}{}^{3}\Sigma_{l=1}\mathbf{s}_{ijkl}\boldsymbol{\sigma}_{kl}$, which allows for an *in situ* stress estimate to be made (Durham et al., 2002). Diffraction peaks are recorded for specific lattice planes from multiple grains in the polycrystal by an array of detectors that is placed behind the polycrystal relative to the x-ray source to measure the lattice plane strain. The macroscopic strain for the polycrystal is measured by photographing a YAG screen that shows x-rays transmitted through the sample assembly. The orientation of the lattice planes has to be taken into account to relate stress to strain and is given by an angle relative to the compression axis (ψ) to estimate the strain (Figure 1.8). Stress estimates using this technique assume a Reuss state of stress in the polycrystal (Singh et al., 1998).

Researchers have developed new methods to estimate the macroscopic stress supported by polycrystals during diffraction experiments because stress estimates from Singh's technique indicate that lattice planes have different amounts of stress based on their orientation. Recently, self consistent computer simulations of deforming polycrystals have been used to estimate the macroscopic stress for specified macroscopic strains. One of the main advantages of self consistent models is that they do not assume a constant strain or stress for the grains in a polycrystal for macroscopic stress

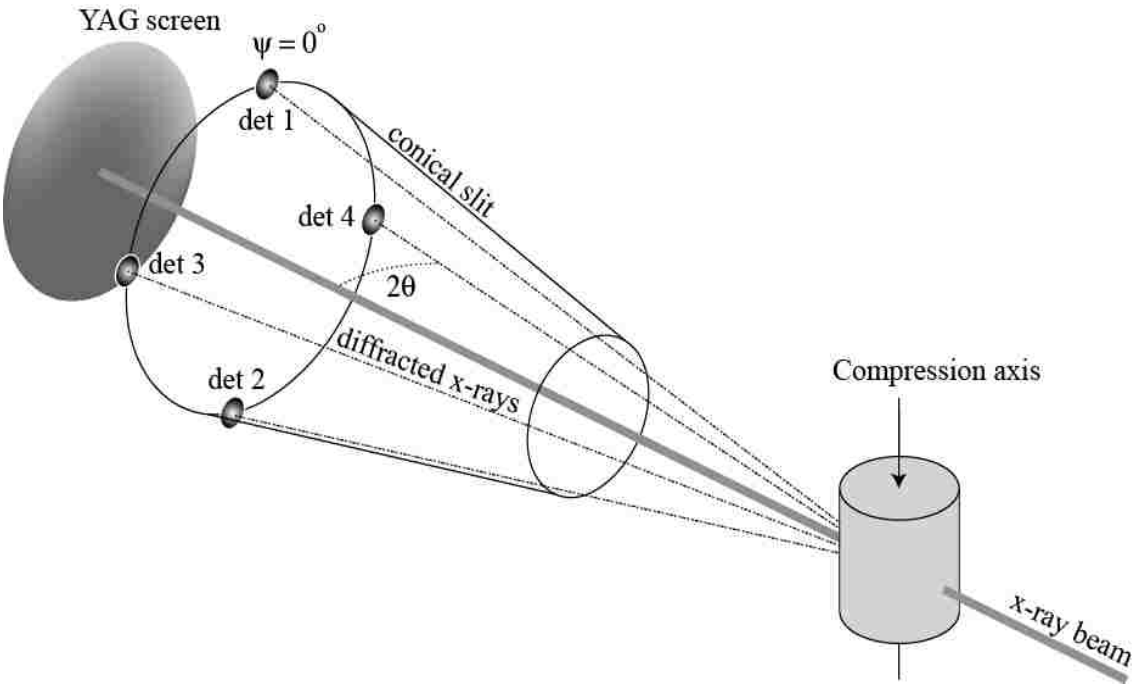

Figure 1.8. General experimental set up for *in situ* lattice plane strain measurements used to estimate the macroscopic stress applied to a polycrystal-x rays pass through the polycrystal and reflect off lattice planes of multiple orientations into detectors. Diagram from Burnley and Zhang, 2008.

predictions. Several different types of models have been used to simulate the deformation of polycrystals including Visco Elastic Plastic Self Consistent models (VPSC) and Elastic Plastic Self Consistent (EPSC) models. In the self consistent models, the grains in a polycrystal are represented as ellipsoidal inclusions with specified orientations within a homogeneous medium in order to estimate the macroscopic stress state of a deformed polycrystal (Wenk, 2002).

The EPSC model is a numerical model that produces stress and strain output for a deformed polycrystal that can be used to estimate the flow strength of olivine. The output from the EPSC model is compared with strain measurements for lattice planes of an olivine polycrystal taken during a diffraction deformation experiment. The flow strength that is determined using the EPSC model for different pressure-temperature conditions

could ultimately be used to create a new flow law for dislocation creep in olivine for conditions in the upper mantle. Despite the success of the EPSC models in fitting lattice strain measured for metals and quartz, there are differences in fitting data from fayalite (Burnley et al., 2008). The strain measurements of the lattice planes of fayalite measured at a confining pressure of 2.5 GPa and a temperature of 700º C have been compared to lattice strain estimates from the EPSC model (Figure 1.9). The strain measurements of different lattice planes from multiple grains show that each lattice plane has a different amount of strain within the polycrystal when a load is applied (Figure 1.9). "Compress" values in figure 1.9 represent the average values for specific lattice planes oriented normal to the compression direction. "Noncompress" values represent average values for specific lattice planes with strain measured in the transverse direction. It is apparent in figure 1.9 that there is a shift from an elastic response to a plastic response to stress at a sample strain of approximately 0.02 for all of the lattice planes except (112) Noncompress. While the EPSC model estimates the strain well when olivine is in the elastic realm, the model values diverge from the experimental values recorded when the olivine started to deform plastically. The same behavior has been observed in previous simulations at lower temperatures and pressures including (25º C, 1 atm).

Estimates of the yield point for olivine may be improved by adding kinking to the EPSC model. Kinking is an accommodation mechanism for hard oriented grains in metal alloys (Wollmershauser et al., 2010). One of the main advantages of the EPSC model is the multitude of input parameters that can be adjusted specifically for the crystal structure of olivine, including active slip systems and a twinning subroutine. The twinning subroutine in the EPSC model provides an approximation for kinking in deformed grains. In order to activate the twinning subroutine in the EPSC model, a shear strain derived

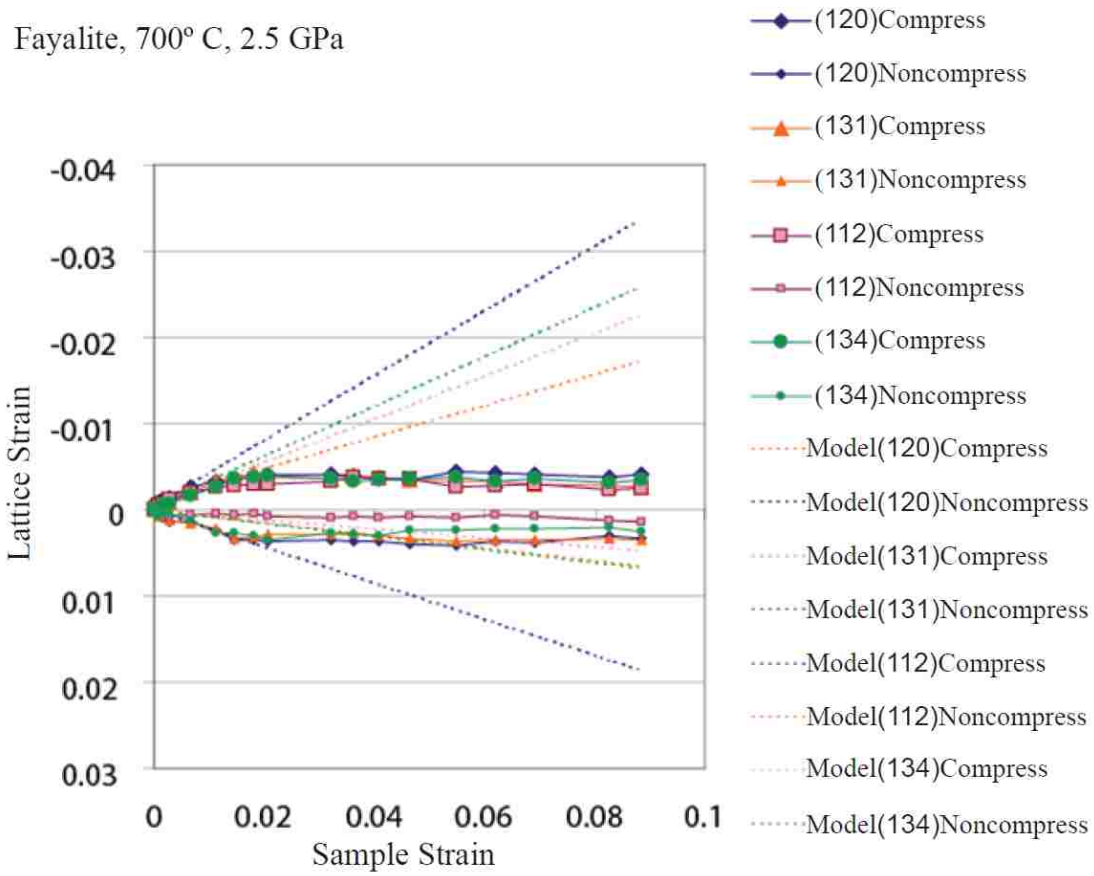

Figure 1.9. Comparison between lattice plane strain in a deformed polycrystal for different lattice planes and EPSC lattice plane strain predictions for a specified macroscopic strain. Diagram adapted from Burnley et al., 2008.

from the kink angle and the slip system are required. Further research is necessary to constrain the geometry of kinking before it can be added to the EPSC model.

CHAPTER 2

METHODOLOGY

A microstructural study of fifteen kinked Mg_2GeO_4 olivine grains was conducted in order to further the geometric understanding of kinking in deformed polycrystals using Electron Back Scatter Diffraction (EBSD) data and optical data. Channel Five software was used to analyze the EBSD data. No kink angle measurements have been recorded from existing studies of deformed Mg_2GeO_4 olivine samples. Orientation maps of fifteen kinked grains from thin sections were made. Pole figures that were made using data from the orientation maps for selected lattice planes were used to determine the direction of the kink axis and kink angle in the kinked grains. The orientation of the axial planes was determined by finding the common plane that contains both the rotation axis and trace of the kink band boundary for each kinked grain in a stereonet; as both of these lines lie within the axial plane. A misorientation angle distribution was also obtained for the entire grain for all of the kinked grains and compared to non-kinked grains. For ten of the kinked grains, the misorientation angle was measured and plotted on a histogram for transects normal to the kink band boundaries to quantify the variability of the kink angle. Transects were also drawn parallel to the kink band domains for ten grains to assess the variability of the misorientation angle within the kink bands.

Data Acquisition

A JEOL JSM-5610 scanning electron microscope (SEM) with an Oxford Nordlys II EBSD detector was used to make the orientation maps in this study. Nine orientation maps were made from three thin sections of deformed Mg_2GeO_4 olivine polycrystals

designated as GL330, GL256, and GL312. Most of the kinked grains were mapped from GL330 because there were more kinked grains in GL330 and indexing rates were better. The thin sections that were used in the study were made from Mg_2GeO_4 olivine polycrystals that were deformed in a Griggs apparatus at temperature and pressure conditions shown in table 2.1. Spinel, Mg_2GeO_4 olivine, and pyroxene are also found in the polycrystals. The samples were prepared for EBSD analysis using a vibromat polisher with a colloidal solution with a particle size of 0.05 μm. After polishing, the areas of the thin sections with the kinked grains were marked using a sharpie. Prior to mapping, the samples were carbon coated to reduce charging on the sample surface during mapping.

Table 2.1. Experimental conditions orientation map samples were deformed in

Sample	Upper (Cº)	Lower T (Cº)	Strain Rate (/s)	Macroscopic Strain (%)	Differential Stress (MPa)
GL330	...	774	$2*10^{-5}$	...	1904±197
GL265	719	715	$2*10^{-4}$	24	2481±118
GL312	925	908	$2*10^{-4}$	15	1279±157

Source: Data from Burnley, 1990.

EBSD orientation maps are made by creating diffraction patterns called Kikuchi patterns and indexing them to obtain orientation data. An SEM beam is rastered across a tilted sample surface and Kikuchi patterns are created, which are recorded by a CCD camera. The CCD camera records photos of the Kikuchi patterns whose orientations are determined for predefined phases by the acquisition software in a process known as indexing. In order to obtain reliable patterns, the system is first calibrated using an oriented Si single crystal, which is mounted next to the sample. In order to determine if

the system was calibrated, the MAD (Mean Angular Deviation) was obtained using the Flamenco software for a point over a silicon standard. The MAD is a measure of the difference between the theoretical pattern that the standard should give and the actual pattern that is measured. Once a satisfactory MAD was measured of ~0.01, the beam was placed over the samples and the maps were made from a selected area at a given magnification. A uniform step size of 2 μm were used for each analysis. Figure 2.1 shows the general setup for EBSD mapping. For this study, the orientation maps were made with a sample tilt of 70º at a working distance of 20 mm between the sample and the pole piece. Orientation maps were made at magnifications from 140x to 340x at operating voltages of 15 kv and 20 kv. When orientation maps were made, an area within the SEM field of view was selected and mapped. The orientation maps are always smaller than the field of view in the SEM because the focus deteriorates at the edges of the field of view. Patterns from Mg_2GeO_4 olivine were indexed using the Pnma space group with a unit cell of a = 10.30, b = 6.03, and c = 4.91. Olivine is traditionally set in the Pbnm space group, which is a = 4.91, b=10.30, and c= 6.03. Therefore, all raw diagrams from the Channel Five software for specific lattice planes were changed back to the Pbnm setting after data analysis. For example, (100) pole figures from the software are actually for (010).

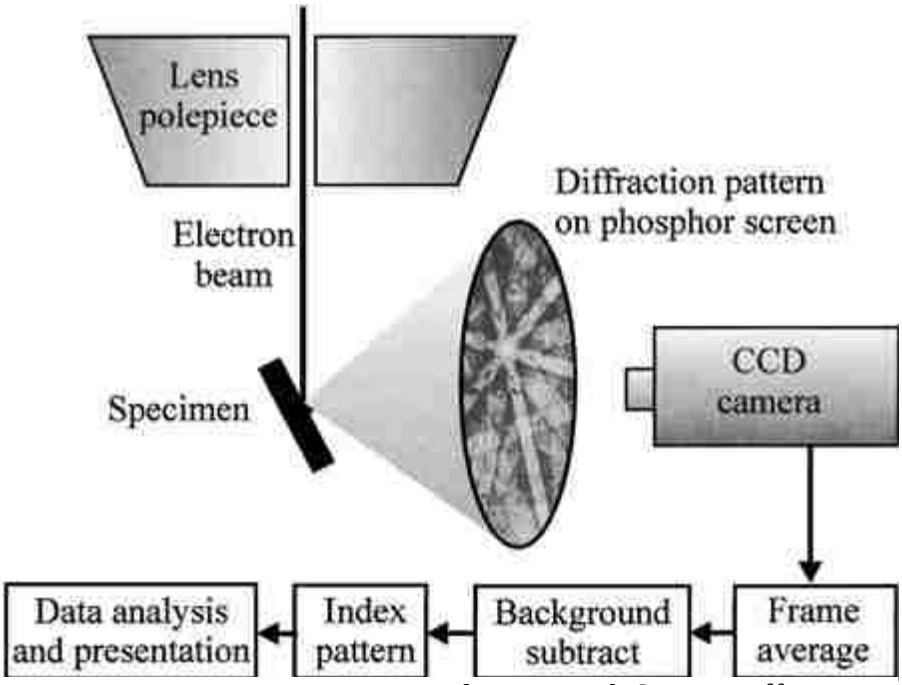

Figure 2.1. Data acquisition using Electron Back Scatter Diffraction. Diagram by Humphreys, 2001.

Data Analysis

After the maps were acquired, Euler angles based on the Bunge convention were used to define the orientations of data points. The Bunge convention uses three rotations to specify orientation with the first rotation about the z axis, the second rotation about the x axis and the third rotation about the y axis. Two coordinate systems in Channel Five software are used to define the orientation of a data point with Euler angles including the sample coordinate axis and the crystal coordinate axis. The sample coordinate axis is coincident with the specimen sample surface with the z axis coming out of the surface towards the observer. The crystal coordinate system is coincident with the major crystal directions in the unit cell of the indexed material. Each orientation range has a color associated with it as shown in figure 2.2. In figure 2.2, ϕ_1, ϕ_2, and ϕ_3 are the rotation angle relative to the x, y, and z directions according to the Bunge convention.

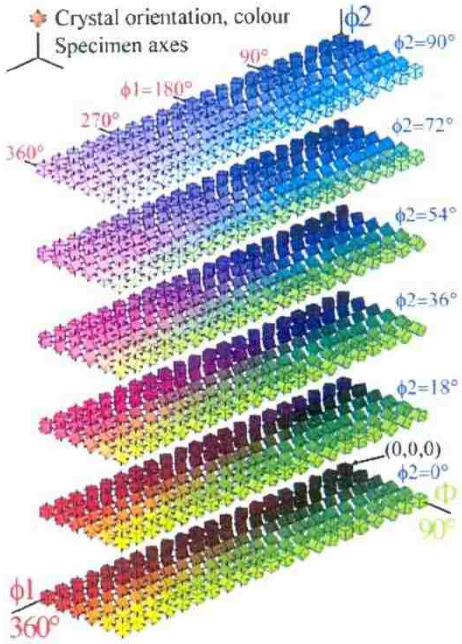

Figure 2.2. Euler colors for orientation of crystallographic coordinate system relative to the sample coordinate system using the Bunge convention. Diagram by Oxford Instruments, 2007.

For the microstructural analysis, the raw data was refined using a Channel Five program called Tango. First the wild spikes were removed, with wild spikes defined as data points misoriented by more than 10º from the average orientation of adjacent data points (Warren et al., 2008). Then the standard setting was used to extrapolate between indexed data points. With the standard setting, an unindexed data point is filled in by the most common orientation of its surrounding neighbors. A setting of four neighbors was used for the standard noise reduction extrapolations. Once the maps were extrapolated, the grain boundary size was specified. In Tango, the grain boundaries are defined by the misorientation of adjacent data points. If the misorientations of the adjacent data points were within 5º, they were grouped together into a grain. The misorientation angle

between adjacent data points is the smallest angular rotation about a common crystallographic direction (Randle, 1992). In Tango, individual grains can be selected and grouped into subsets so that they can be isolated for analysis from other grains in the map. Subsets were made for the kinked grains.

In order to determine the plane of shear, equal angular upper hemisphere pole figures of the scattered data points were made for twelve lattice planes for all of the kinked grains using a program called Mambo. The twelve lattice planes were: (010), (001), (100), {111}, {110}, {011}, {101}, {201}, {403}, {112}, {120}, and {312}. The pole figures were used to identify and determine the orientation of the rotation axis for the kinked grains. The rotation axis was determined for each kinked grain by observing the pole for which the data points from each domain show no rotation. Density contour pole figures were created to measure the kink angle. An angular measurement tool was used to measure the angle between different domains in areas of the kinked grain that had the highest density of data points. A half width setting of 5º was used for the contoured pole figures.

The axial planes for each of the kinked grains in the sample coordinate system were found by fitting a great circle to the kink axis and a pole in the direction of the trace of the kink band boundaries using a program called StereoWin 1.2. The position of the pole to the plane of shear was initially defined by two angular measurements that were made in Mambo using the angular measurement tool. Each angular measurement of the rotation axis used to determine the axial plane was centered at the boundary where the kink domains of each grain overlapped. The first angular measurement was the angular distance from the Z0 axis down to the point. The second angular measurement was the

angle from either the +X0 or -X0 point on the equal angular projection depending on which quadrant the pole was in. The angular measurements from Mambo were converted into a trend and a plunge and imported into StereoWin 1.2. For the trend conversion, the angle of displacement (γ) away from the ± X0 axis was determined geometrically using the formula $\gamma = \arccos(A/B)$, where $A = \cos(\alpha)$ and $B = \cos(90-\beta)$. For the angular measurements made in Mambo, α was the angle from the X0 axis and β was the angle from the Z0 axis. The plunge value used in StereoWin 1.2 was simply $(90-\beta)$. Figure 2.3 summarizes the angular conversion.

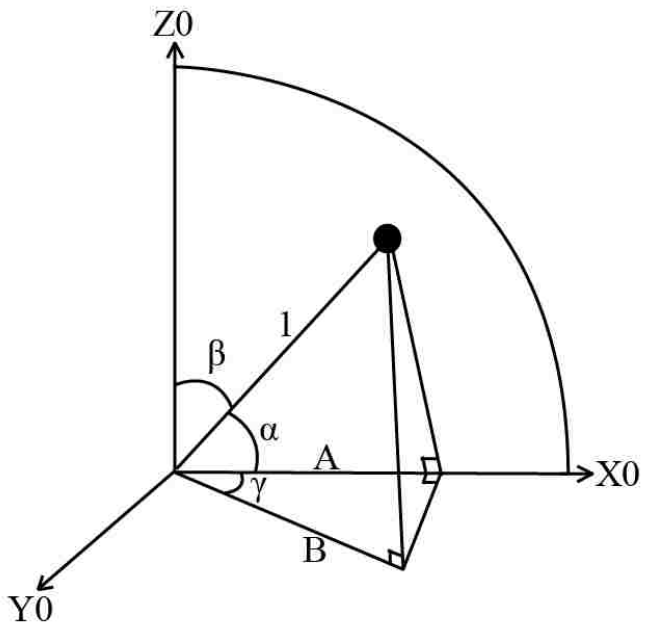

Figure 2.3. Angular conversion from Mambo to StereoWin 1.2 for pole measurements

The trace direction was found by measuring the angle of a kink band boundary from the Y0 axis for each grain on the EBSD maps. Optical measurements of the trace angle were made and compared to the EBSD trace measurements. If the difference in the trace measurements was greater than 4°, the optical trace measurement was used. The trace

measurements were imported into StereoWin 1.2 with the trace angle defined as the trend and a plunge of zero. The Pick Great Circle Command in StereoWin 1.2 was used to generate the axial planes for each kinked grain and determine the orientation of the kinked grains in terms of a strike and dip assuming the right hand rule. The command also generated the trend and plunge of the pole to the axial planes.

The slip direction was determined for the kinked olivine grains by using the orientation of the axial planes. The slip direction for the kinked grains was approximated using the poles to the axial plane, which plot sub parallel to the slip direction for small rotation angles (Vaughn et al., 1978). In StereoWin 1.2, the orientation of the pole to the axial plane was compared to the three principle crystallographic directions from a subset of a kink band domain for each grain. A subset was chosen from a domain to improve the accuracy of the angular measurement from Mambo because (100) and (001) have a wide angular range.

To characterize the kink angle from misorientation angle data in the kinked grains, correlated histograms of each kinked grain were created that included frequency of misorientation angles between pairs of adjacent data points within the kinked grains. The frequency of misorientation is the ratio of misorientation pairs to the total number of misorientation pairs. Separate histograms were made for the kinked grains and non-kinked control grains. Once all of the histograms for each type of grain were made, the histograms were combined to form a cumulative histogram.

Detailed information about the spatial variation of the kink band angle across a kinked grain was obtained for ten of the kinked grains by using the misorientation transect tool in Tango. The misorientation transect tool measures the misorientation angle

between data points along a line. The misorientation angle was recorded between adjacent data points along the transect. The distance traversed by each transect in the X0Y0 plane is included in the misorientation profiles. For these kinked grains, misorientation profiles were made for transects drawn across the grains normal to the kink band boundaries and parallel to kink band boundaries. Several parallel transects were made normal to the kink band boundaries to assess the degree of variability in the kink band angle along the kink band boundary for each kink domain. One transect parallel to the domain was made for each domain in the kinked grains to assess the orientation variability within kink band domains. Misorientation transects were also made across four grains that were not kinked for comparison with the misorientation transects for the kinked grains. A histogram for the misorientation angles from all of the transects was created to assess the kink angle along the kink band boundaries in the kinked grains.

CHAPTER 3

RESULTS

EBSD Orientation Map Results

All of the targeted kinked grains were indexed well enough to show distinct domains with different Euler orientations in the raw orientation data, although there was a wide range of indexing rates for the maps. Some of the maps have large areas that were not indexed. The raw index rates vary from a minimum of 24% in GL330C to a maximum of 63% in map GL265. Map GL330A has the largest amount of extrapolation applied to it to smooth out and fill in the kink band boundaries with an additional 30% of indexed area added to the raw indexed area. Maps GL330G and GL265 had the least amount of extrapolation applied to them with an additional 11% of map area added. The average MAD values for the maps are all less than or equal to .64. Table 3.1 shows a summary of the magnifications, the MAD, index rates and extrapolation for the maps with the kinked grains. The raw orientation maps are compared to the noise refined orientation maps in figure 3.1-figure 3.9. A number of factors contributed to the range in index rates including pits in the sample surface, minor occurrences of the pyroxene and spinel phase, misindexing, and cracks. In grain K4, there were some areas covered by the sharpie used for marking that could not be indexed.

The refined maps match well with optical photographs of the kinked grains. The trace of the kink band boundaries is distinguished by the change in extinction angle and cracks along kink band boundaries in the optical photos, while the trace occurs along the change in orientation color in the orientation maps. The kink band domains for each grain are

Table 3.1. EBSD orientation map index and extrapolation results

Map	Grains	Magnification	MAD	Index (%)	Extrapolation (%)
GL330A	K1-K3	300x	.44	.49	.30
GL330B	K4	200x	.48	.25	.23
GL330C	K5	230x	.58	.24	.25
GL330D	K6	300x	.60	.47	.29
GL330E	K7	350x	.55	.51	.20
GL330F	K8	160x	.61	.74	.12
GL330G	K9-K13	140x	.62	.52	.11
GL265	K14	330x	.59	.63	.11
GL312	K15	140x	.64	.40	.16

labeled and correlated between the optical photos and the noise reduced orientation maps in figure 3.10-figure 3.24. Distinct domains are given a letter designation and kink bands of the same domain are labeled by their number. For example, in grain K7, the second kink band of domain orientation A is named domain K7A2 (figure 3.16). The domains in the optical photos were all found in the kinked grains from the orientation maps with the exception of grain K3. Grain K3 could not be completely correlated because not all of grain K3 was in the field of view in the orientation map. Most of the grains have two prominent kink band domains. In addition, the relative widths of the kink band domains for each kink are similar. The difference in the orientation of the trace of the kink band boundary between the optical photos and orientation maps is no greater than 4º for ten of the fifteen grains. Grains K5, K9, and K10 do show a significant deviation between the trace measurements. The difference between the optical and orientation map measurements for these grains is 17º,18º, and 17º respectively. A tilt distortion in the EBSD detector is the most likely cause of the deviation between optical and orientation measurements. Grain K9 and grain K10 have the least developed kink band boundaries of the fifteen grains, which also made it difficult to accurately measure the orientation of the

kink band boundary traces. Overall, the orientation maps provide a solid spatial representation for the orientation of the kinked grains.

Fourteen out of fifteen kinked grains have two distinct domain orientations that alternate across the grains. Many grains that have two prominent domain orientations also show additional Euler sub-orientations. Grains K5, K6, K8, and K9 have two distinct domains but show a third Euler orientation that appears in one or both of the kink band domains. A light blue Euler sub-orientation is found along the edges of grain K5 in domains including K5A1, K5B3, K5A5, and K5B7 (figure 3.14b). The light blue Euler sub-orientation can be correlated with the optical image of grain K5 (figure 3.14). For example in domain K5B3, there is a shift from purple birefringence to white birefringence. In domain K5B7, the light blue corresponds to the orange-white birefringence. In grain K6, Domain A appears throughout the grain, while domain B shows a pink Euler orientation in the upper portion of grain K6 and a blue-green sub-Euler orientation in the lower portion of the grain (figure 3.15b). In the optical photo of grain K6, there is a shift from black birefringence to white birefringence from the upper section of domain B to the lower section of domain B (figure 3.15a). The orientation map of K8 shows an additional blue sub-orientation in domain K8B2 (figure 3.17b) and grain K9 shows an additional green sub-orientation in domain A (figure 3.18b). Although present in the orientation map data, neither of these sub-orientations could be identified in the optical photos. Grain K15 has three distinct domains optically and in the orientation maps (figure 3.24b). In grain K15, domain A is found on the outer edges of the grain primarily on the top and bottom of the grain (figure 3.24). In the orientation map, grain K15A is absent in the center of K15. Grain K15 also has a subgrain that has two domains

with blue and purple Euler orientations (figure 3.24b).

The kinked grains have kink band boundaries that are both curved and straight. Grain K12 has curved kink band boundaries and grain K14 has straight kink band boundaries. Many grains have kink band boundaries with limited curvature. Figure 3.25 shows a comparison of the shape of the kink band boundaries in the optical photographs of K12 and K14. There are also delamination cracks in some of the kink bands, particularly in grains K5 (figure 3.14) and K7 (figure 3.16). The width of the kink band domains varies from grain to grain and can also vary within the same grain as in grain K2 (figure 3.11). Domain K2A3 is wider than the other A domains in grain K2. The orientation of the kink band boundary traces for the kinked grains is predominantly perpendicular to the compression axis (figure 3.10-figure 3.24).

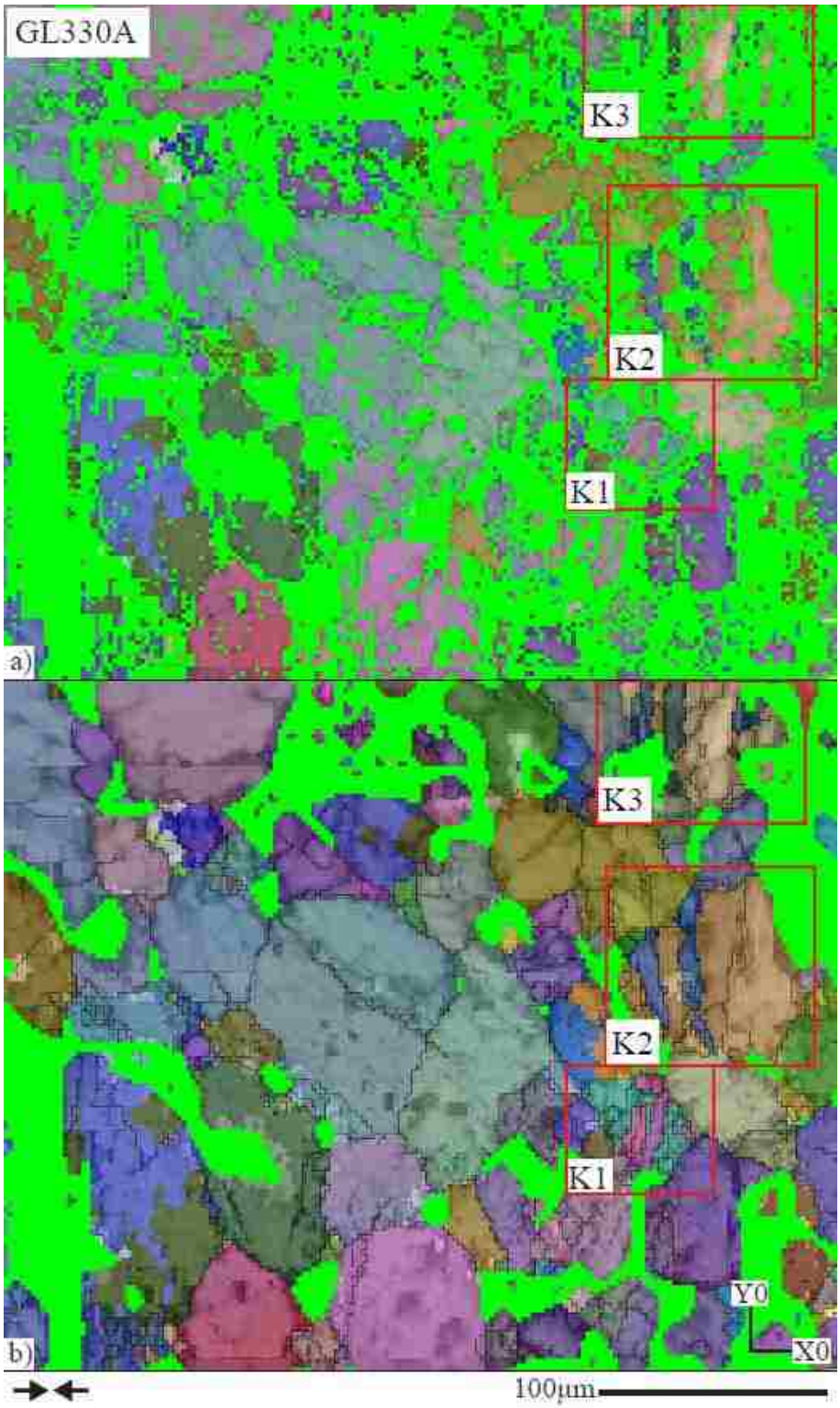

Figure 3.1. GL330A raw and refined orientation map. a) GL330A raw; b) GL330A refined.

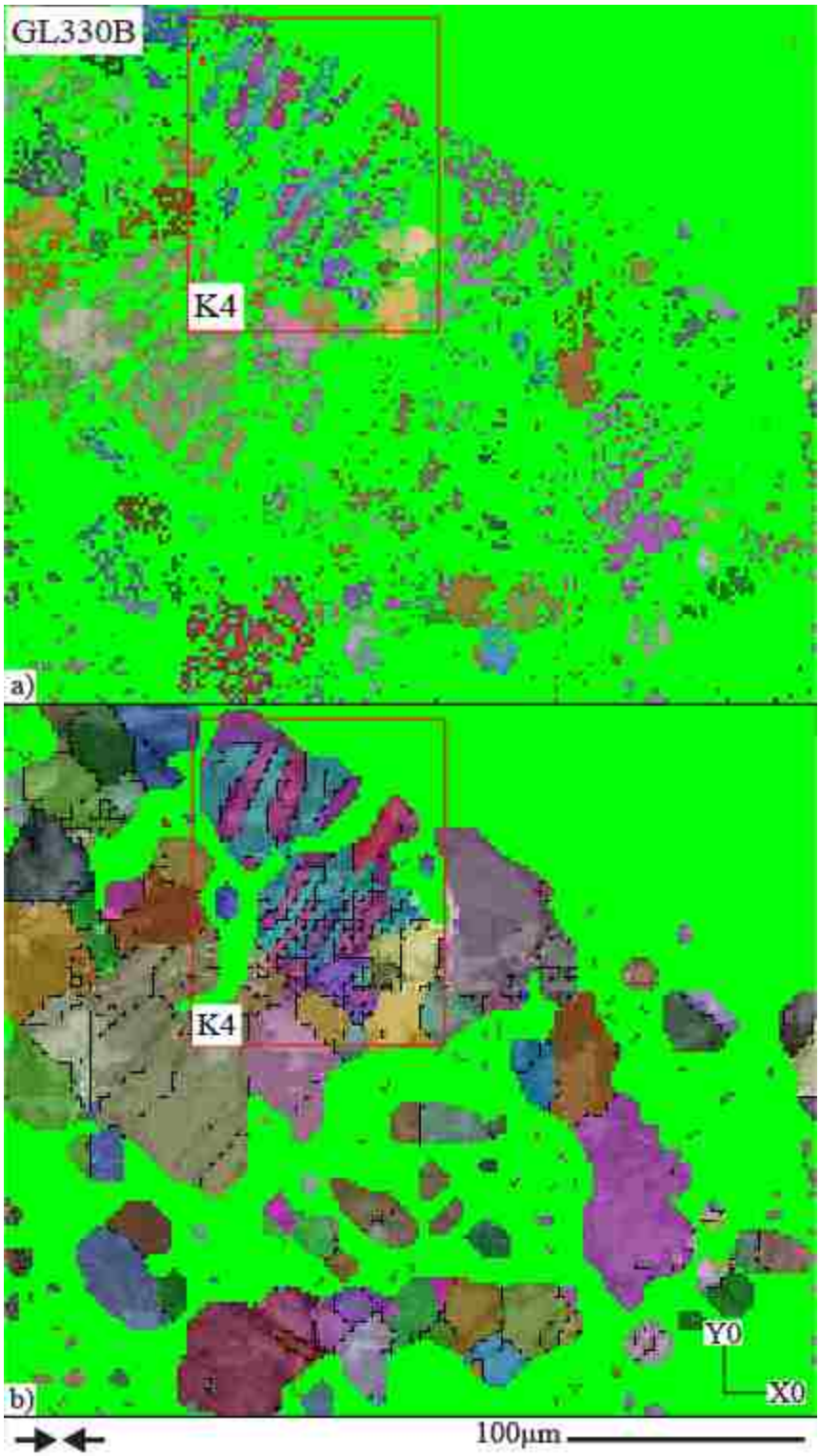

Figure 3.2. GL330B raw and refined orientation map. a) GL330B raw; b) GL330B refined.

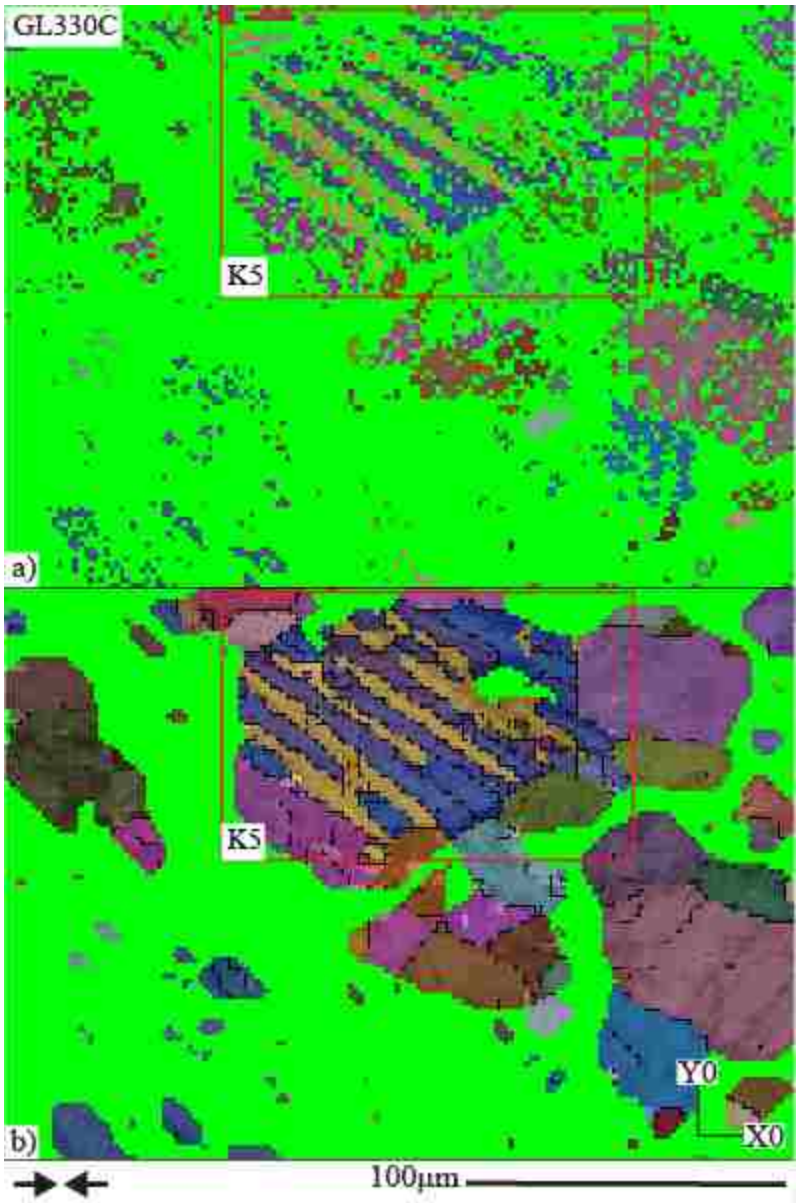

Figure 3.3. GL330C raw and refined orientation map.
a) GL330C raw; b) GL330C refined.

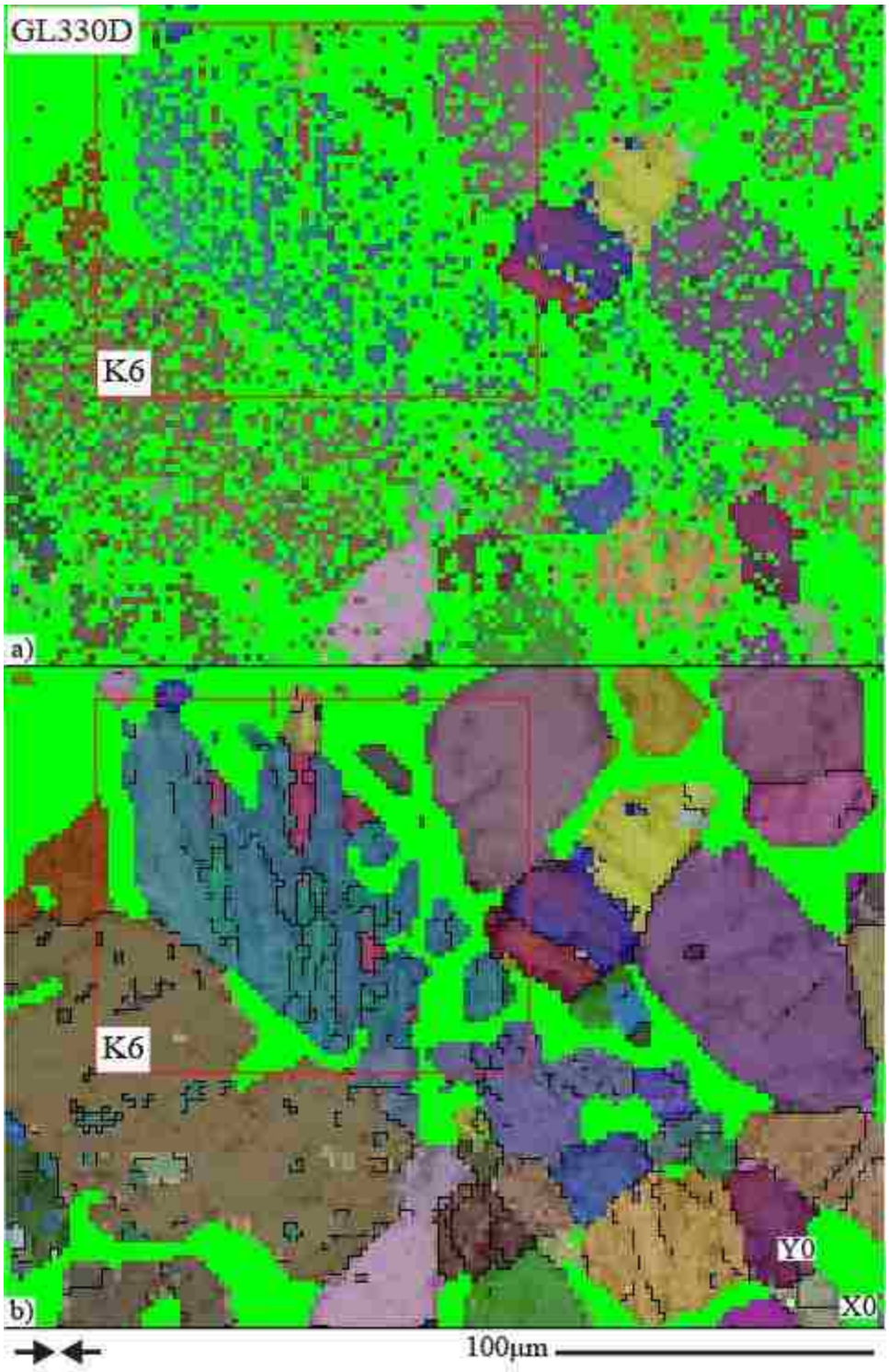

Figure 3.4. GL330D raw and refined orientation map. a) GL330D raw; b) GL330D refined.

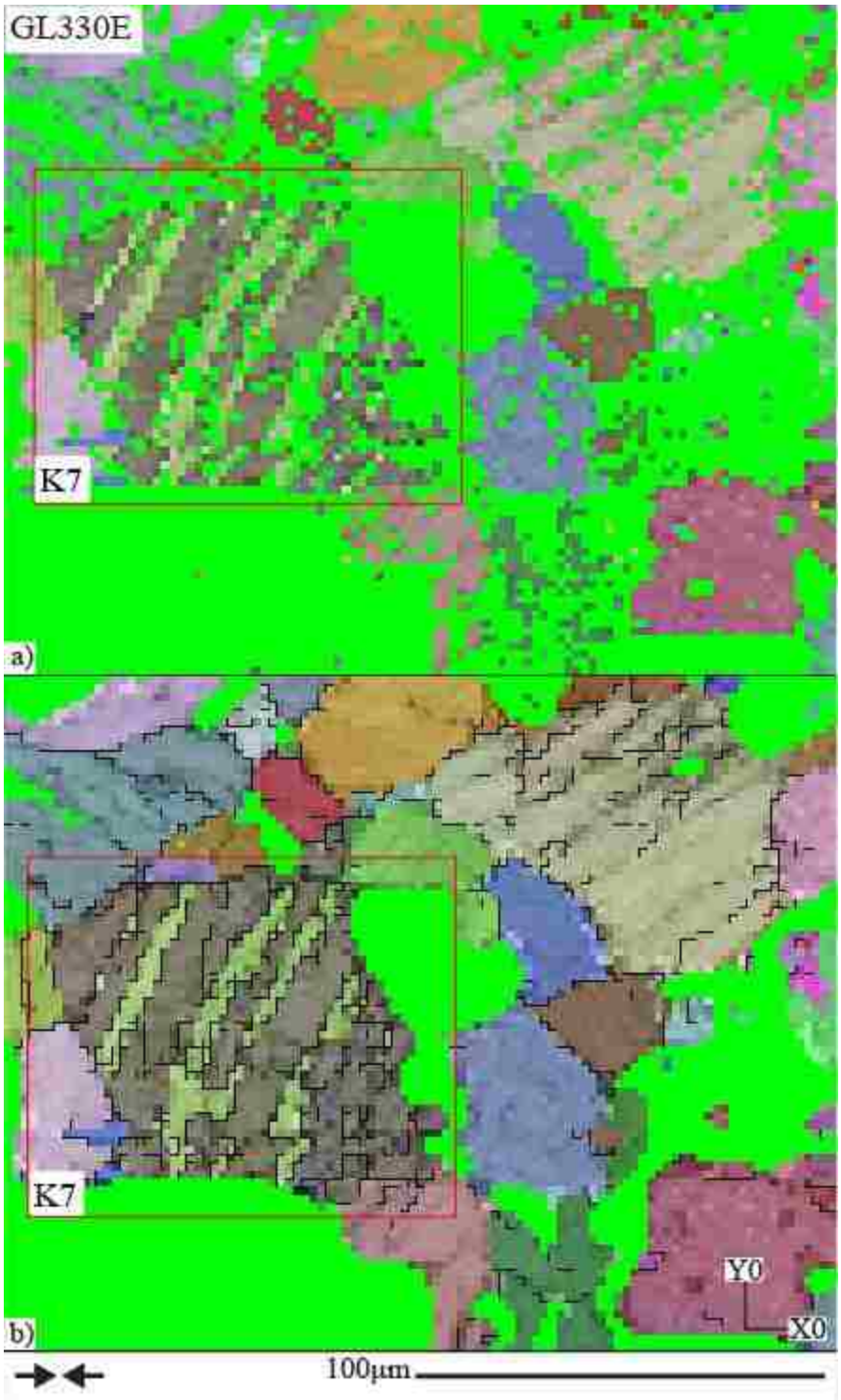

Figure 3.5. GL330E raw and refined orientation map. a) GL330E raw; b) GL330E refined.

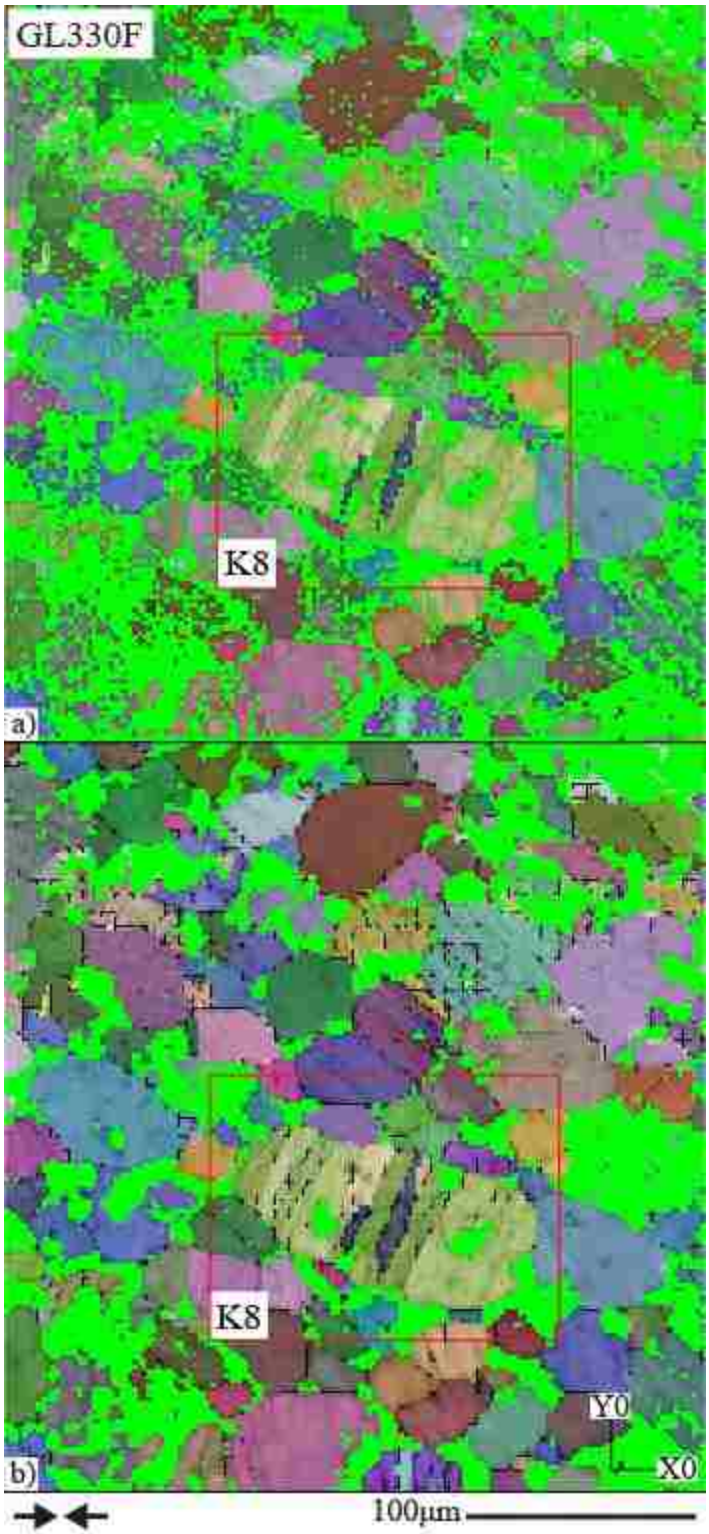

Figure 3.6. GL330F raw and refined orientation map.
a) GL330F raw; b) GL330F refined.

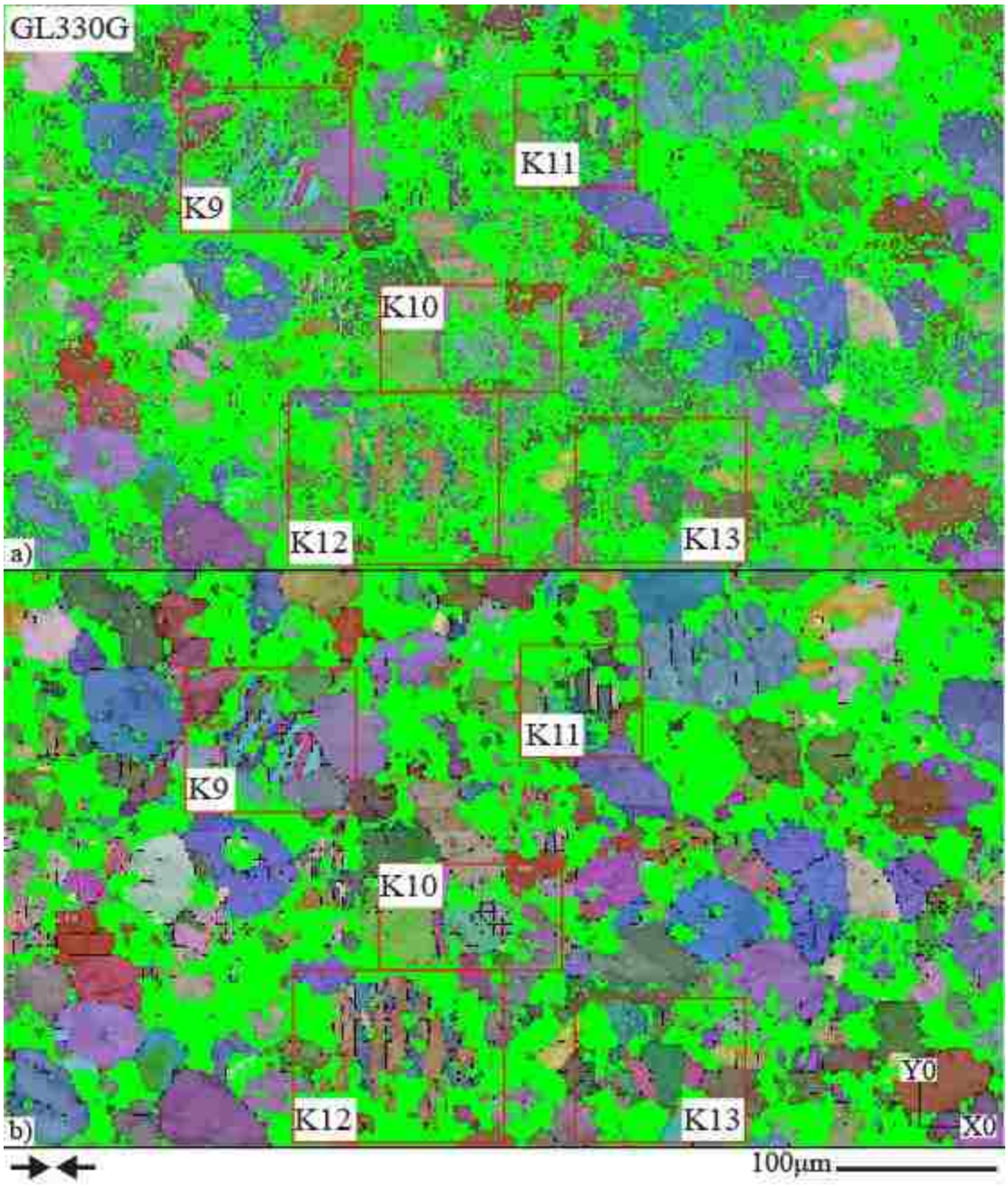

Figure 3.7. GL330G raw and refined orientation map. a) GL330G raw; b) GL330G refined.

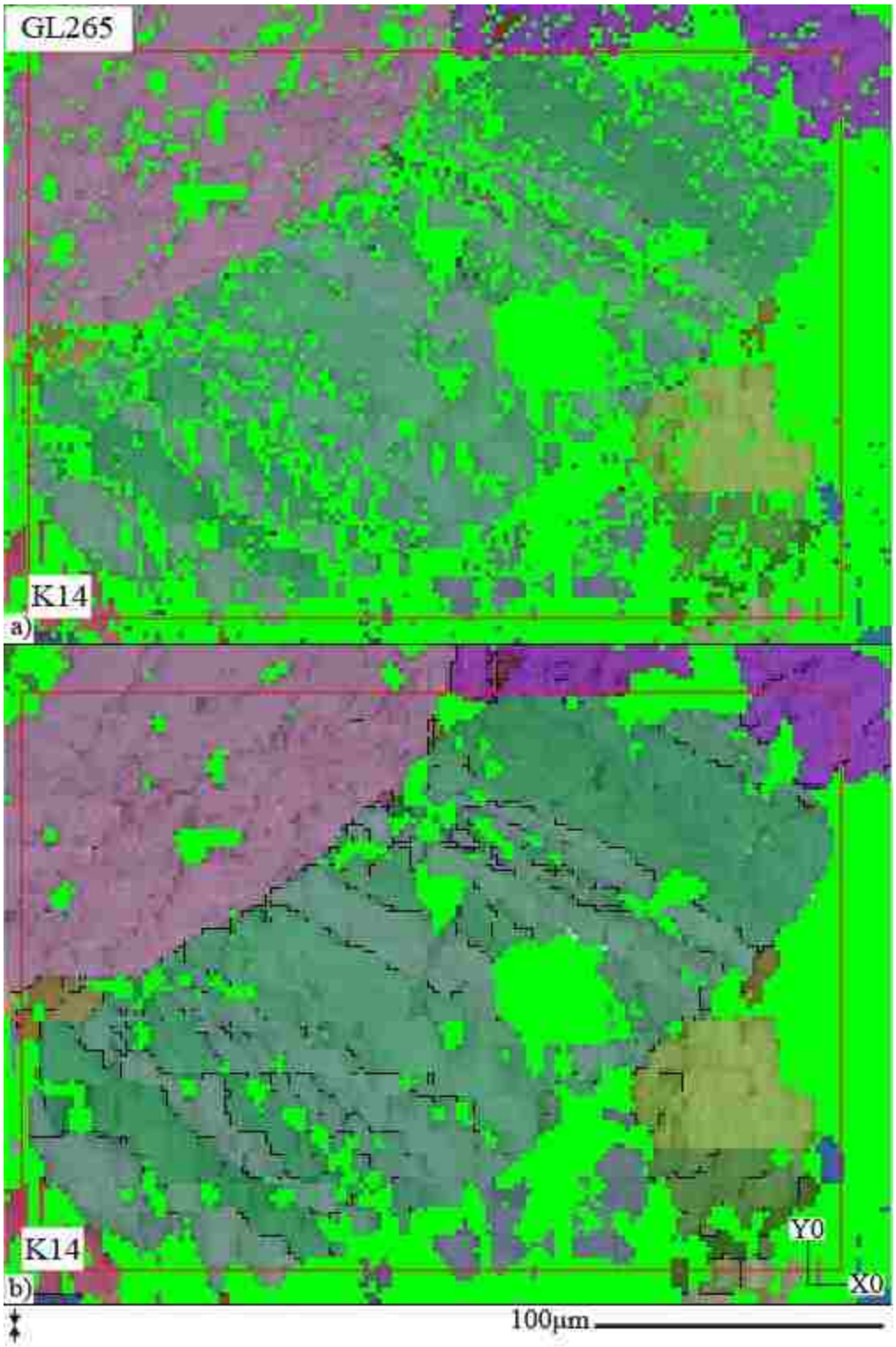

Figure 3.8. GL265 raw and refined orientation map. a) GL265 raw;
b) GL265 refined.

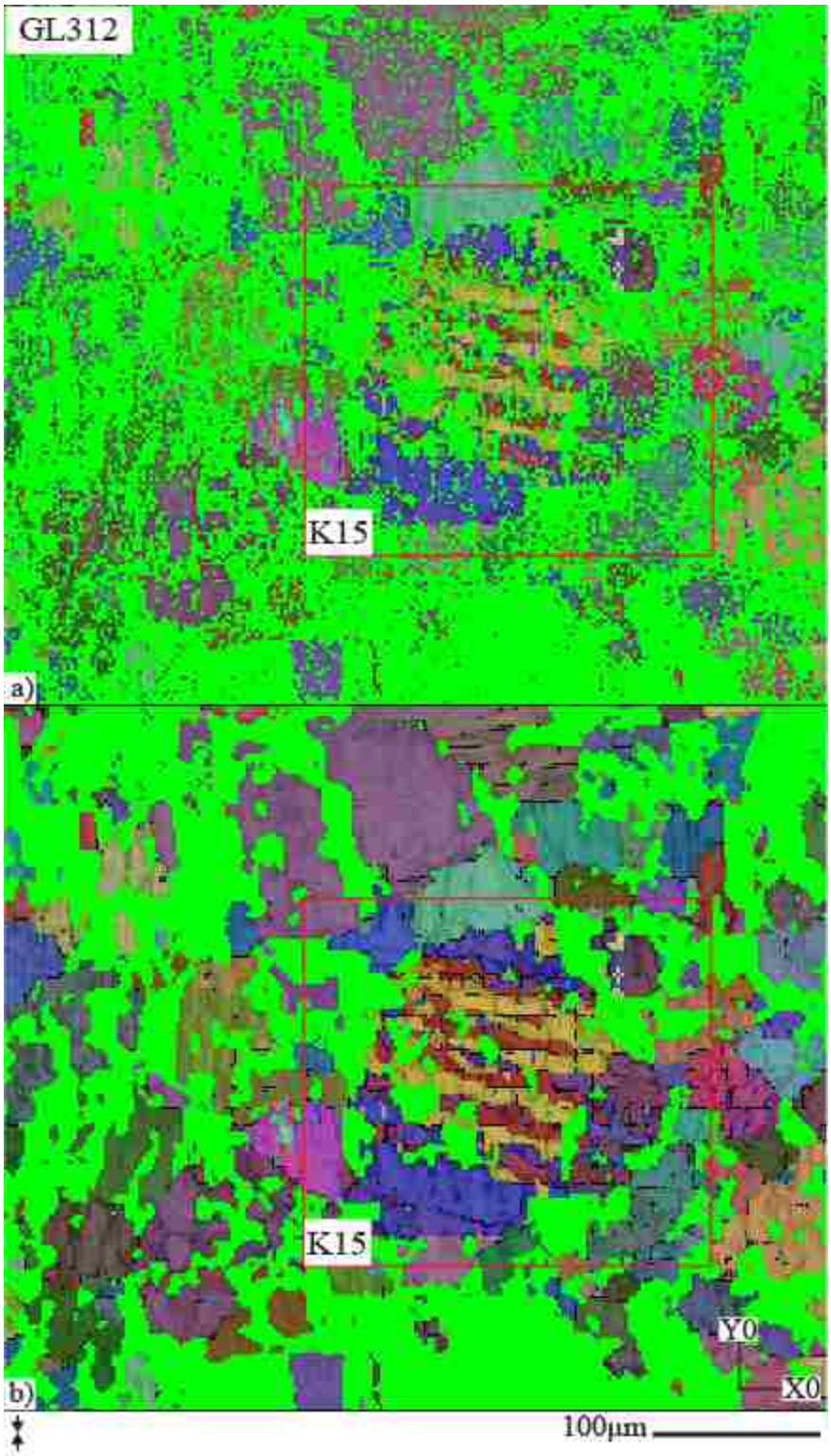

Figure 3.9. GL312 raw and refined orientation map.
a) GL312 raw; b) GL312 refined.

Figure 3.10. Kink band domains for grain K1 in optical and orientation map image. a) optical image of grain K1; b) orientation map image of grain K1.

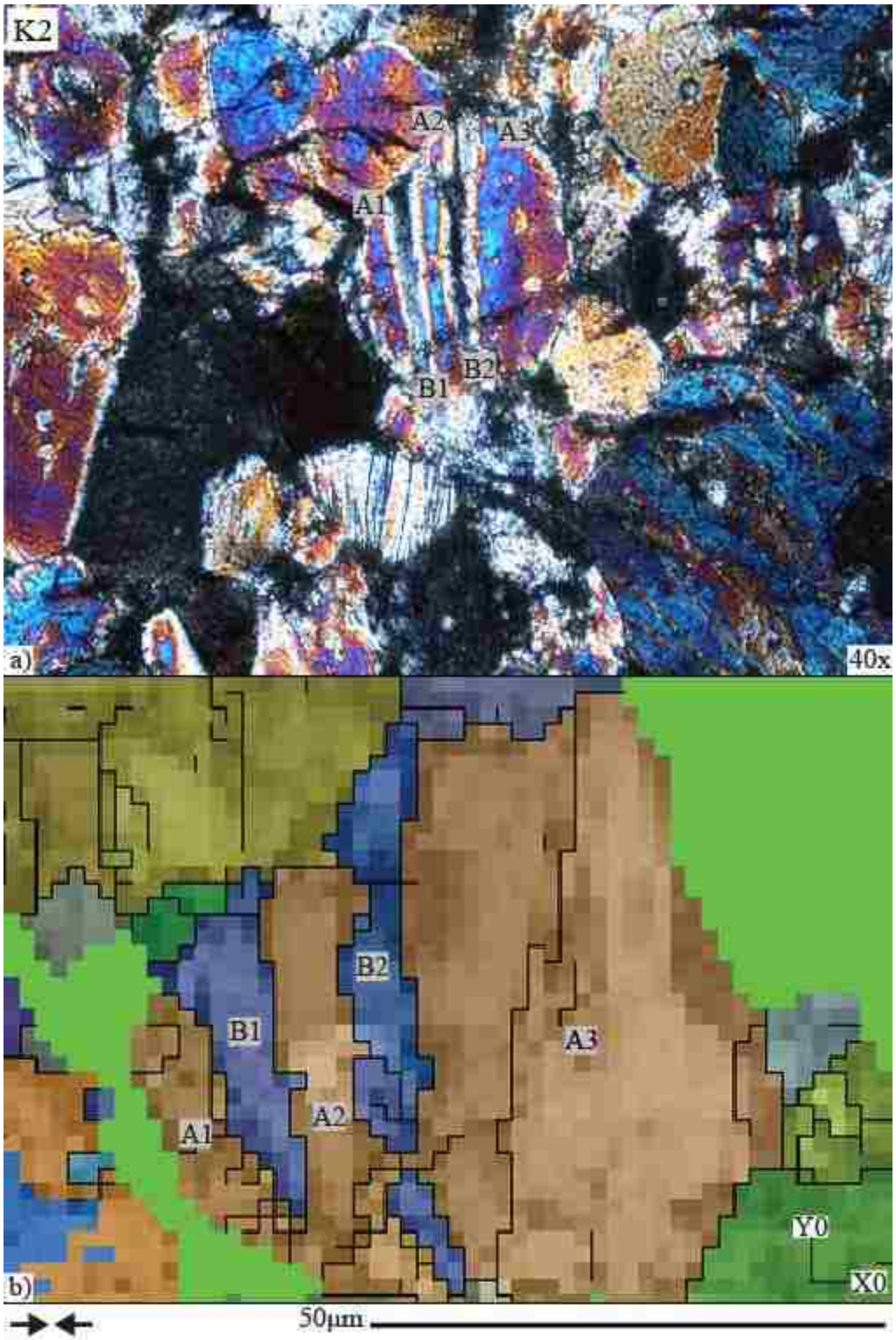

Figure 3.11. Kink band domains for grain K2 in optical and orientation map image. a) optical image of grain K2; b) orientation map image of grain K2.

Figure 3.12. Kink band domains for grain K3 in optical and orientation map image. a) optical image of grain K3; b) orientation map image of grain K3.

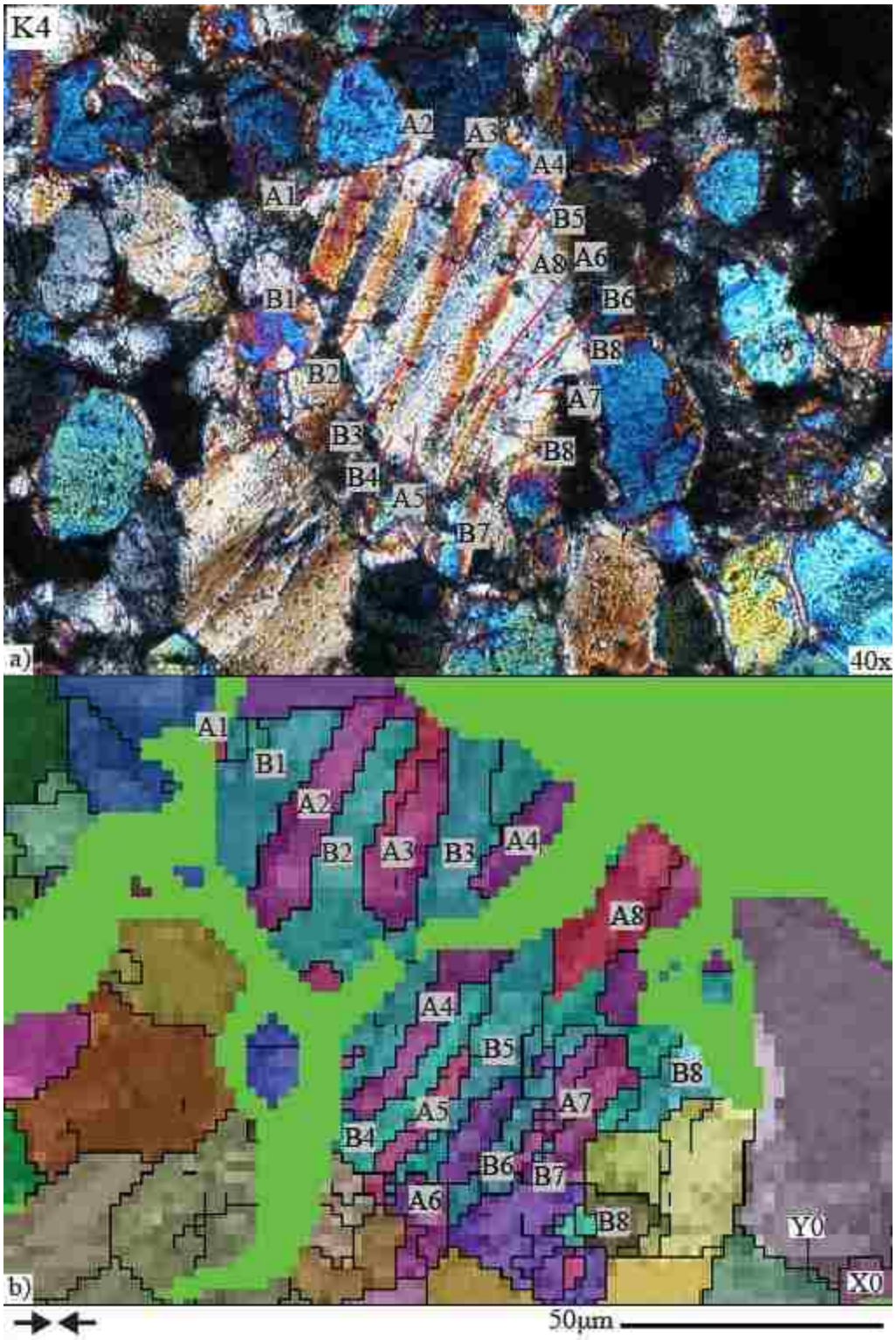

Figure 3.13. Kink band domains for grain K4 in optical and orientation map image. a) optical image of grain K4; b) orientation map image of grain K4.

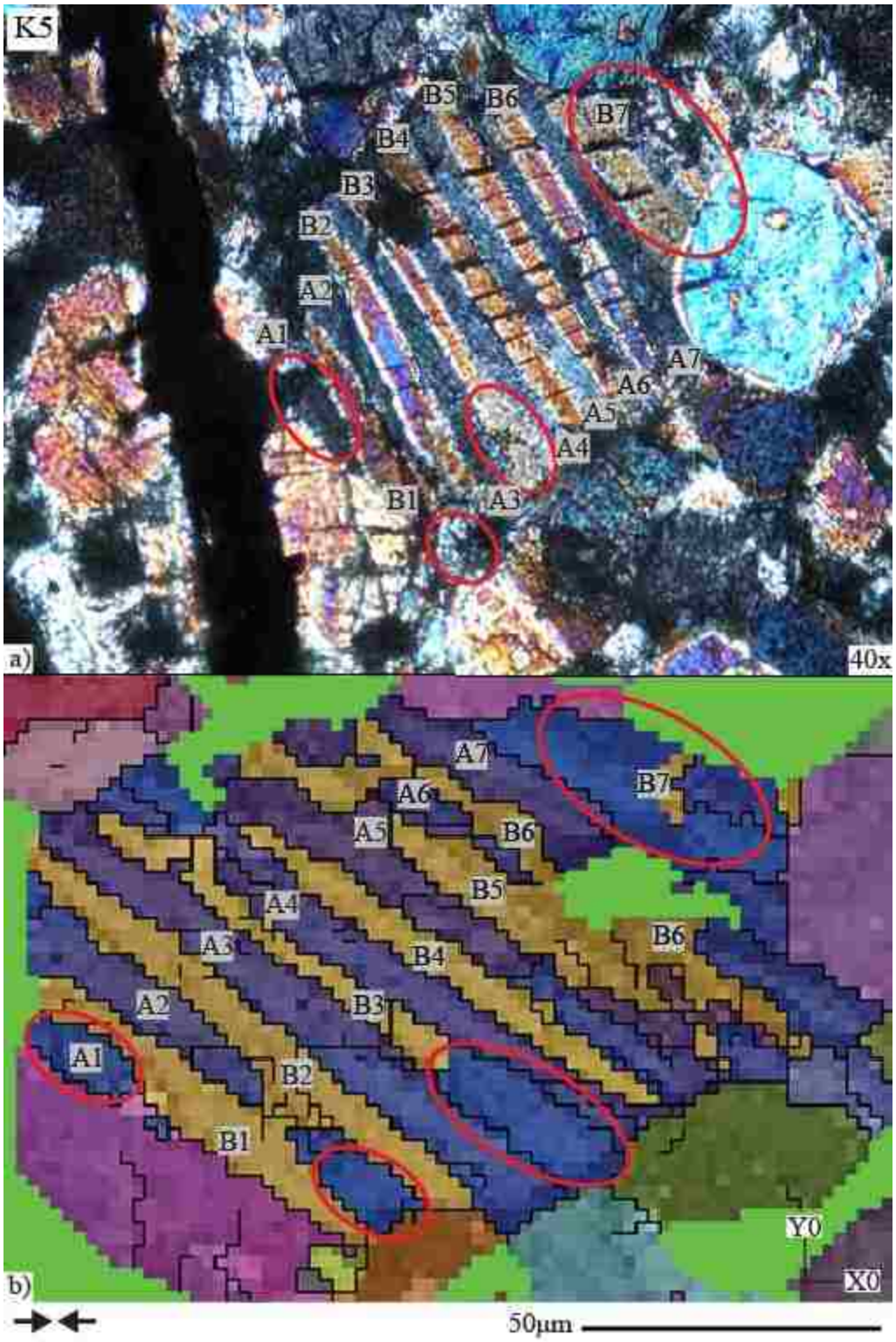

Figure 3.14. Kink band domains for grain K5 in optical and orientation map image. a) optical image of grain K5; b) orientation map image of grain K5.

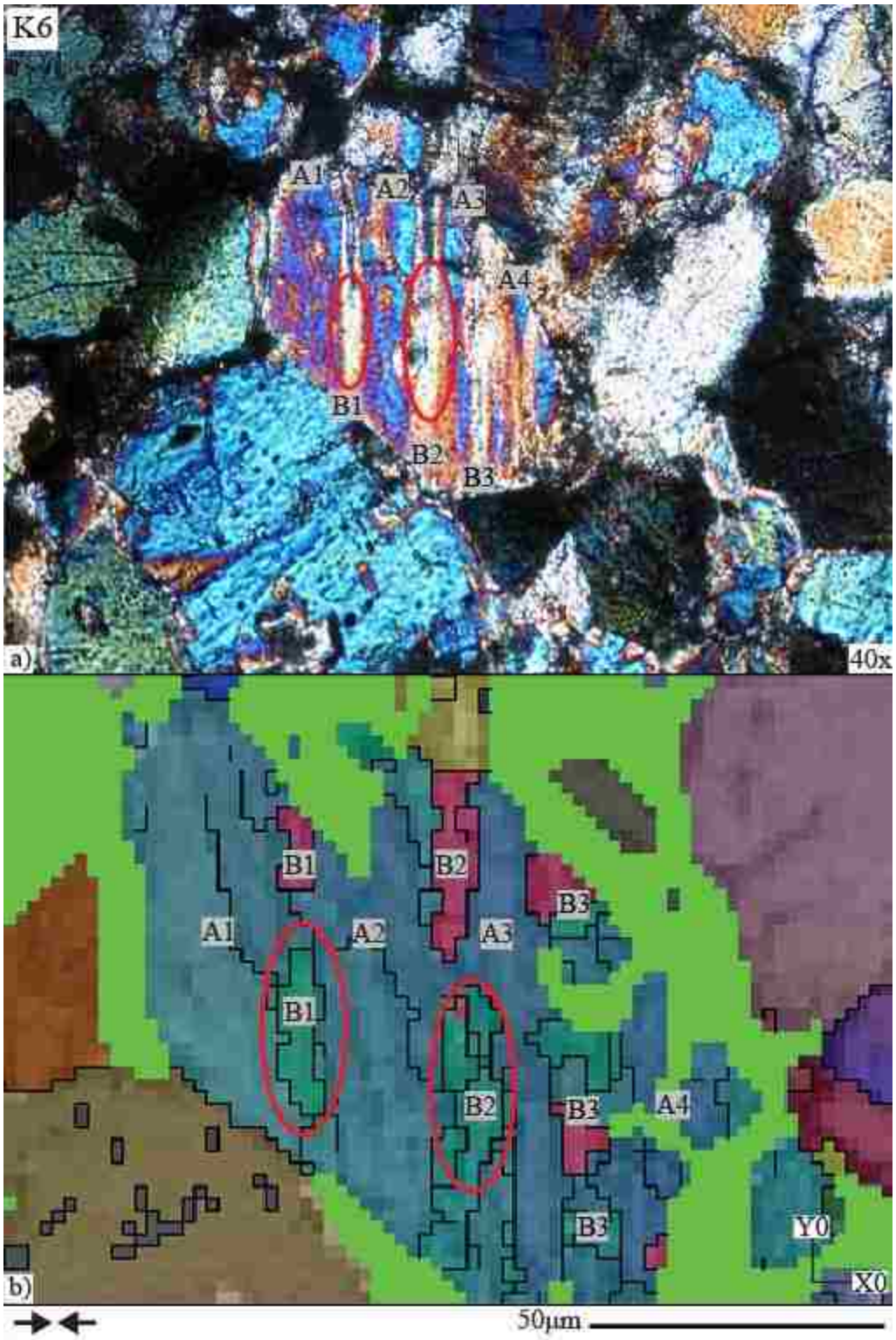

Figure 3.15. Kink band domains for grain K6 in optical and orientation map image. a) optical image of grain K6; b) orientation map image of grain K6.

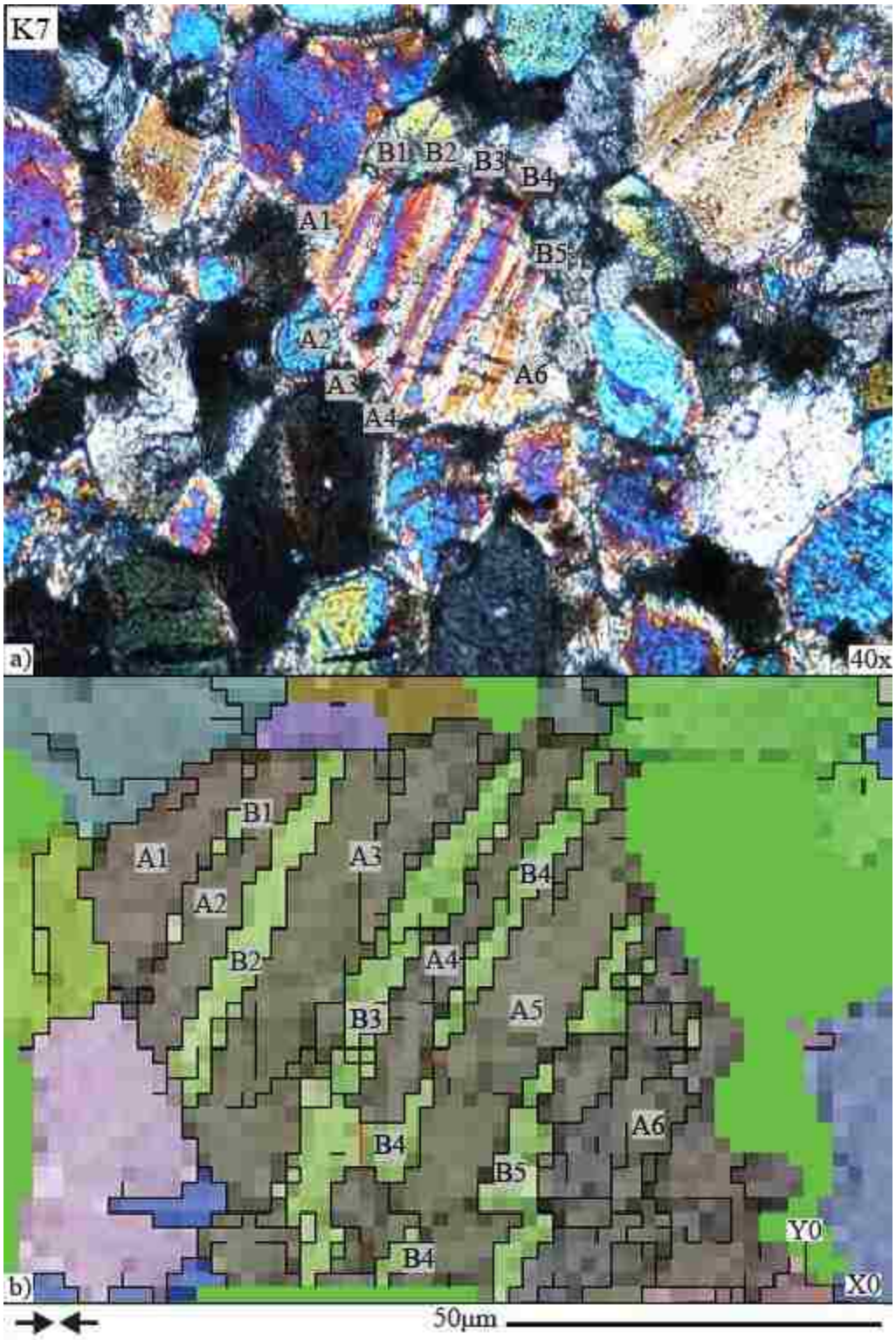

Figure 3.16. Kink band domains for grain K7 in optical and orientation map image. a) optical image of grain K7; b) orientation map image of grain K7.

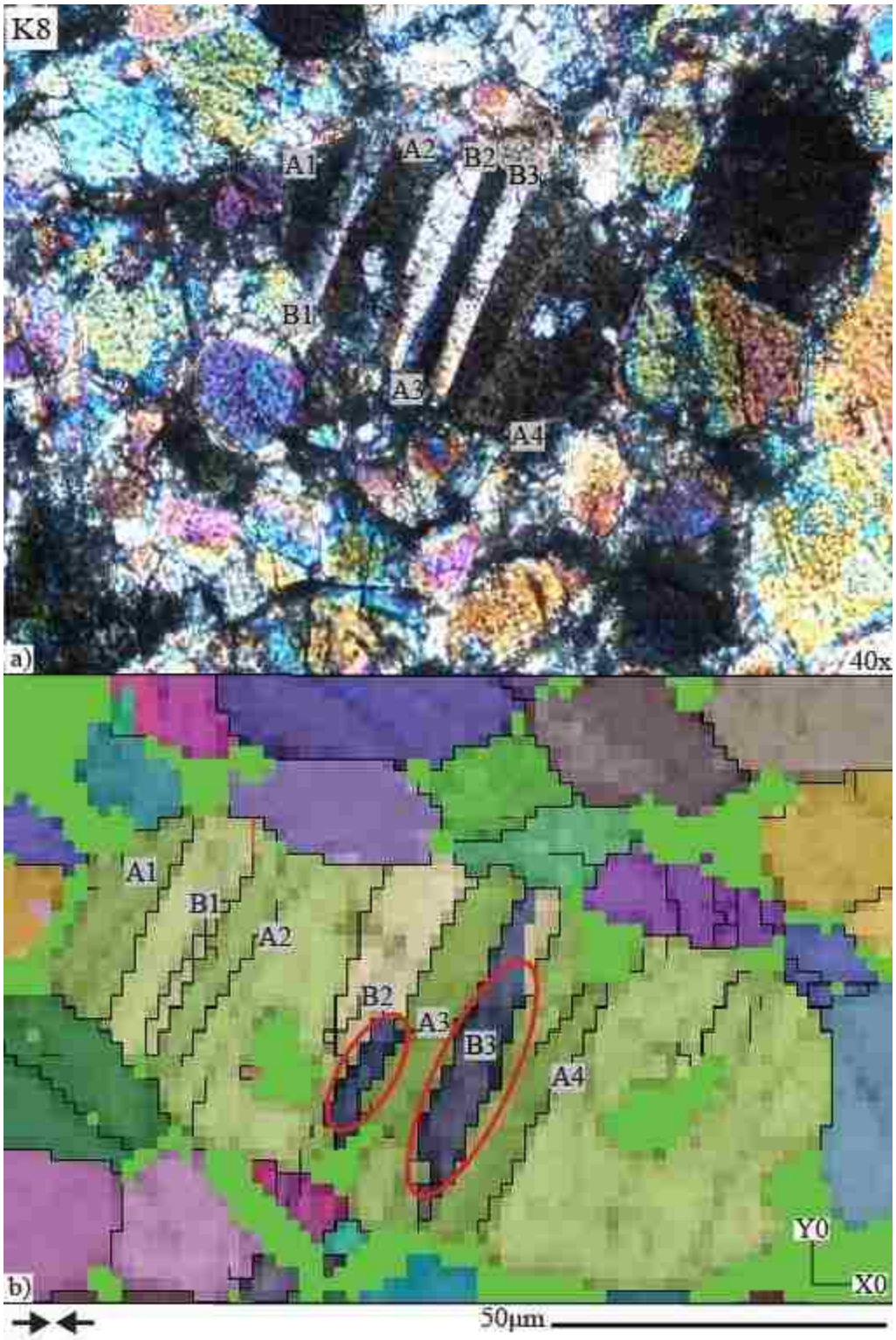

Figure 3.17. Kink band domains for grain K8 in optical and orientation map image. a) optical image of grain K8; b) orientation map image of grain K8.

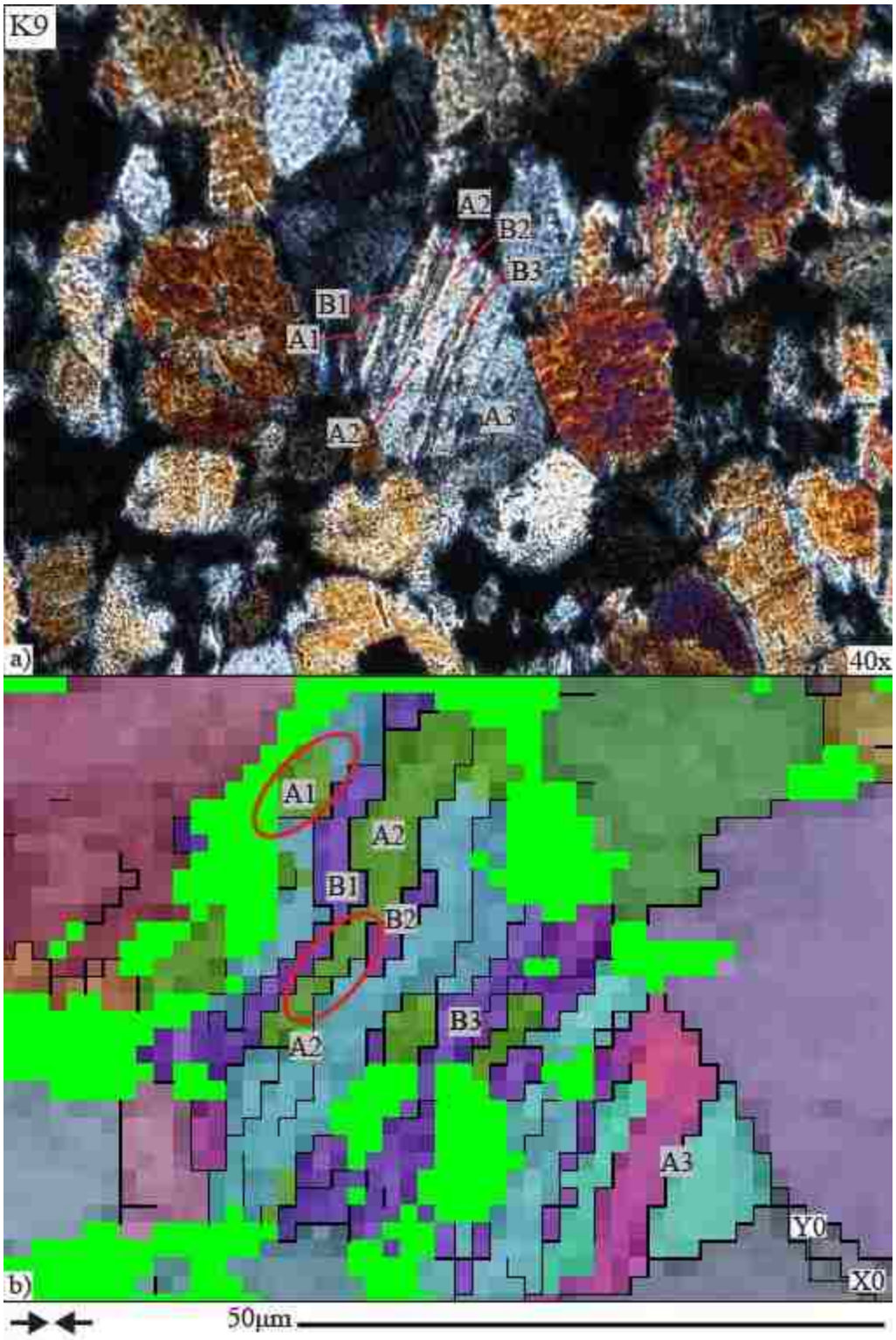

Figure 3.18. Kink band domains for grain K9 in optical and orientation map image. a) optical image of grain K9; b) orientation map image of grain K9.

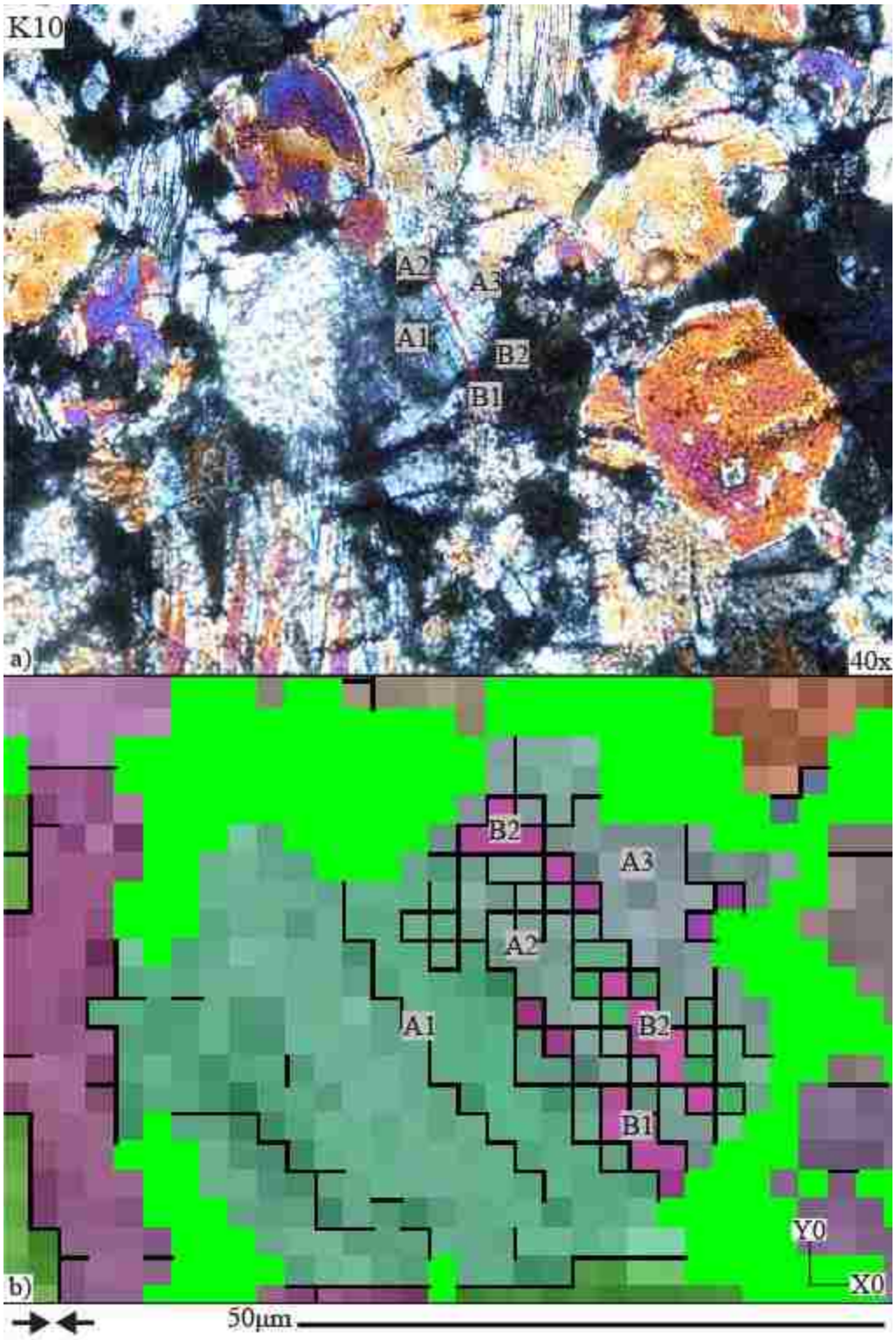

Figure 3.19. Kink band domains for grain K10 in optical and orientation map image. a) optical image of grain K10; b) orientation map image of grain K10.

Figure 3.20. Kink band domains for grain K11 in optical and orientation map image. a) optical image of grain K11; b) orientation map image of grain K11.

Figure 3.21. Kink band domains for grain K12 in optical and orientation map image. a) optical image of grain K12; b) orientation map image of grain K12.

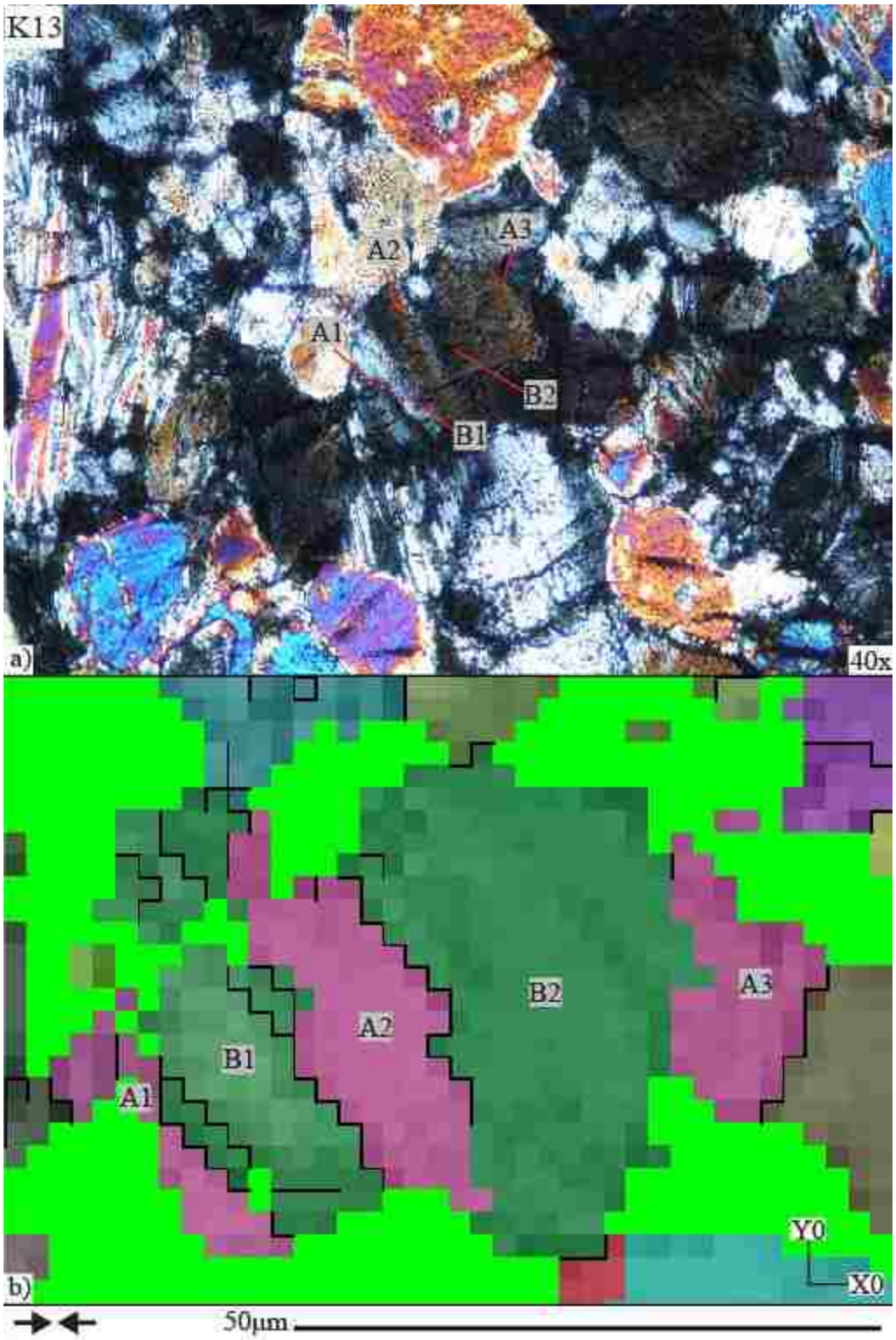

Figure 3.22. Kink band domains for grain K13 in optical and orientation map image. a) optical image of grain K13; b) orientation map image of grain K13.

Figure 3.23. Kink band domains for grain K14 in optical and orientation map image. a) optical image of grain K14; b) orientation map image of grain K14.

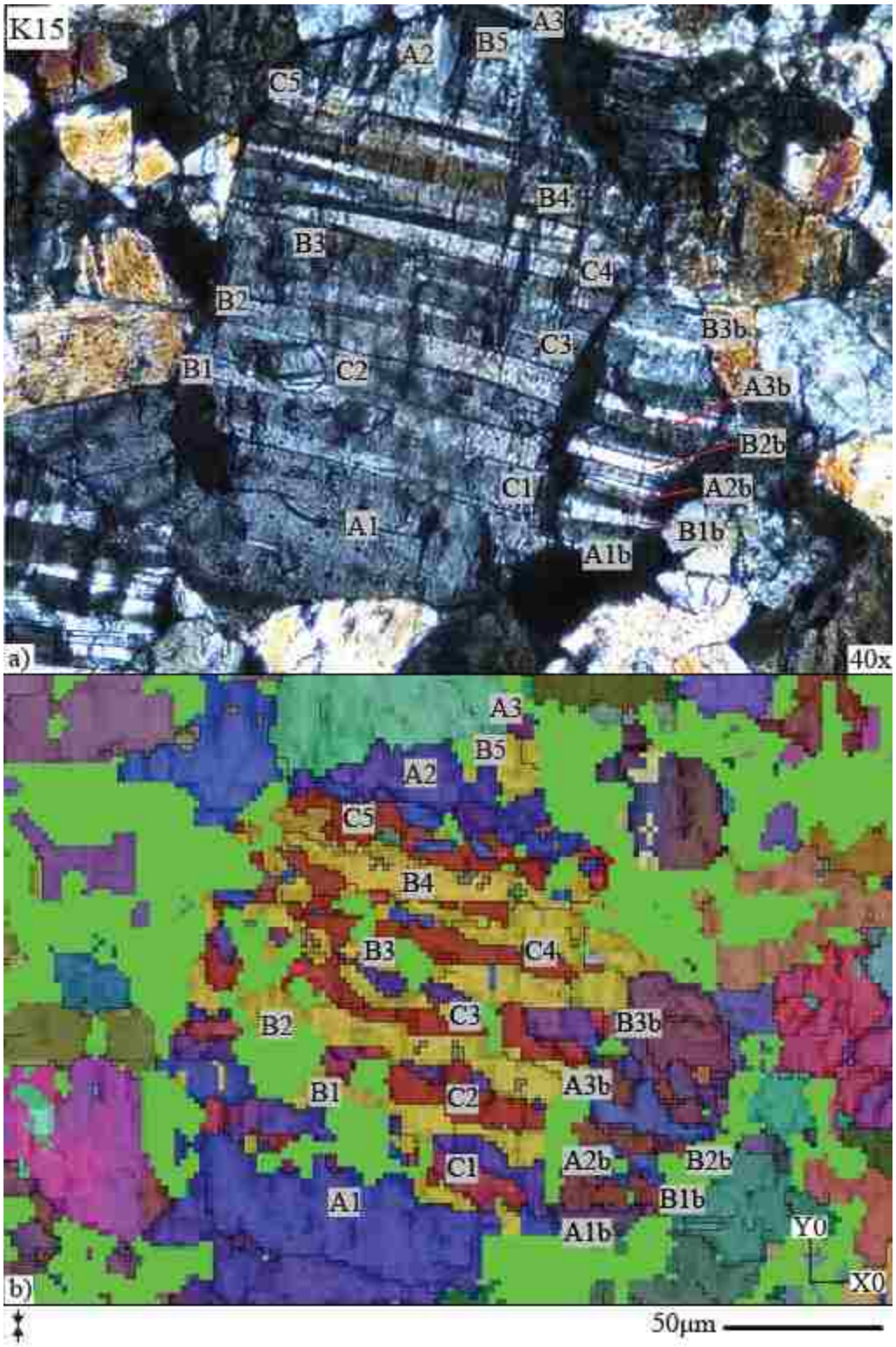

Figure 3.24. Kink band domains for grain K15 in optical and orientation map image. a) optical image of grain K15; b) orientation map image of grain K15.

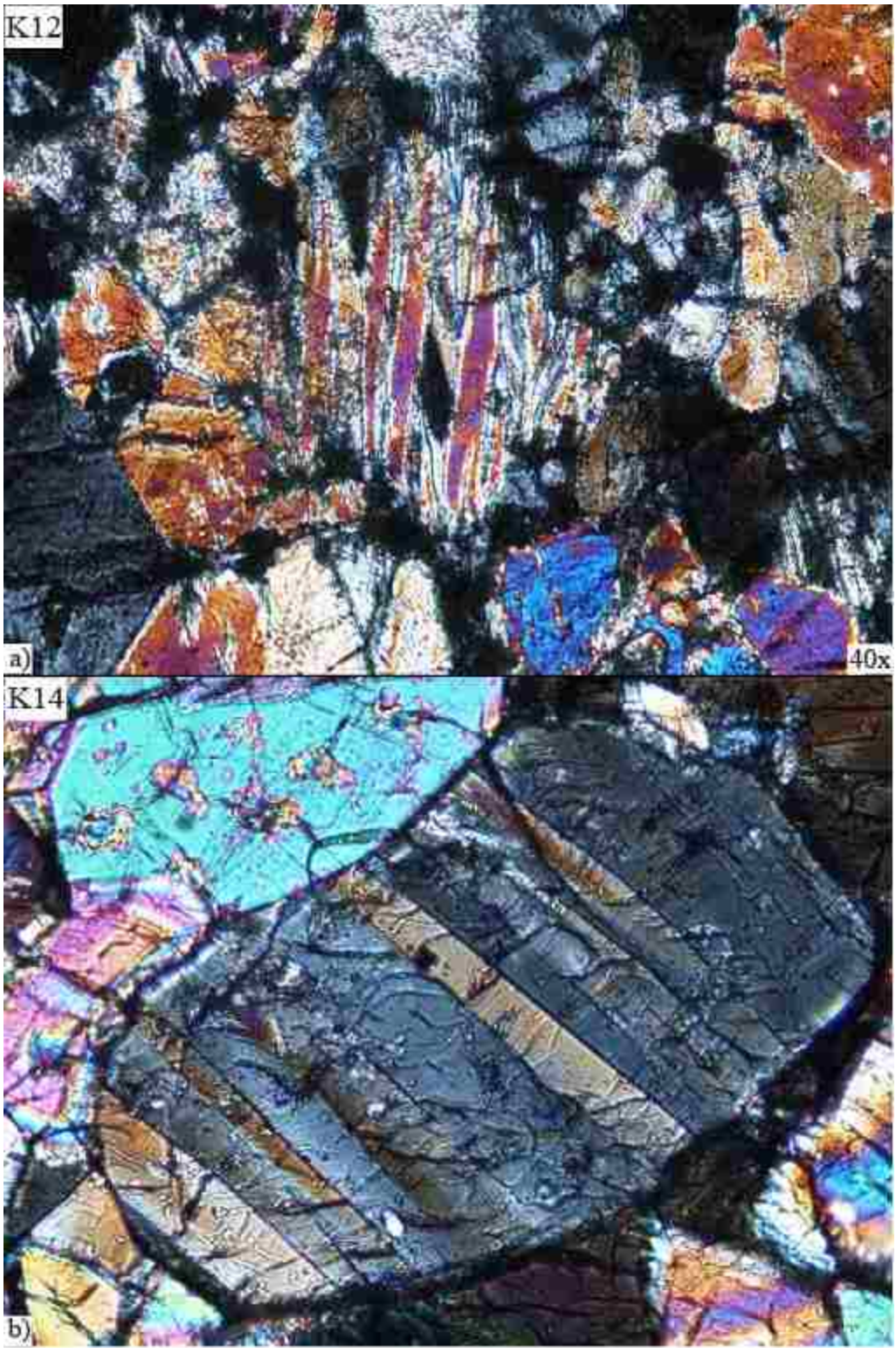

Figure 3.25. Comparison between curved and straight kink band boundaries. a) curved boundaries in grain K14; b) straight boundaries in grain K12.

Sample Coordinate System Orientation Data

All of the pole figures from Mambo of the upper hemisphere for the kinked grains show distinct data clusters for each domain. The orientation relationships between domains are summarized for grain K7 in figure 3.26, which shows pole figures of the scattered data in the sample coordinate system for the following lattice planes: (010), (001), (100), {111}, {110}, {011}, {101}, {201}, {403}, {112}, {120}, and {312}. K7 has two kink domains which are shown by the light grey (domain A) data points and light green data points (domain B) (figure 3.26). In all of the kinked grains, there is an angular separation between the different domains for all of the lattice planes except for (010) (figure 3.26). For the (010) poles, the domains cluster around a point for all of the grains (figure 3.27). This data shows that other lattice planes are rotated about the [010] direction, thus the rotation axis for the kink band domains is [010]. Figures 3.28-3.42 show the scattered data for (010) compared to (001) and (100) for the kinked grains from each orientation map. The number (n) of data points for the kinked grains in the pole figures is also shown in figures 3.28-3.42.

The orientations of the kink band domains for each kinked grain are shown in upper hemisphere pole figures from the refined orientation maps. The (001) and (100) poles provide valuable information about the orientation of the domains with respect to each other. The grains that show two distinct orientations with limited sub-domains in the orientation maps have two distinct data clusters corresponding to each domain that fit a great circle (figure 3.43). For the grains with the expression of additional domains and sub-domains, there are three domain clusters that plot on a great circle. For grain K15, all three domains fit a great circle and one of the three domains (domain A) has an

intermediate orientation that bridges the angular separation between the other two orientations, with the exception of the (010) poles which all overlap. Both grain K5 and K6 have domains with an intermediate orientation, but in grain K6, the intermediate sub-domain plots closer to the pink orientation in domain B with respect to the other two domains. The sub-orientations in K8 and K9 have the highest rotation angles of the scattered data within their domains. Figure 3.44 summarizes the orientation relationships of the domains and sub-domains for grains K5, K6, K8, K9, and K15.

Contoured pole figures provide useful bulk measurements for the amount of lattice plane rotation between kink band domains. For grains with an angular spread, contour maps show where the highest density of data points for each domain plot. For the kinked grains, each domain showed an area with a peak density of data points compared to the background corresponding to a specific kink band domain. The rotation angle or kink band angle that was measured between each domain for (100) using contoured pole figures from Mambo is shown in table 3.2. The kinked grains show a range of angles. There are kinked grains with lower kink angles between opposite orientations that fall into the range of 15º to 30º. These grains include: K8, K10, K11, K13, and K14. The grains with a higher rotation angle have rotation angles above 35º. These grains include: K1, K2, K3, K4, K5, K6, K7, K9, K11, K12, and K15. Grain K12 has the highest kink angle with a value of 68º. Figure 3.45 shows the contour pole figures for the (100) lattice plane for all of the kinked grains.

The (010) pole orientations for all of the kinked grains are summarized in figure 3.46 with respect to the compression axis. Each pole on figure 3.46 is a point measurement made using **010·X0** and **010·Z0** measurements in Mambo that was plotted in StereoWin

Table 3.2. Kink angle measured using contoured pole figures of (100)

Grain	AB (º)	AC (º)	BC (º)
K1	37.61	...	...
K2	46.66	...	...
K3	46.32	...	...
K4	47.62	...	...
K5	41.55	...	...
K6	47.13	...	...
K7	54.04	...	...
K8	18.79	...	...
K9	51.13	...	...
K10	28.20	...	...
K11	41.10	...	...
K12	68.20	...	...
K13	26.04	...	...
K14	21.36	...	...
K15	19.28	29.55	46.16

1.2. The **010·X0** and **010·Z0** measurements are summarized in table 3.3. The (010) poles for the kinked grains plot semi-parallel with the Y0 axis away from compression direction indicating that the plane of shear for the kinked grains is sub parallel with the compression axis in the sample coordinate system (figure 3.46). Figure 3.47 shows the orientation of the axial planes, which contain the (010) poles and the trace of the kink bands. There is some variation in the orientation of the axial planes and the angle from X0 varies from 0º in grain K11 to 38º for grain K5. Most grains have axial planes that plot close to X0, with 12 out 15 axial planes having an orientation less than 30º from X0. All of the axial planes are steeply inclined from the compression direction. The inclination of the axial planes from the X0Y0 plane ranges from 51º to 87º with an average inclination of 68º from the X0Y0 plane.

Table 3.3. Angular measurements made in Mambo to define (010) pole orientations

Grain	**010·X0** (º)	**010·Z0** (º)
K1	87	49
K2	56	51
K3	78	43
K4	58	70
K5	42	64
K6	73	57
K7	58	76
K8	73	71
K9	67	90
K10	52	68
K11	63	44
K12	64	33
K13	45	52
K14	59	47
K15	85	77

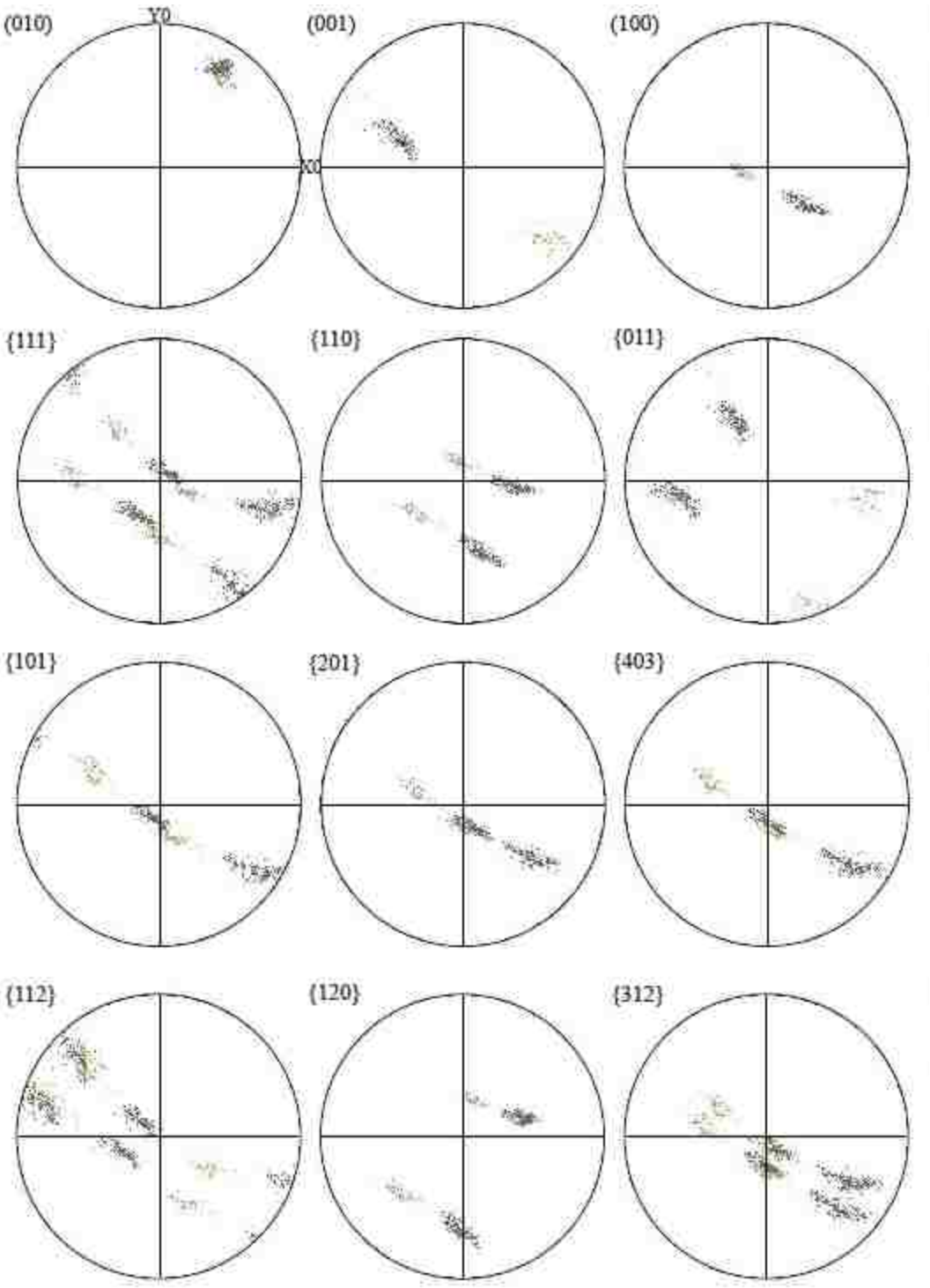

Figure 3.26. Upper hemisphere stereographic projection for selected lattice planes for grain K7.

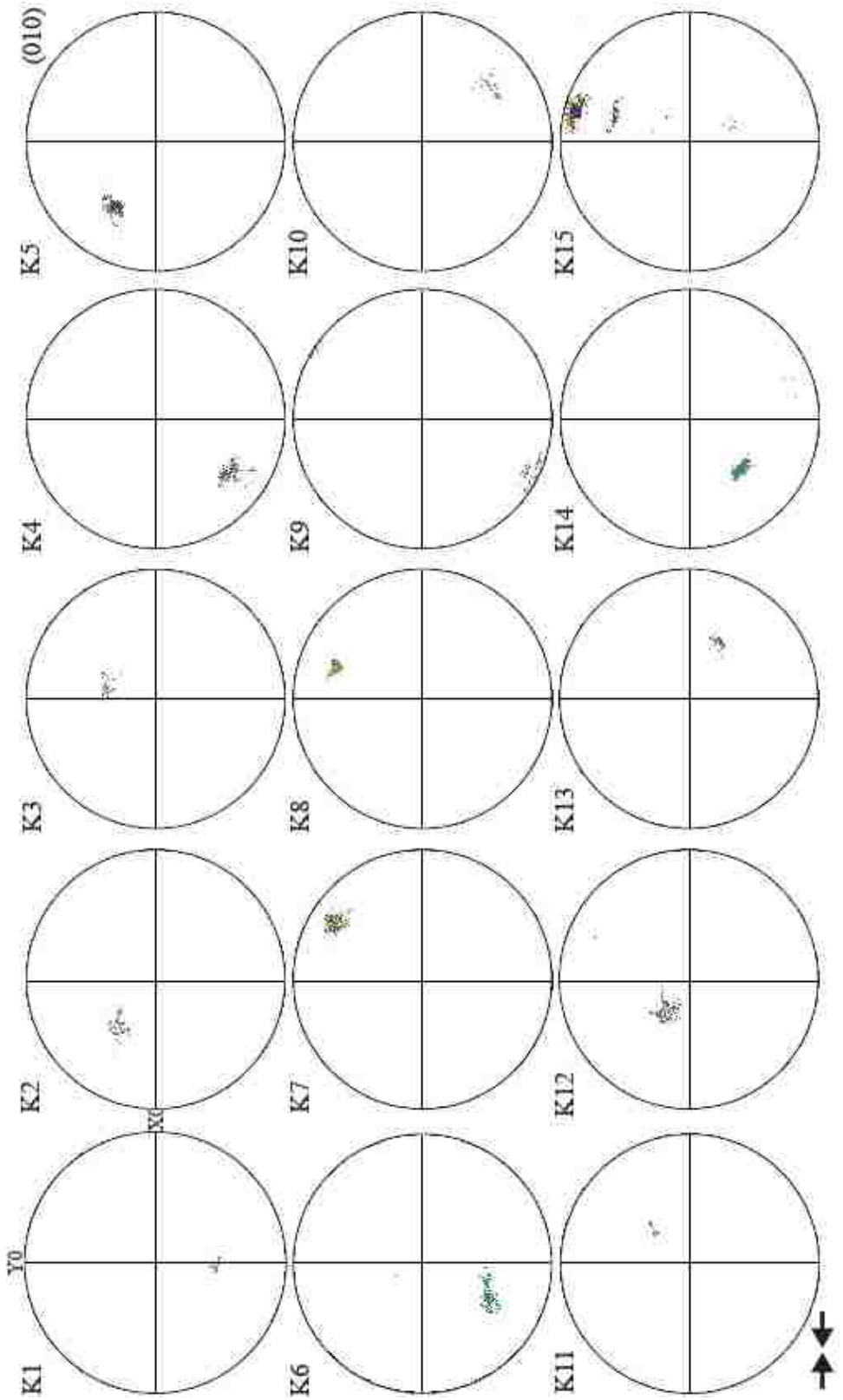

Figure 3.27. Upper hemisphere stereographic projection for (010) poles for all grains with respect to compression direction.

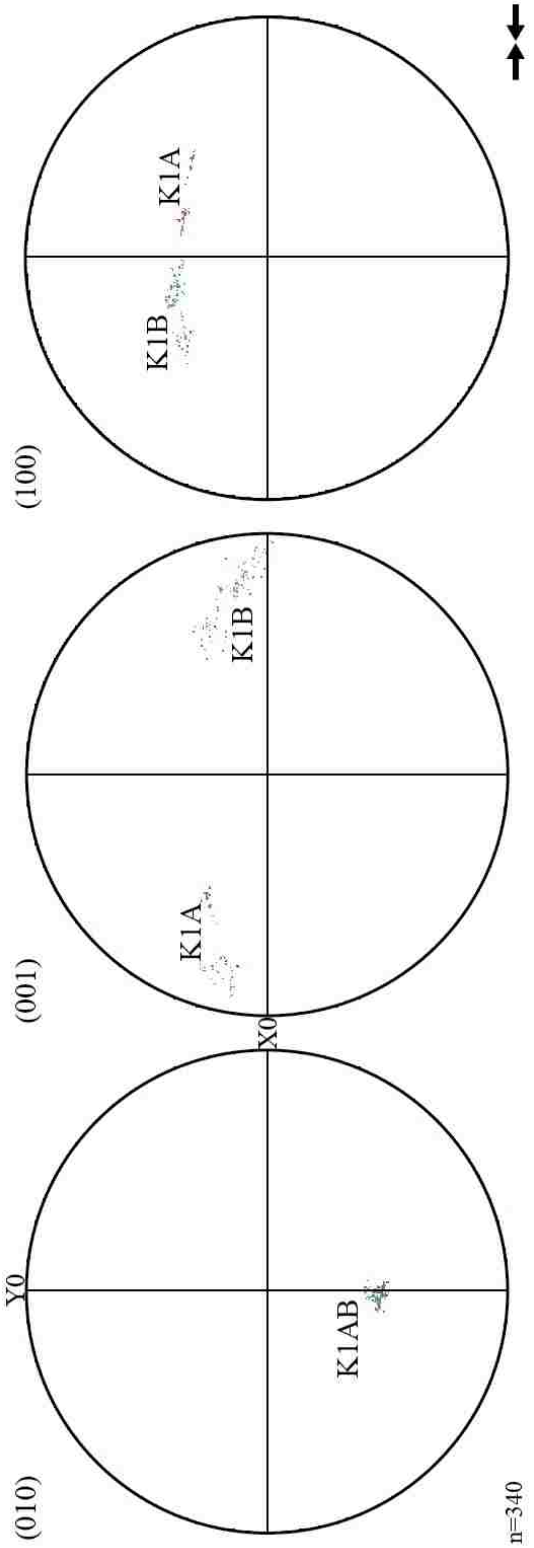

Figure 3.28. Upper hemisphere stereographic of (010), (001), and (100) for grain K1.

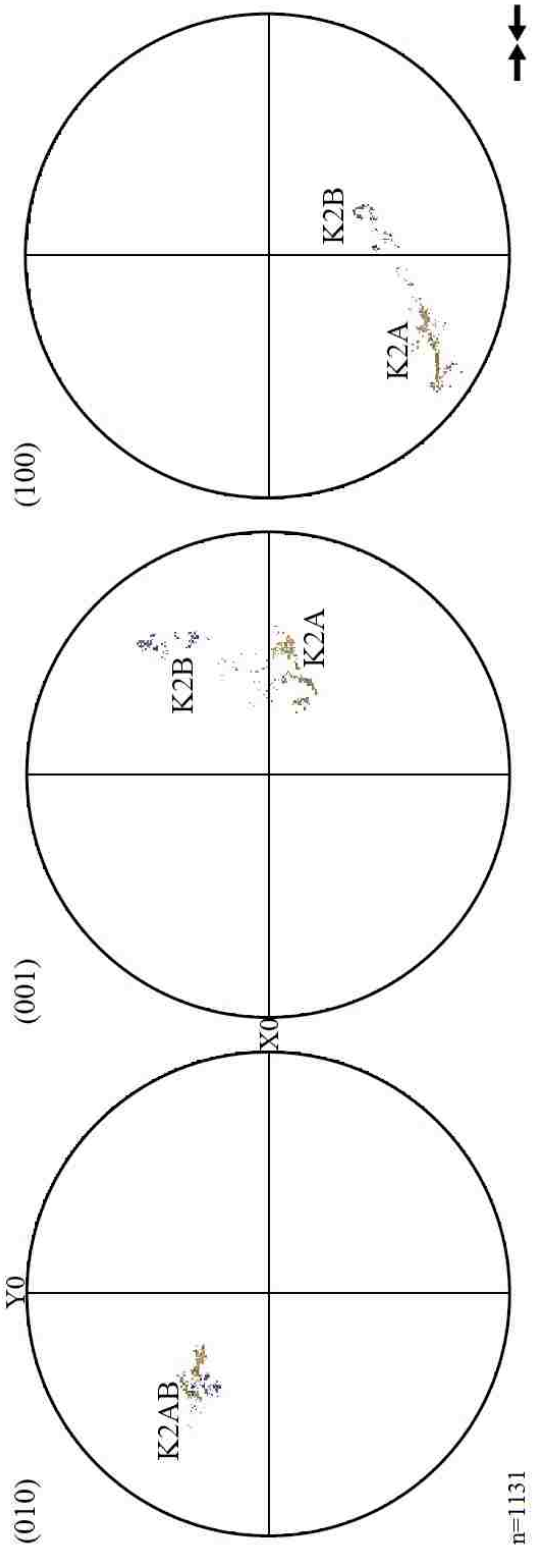

Figure 3.29. Upper hemisphere stereographic of (010), (001), and (100) for grain K2.

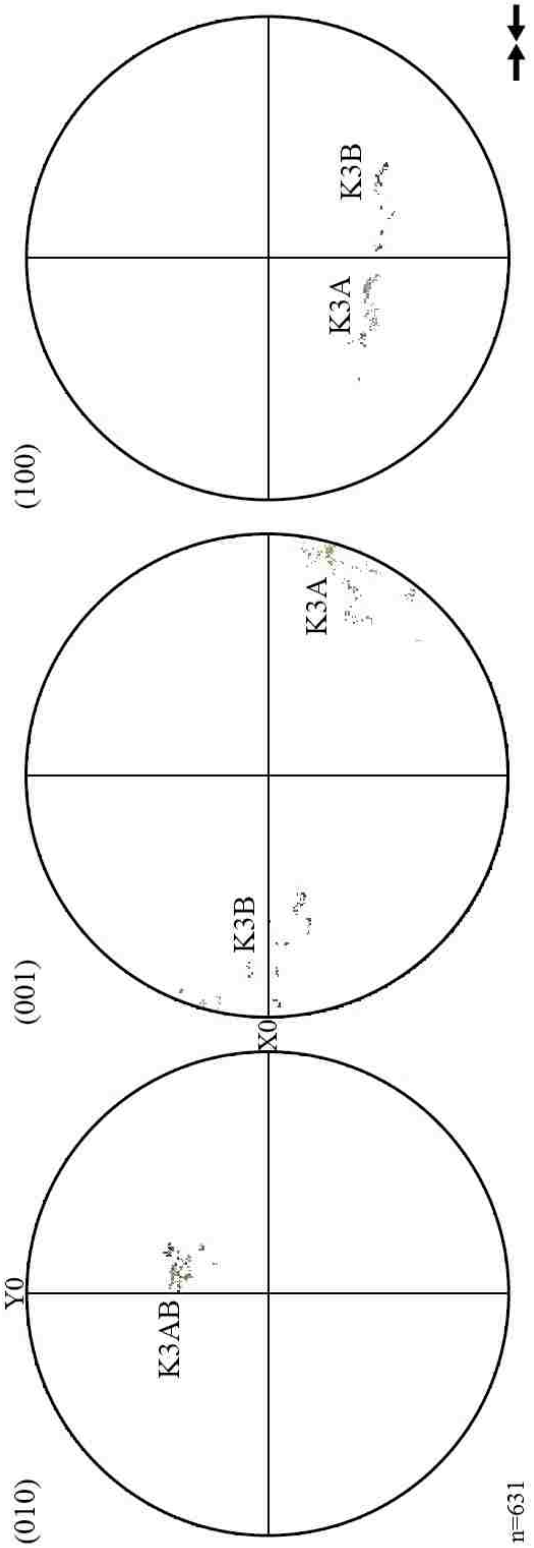

Figure 3.30. Upper hemisphere stereographic of (010), (001), and (100) for grain K3.

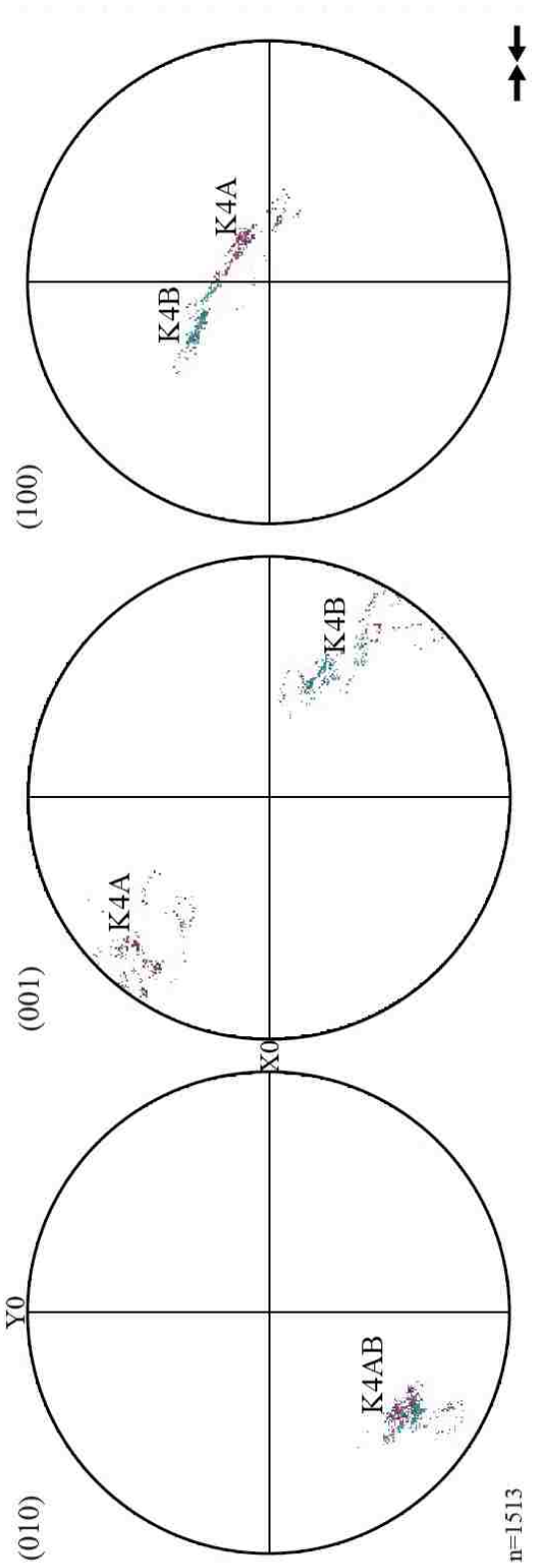

Figure 3.31. Upper hemisphere stereographic of (010), (001), and (100) for grain K4.

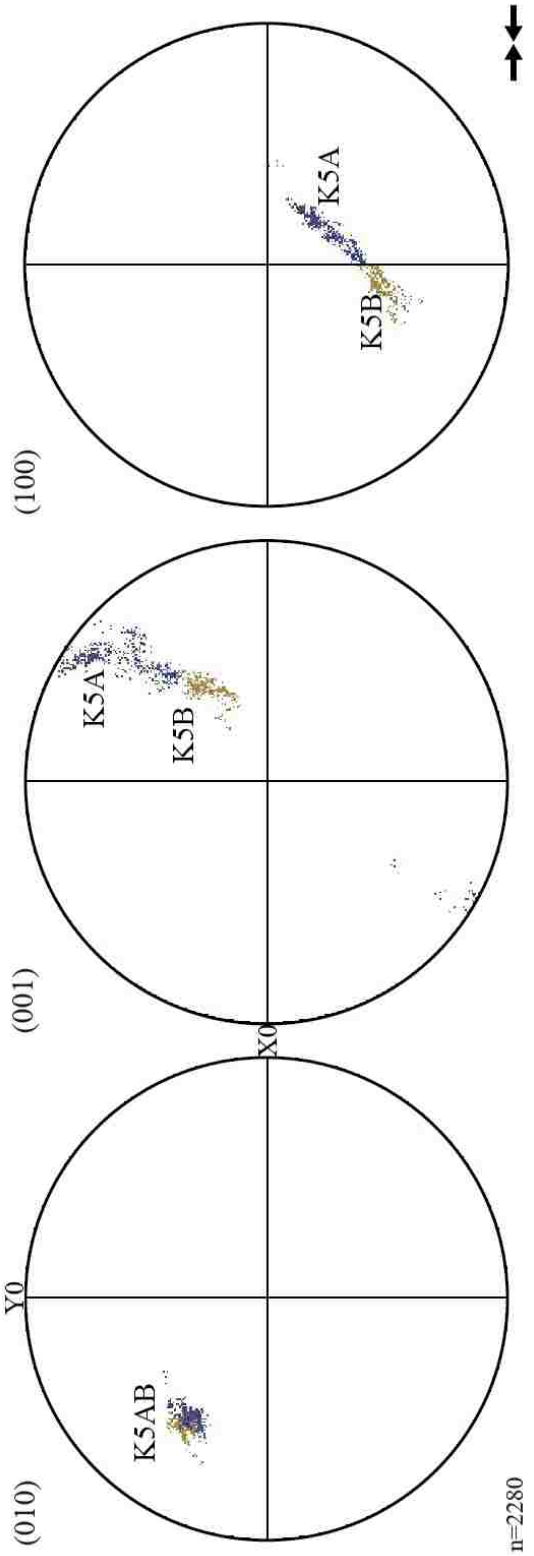

Figure 3.32. Upper hemisphere stereographic of (010), (001), and (100) for grain K5.

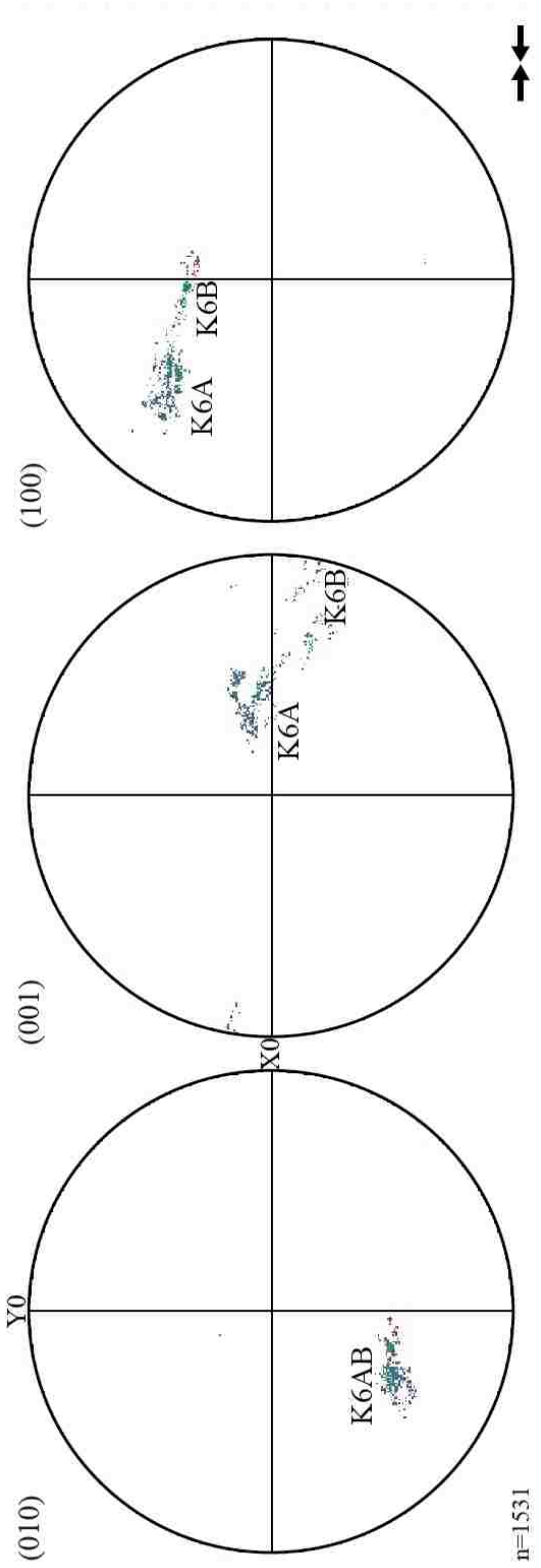

Figure 3.33. Upper hemisphere stereographic of (010), (001), and (100) for grain K6.

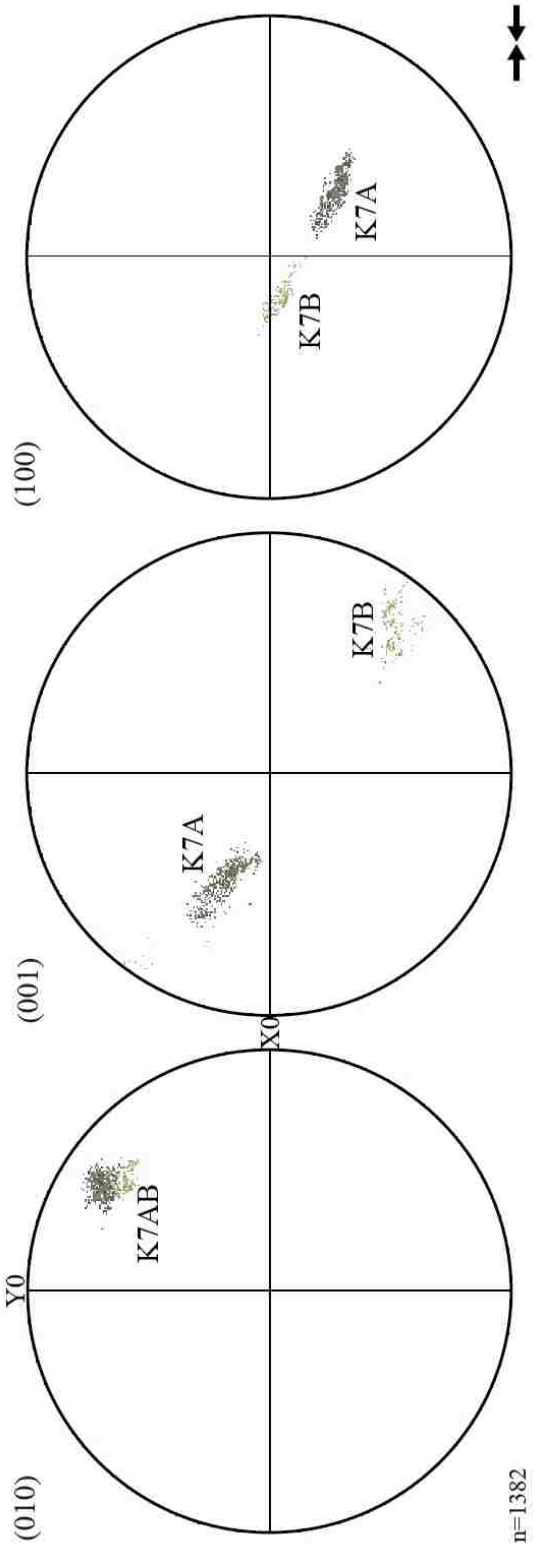

Figure 3.34. Upper hemisphere stereographic of (010), (001), and (100) for grain K7.

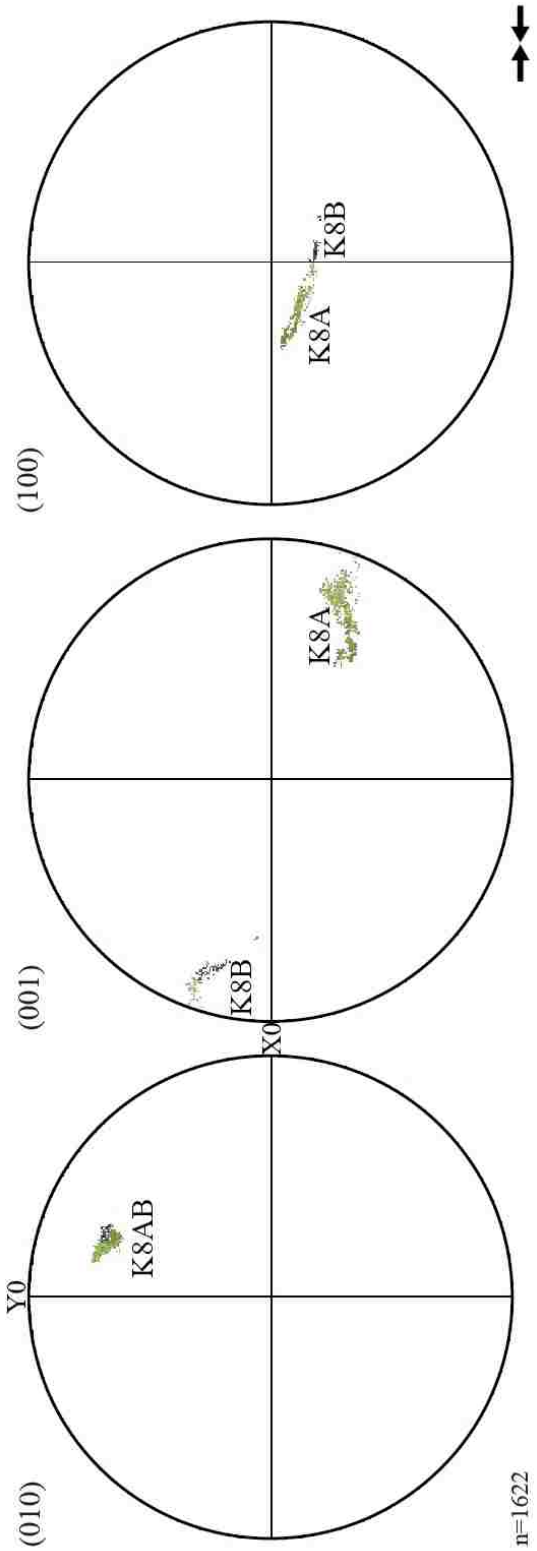

Figure 3.35. Upper hemisphere stereographic of (010), (001), and (100) for grain K8.

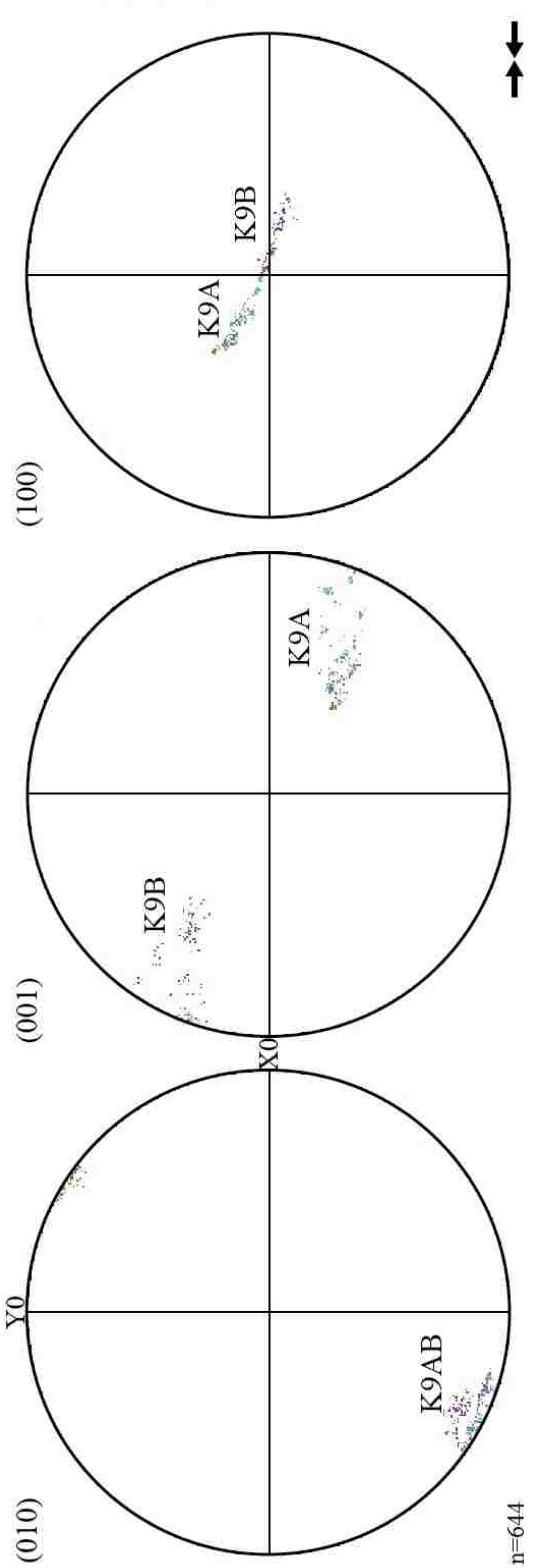

Figure 3.36. Upper hemisphere stereographic of (010), (001), and (100) for grain K9.

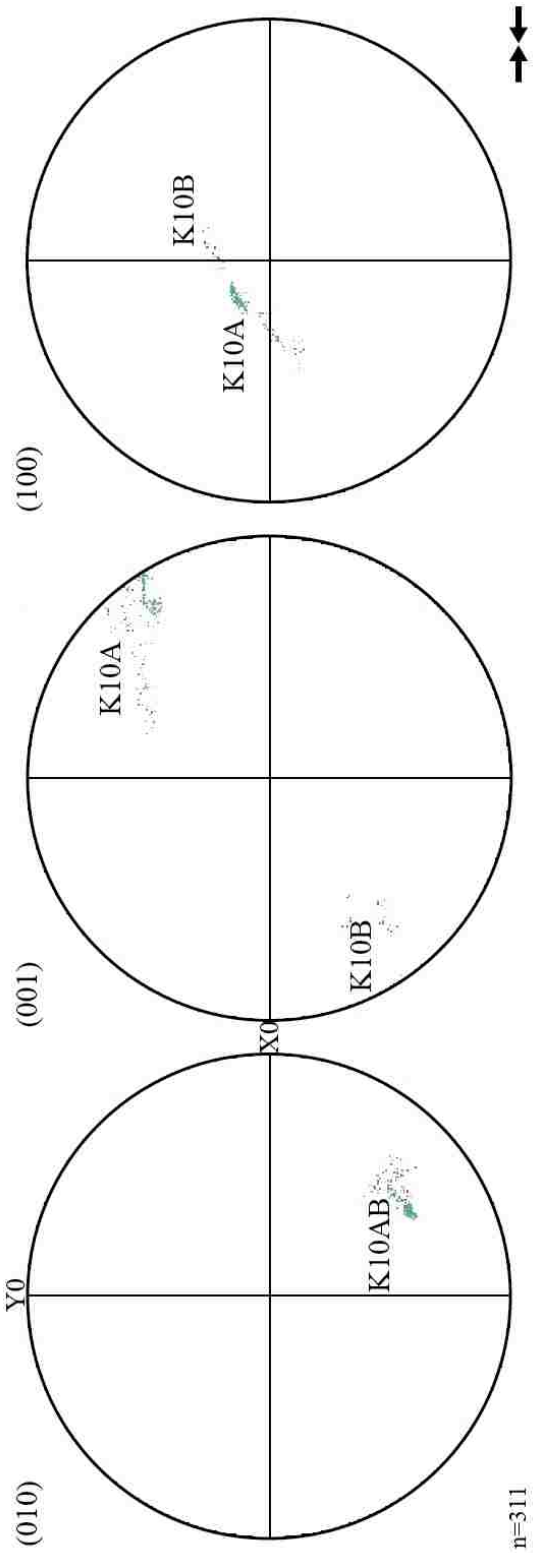

Figure 3.37. Upper hemisphere stereographic of (010), (001), and (100) for grain K10.

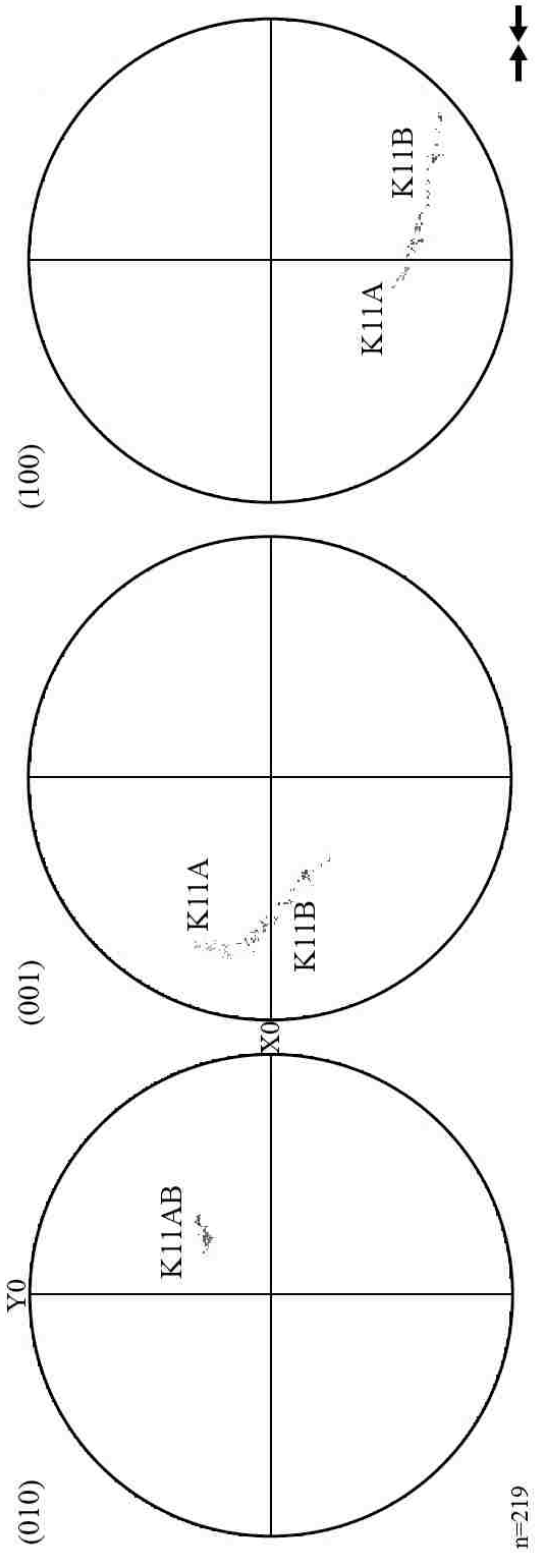

Figure 3.38. Upper hemisphere stereographic of (010), (001), and (100) for grain K11.

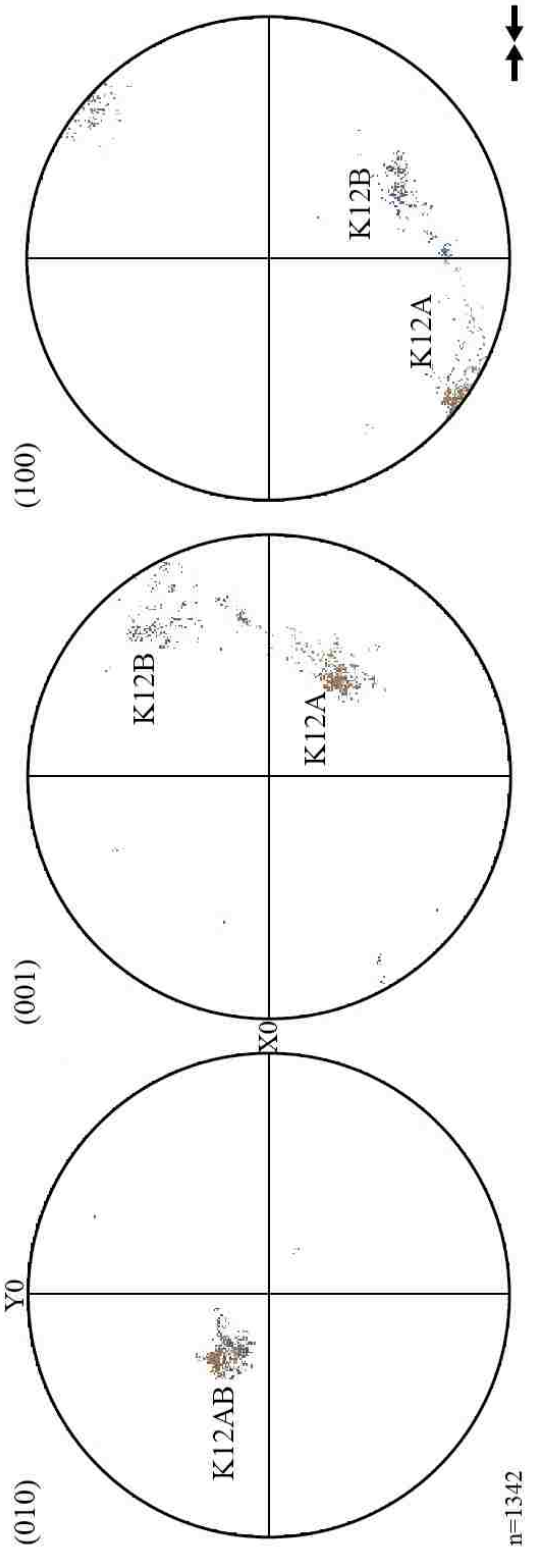

Figure 3.39. Upper hemisphere stereographic of (010), (001), and (100) for grain K12.

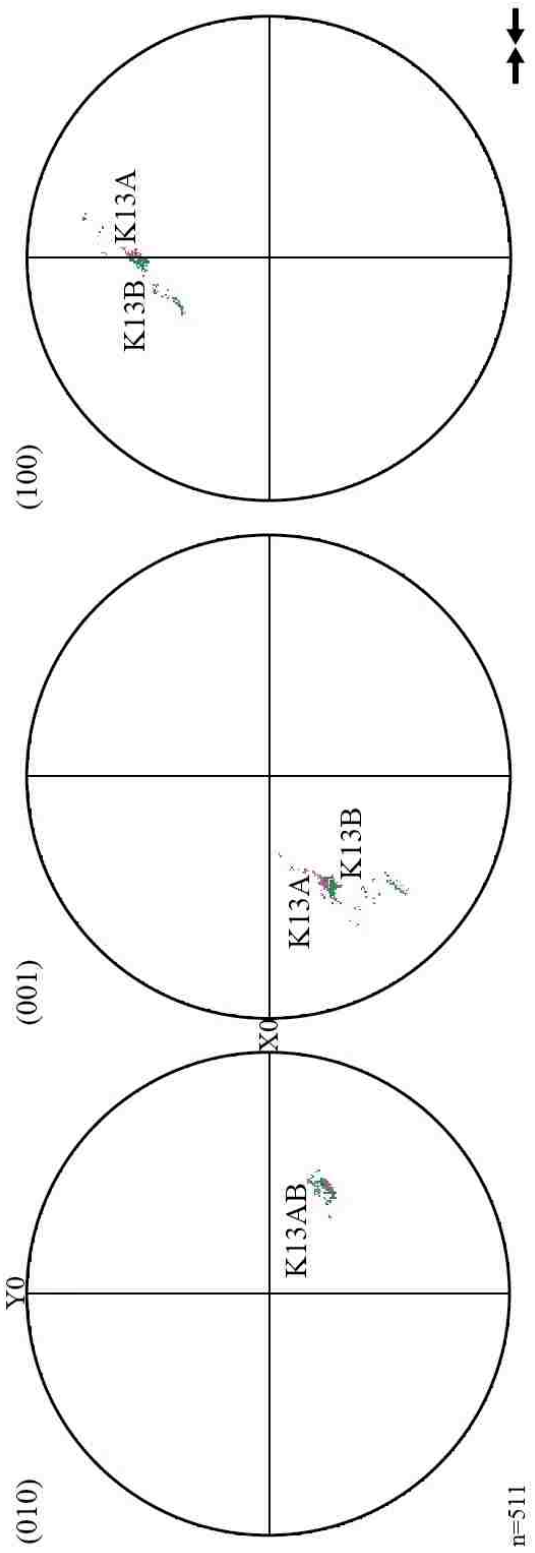

Figure 3.40. Upper hemisphere stereographic of (010), (001), and (100) for grain K13.

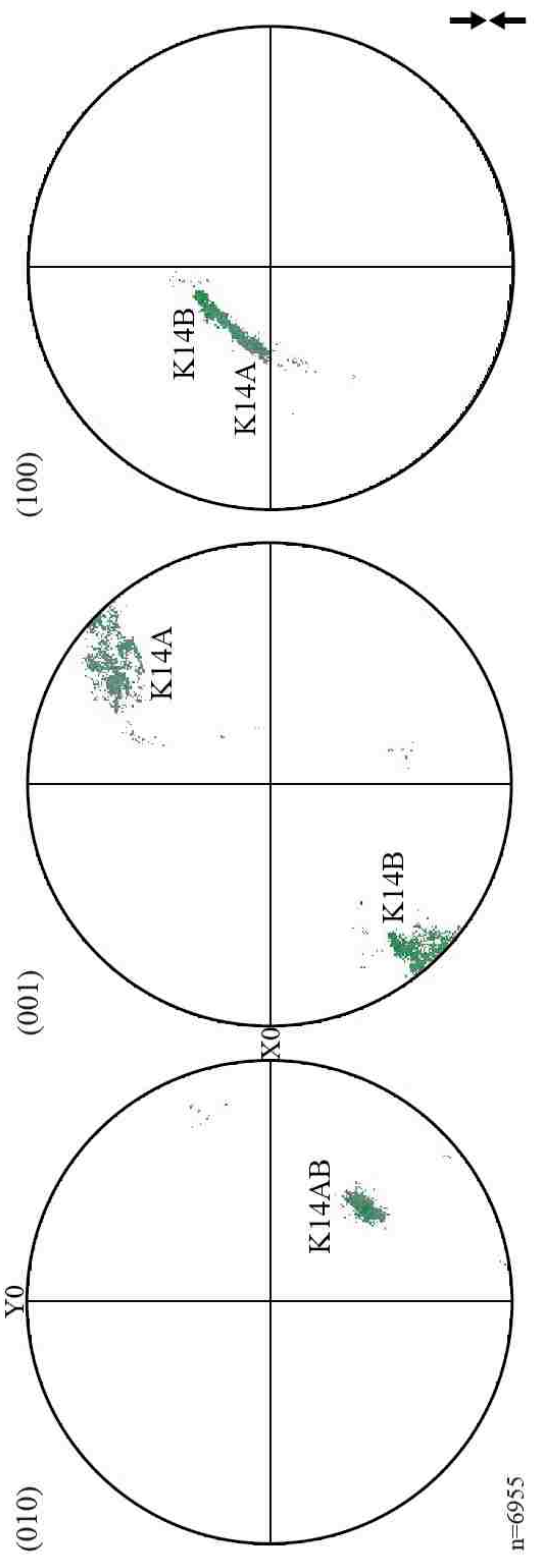

Figure 3.41. Upper hemisphere stereographic of (010), (001), and (100) for grain K14.

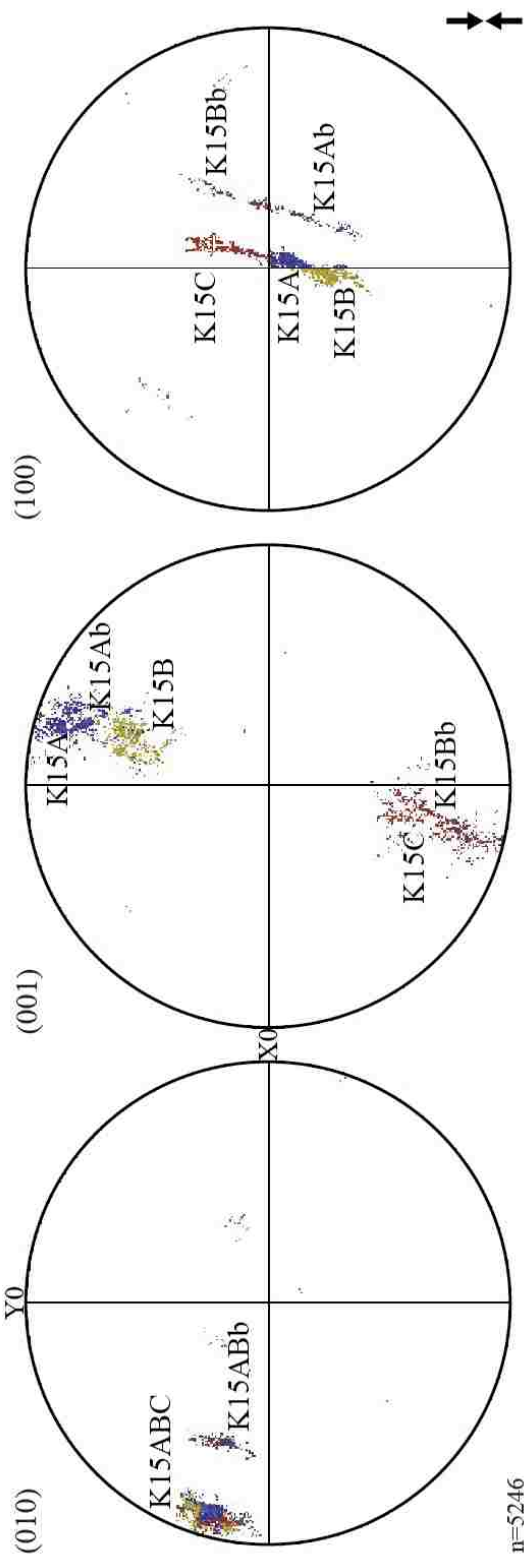

Figure 3.42. Upper hemisphere stereographic of (010), (001), and (100) for grain K15.

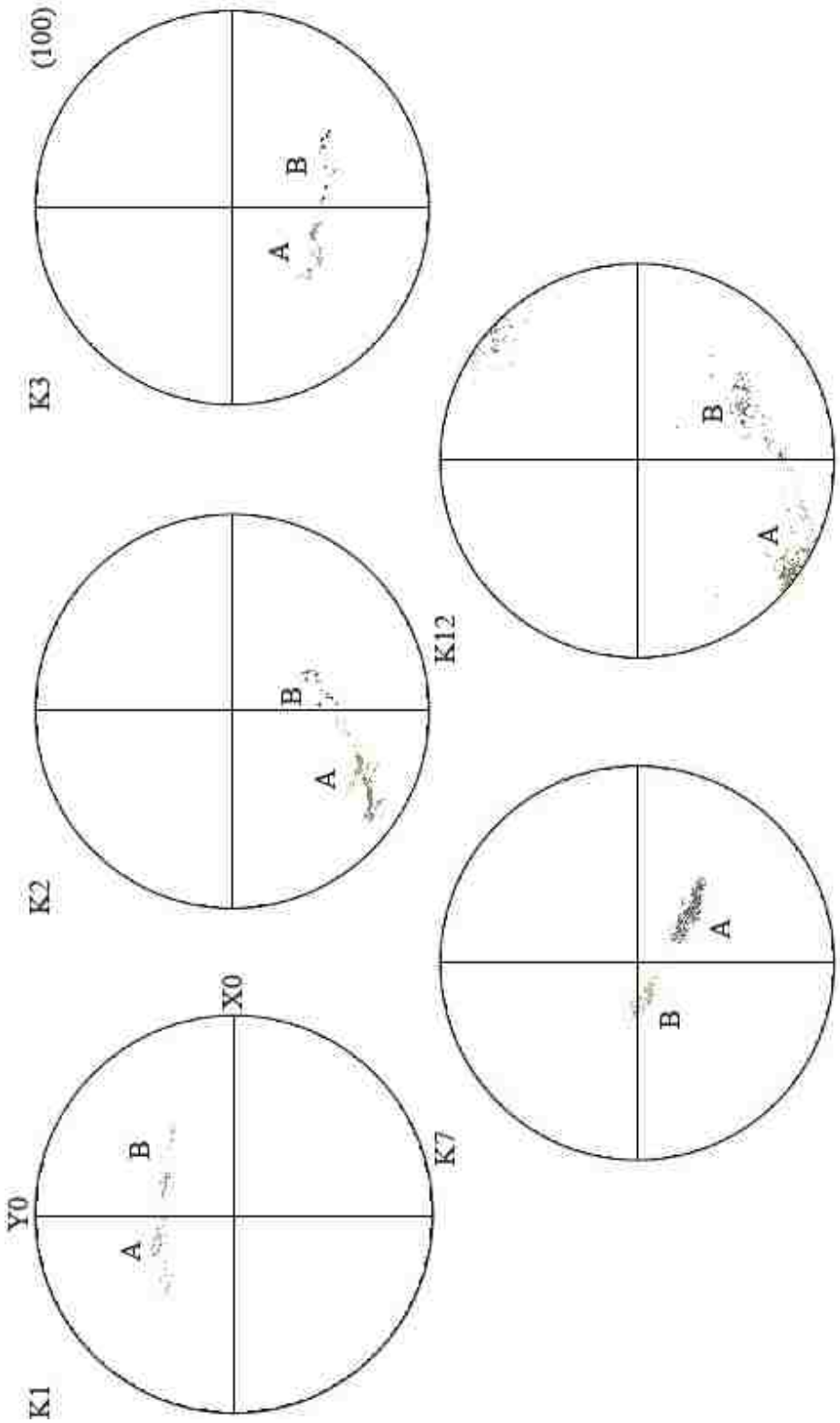

Figure 3.43. Upper hemisphere stereographic projection for grains with two domains (100).

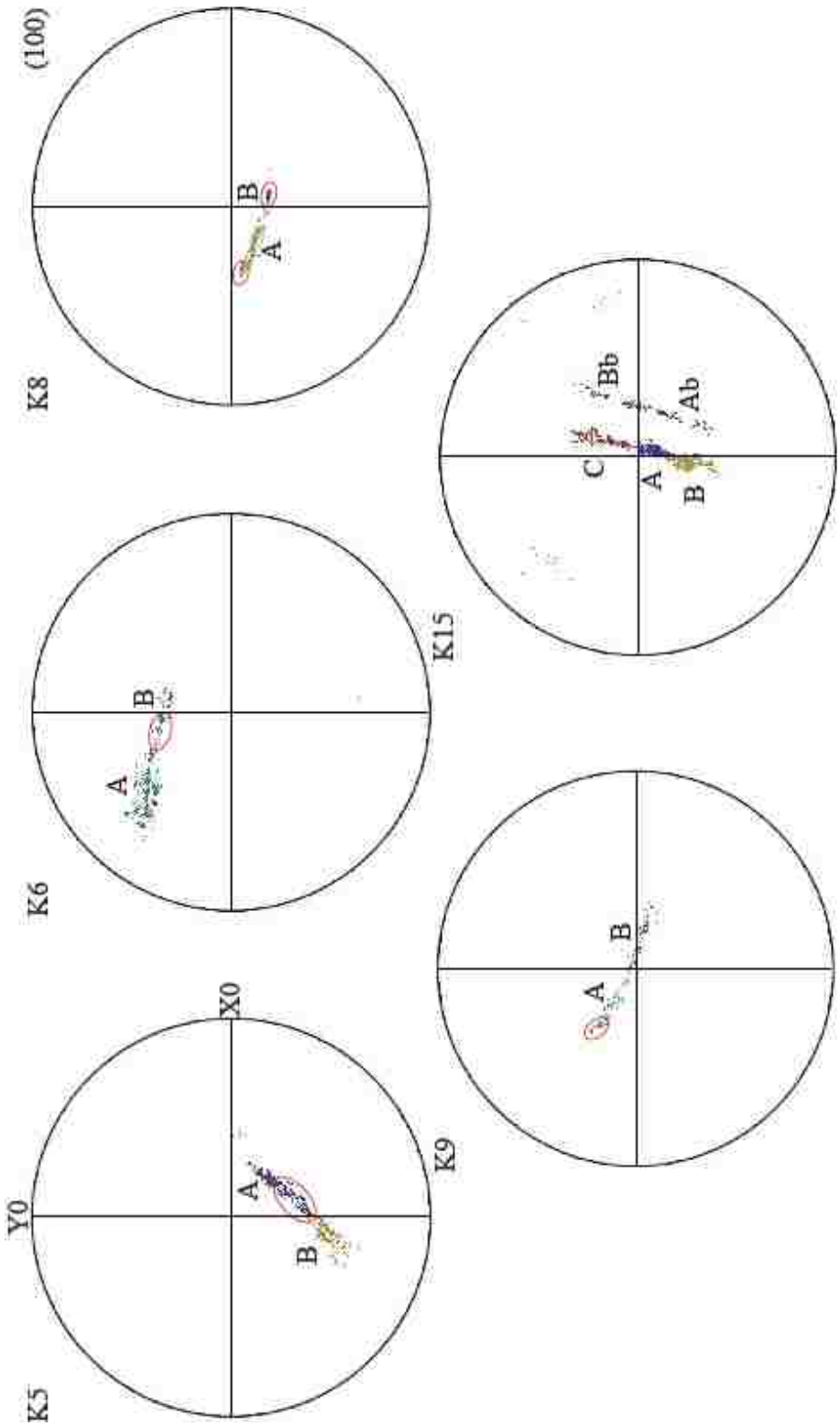

Figure 3.44. Upper hemisphere stereographic projection of grains with two domains that have sub-domains (100).

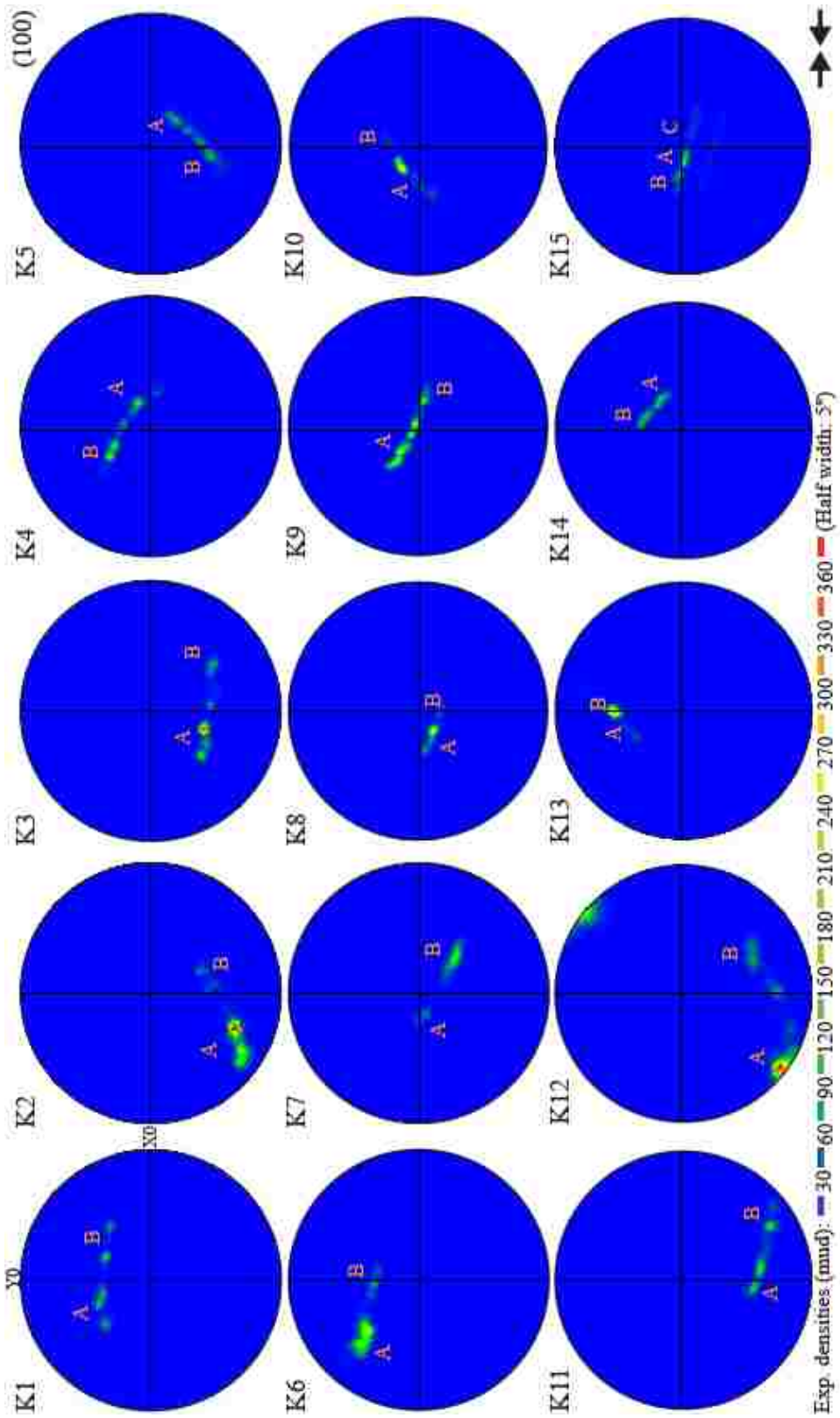

Figure 3.45. Contoured upper hemisphere stereographic projection for (100) with domains shown with respect to compression.

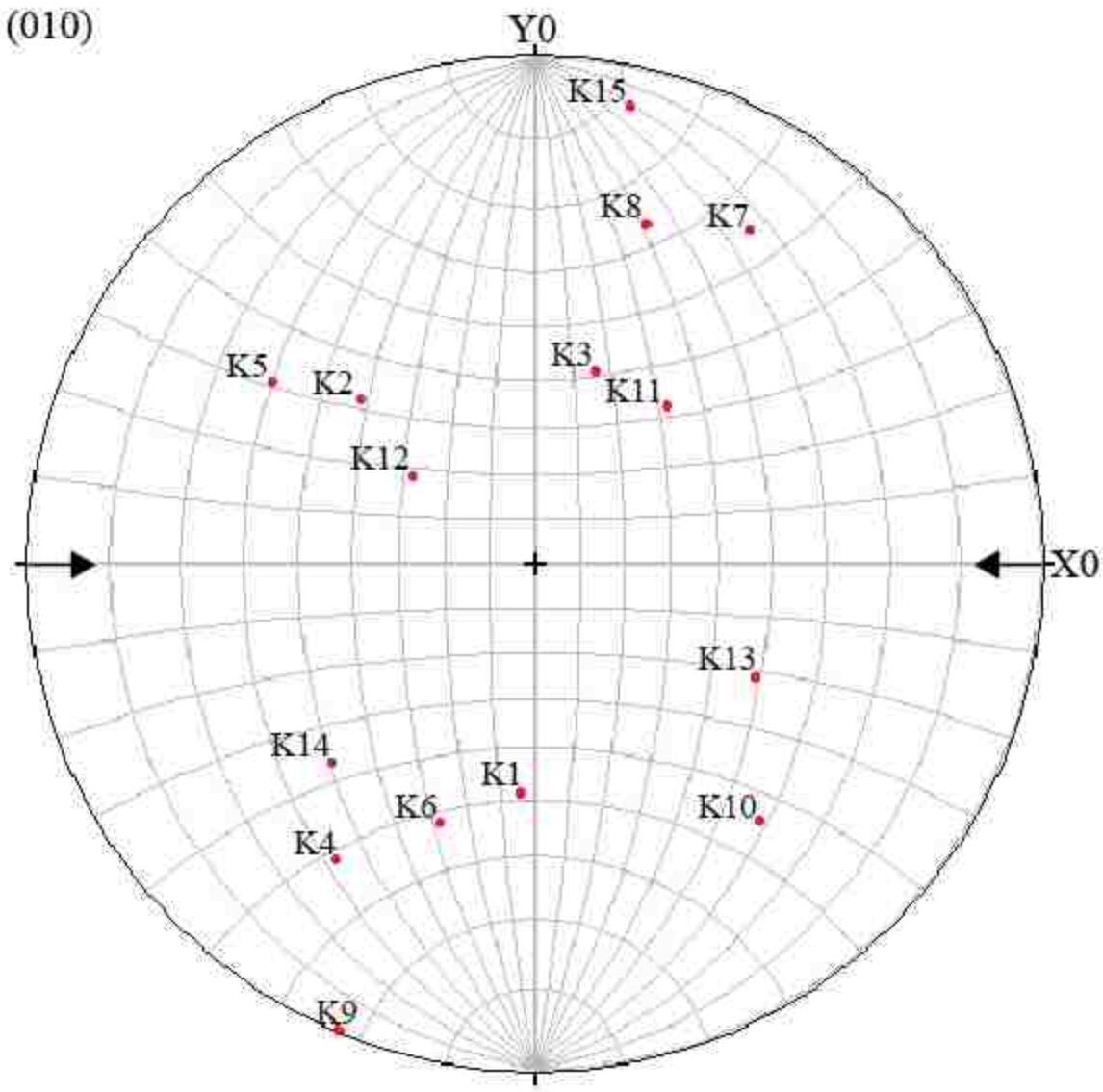

Figure 3.46. Upper hemisphere stereographic projection of rotation axis for kinked grains with respect to compression (grain K14 and grain K15 poles have been rotated 90º to align the compression direction with the compression direction for the kinked grains from sample GL330).

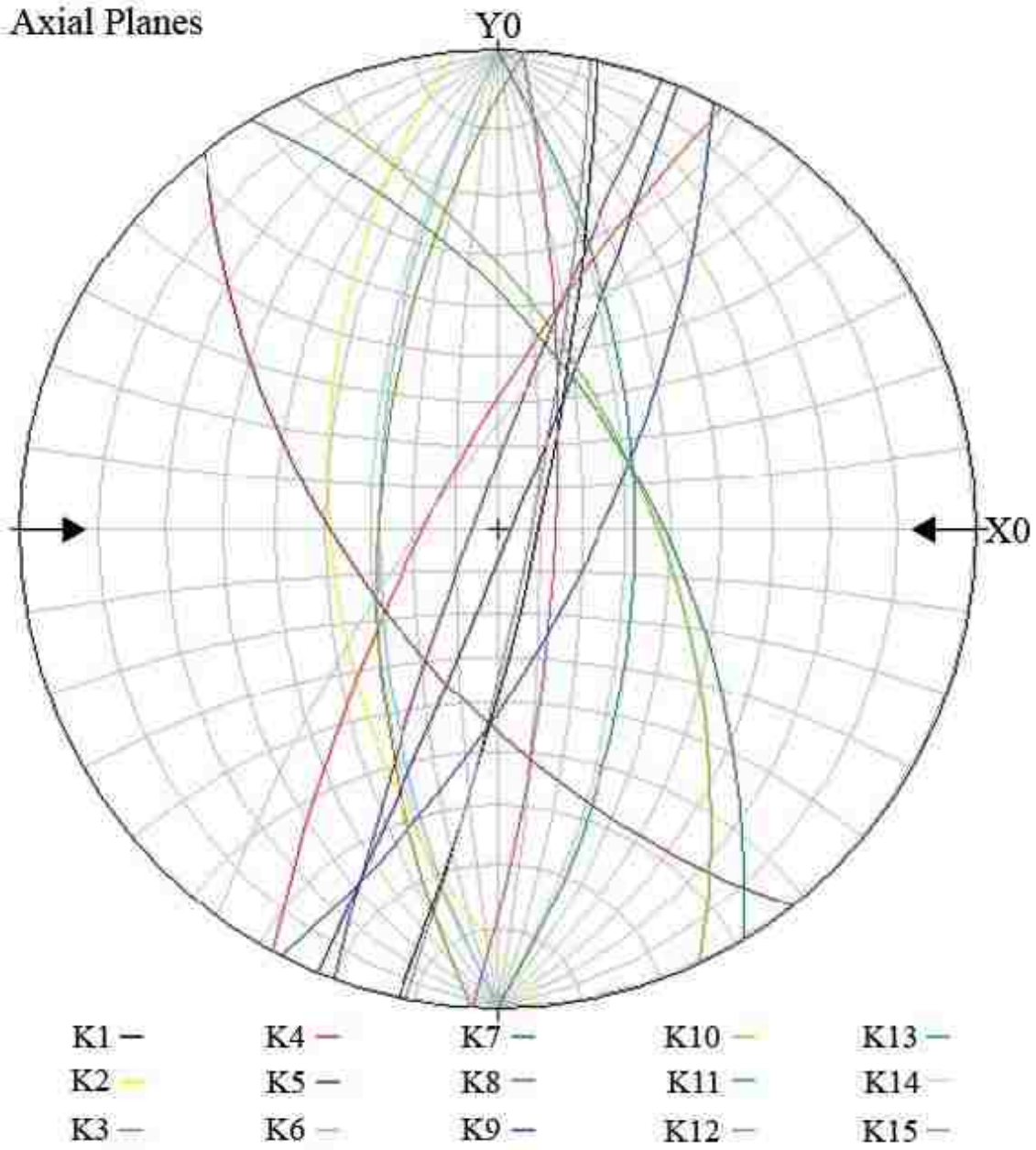

Figure 3.47. Upper hemisphere stereographic projection of the orientation of axial planes with respect to compression axis (axial planes for grain K14 and grain K15 have been rotated 90º to align the compression direction with the compression direction for the kinked grains from sample GL330).

Crystal Coordinate System Orientation Data

The poles to the axial planes plot sub parallel to the [001] direction. Figures 3.48-3.50 show a summary of the axial planes, axial poles (AP), and the three principle directions of a subset from one domain for each kinked grain. The trace measurement (T) and the pole to (010) for each grain are also included in the diagrams. Most axial poles plot closer the [001] direction than the [100] direction, thus slip in the [001] direction is inferred. Grains with lower kink angles have axial poles that plot closer to the slip direction.

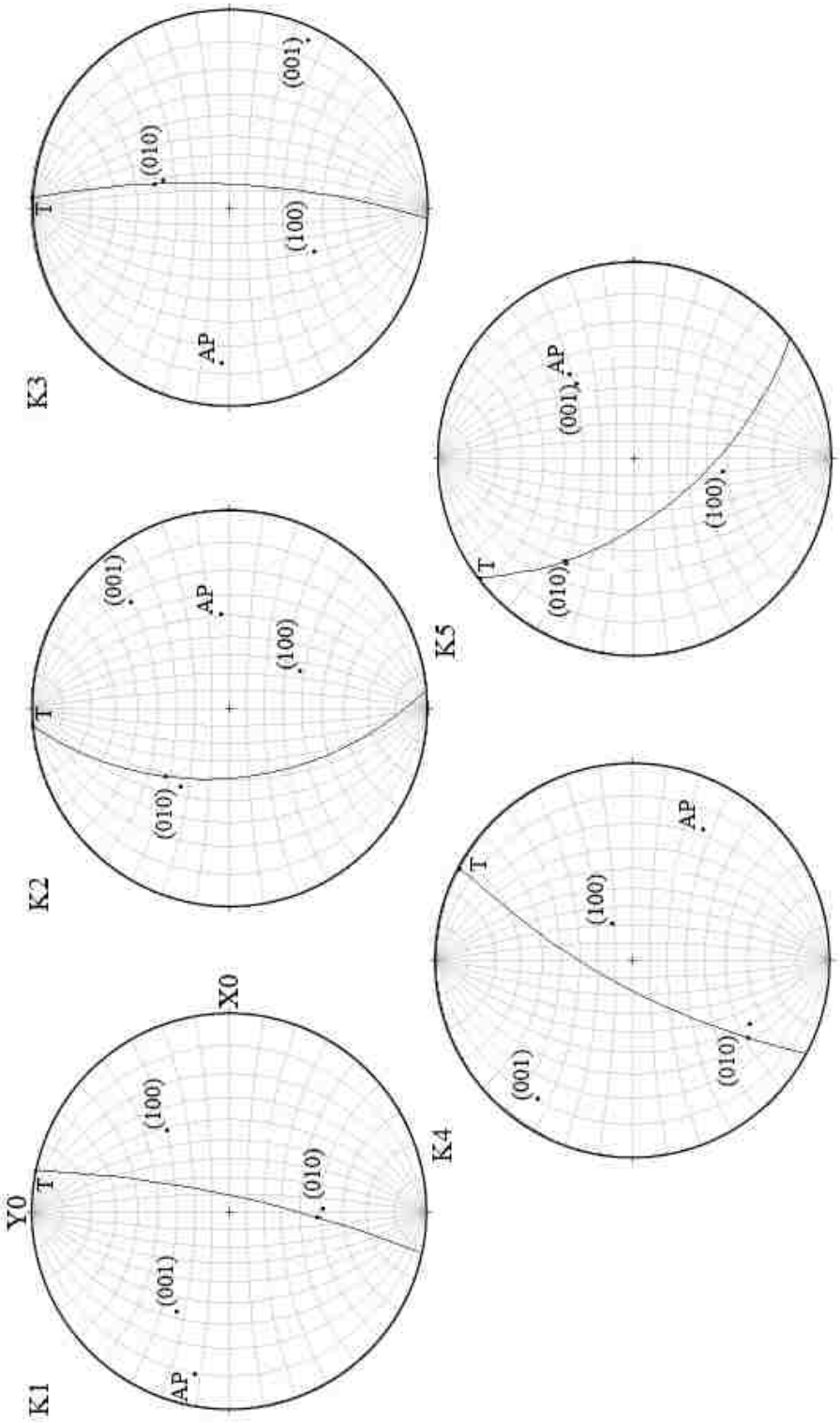

Figure 3.48. Axial poles and crystallographic directions for grains K1-K5.

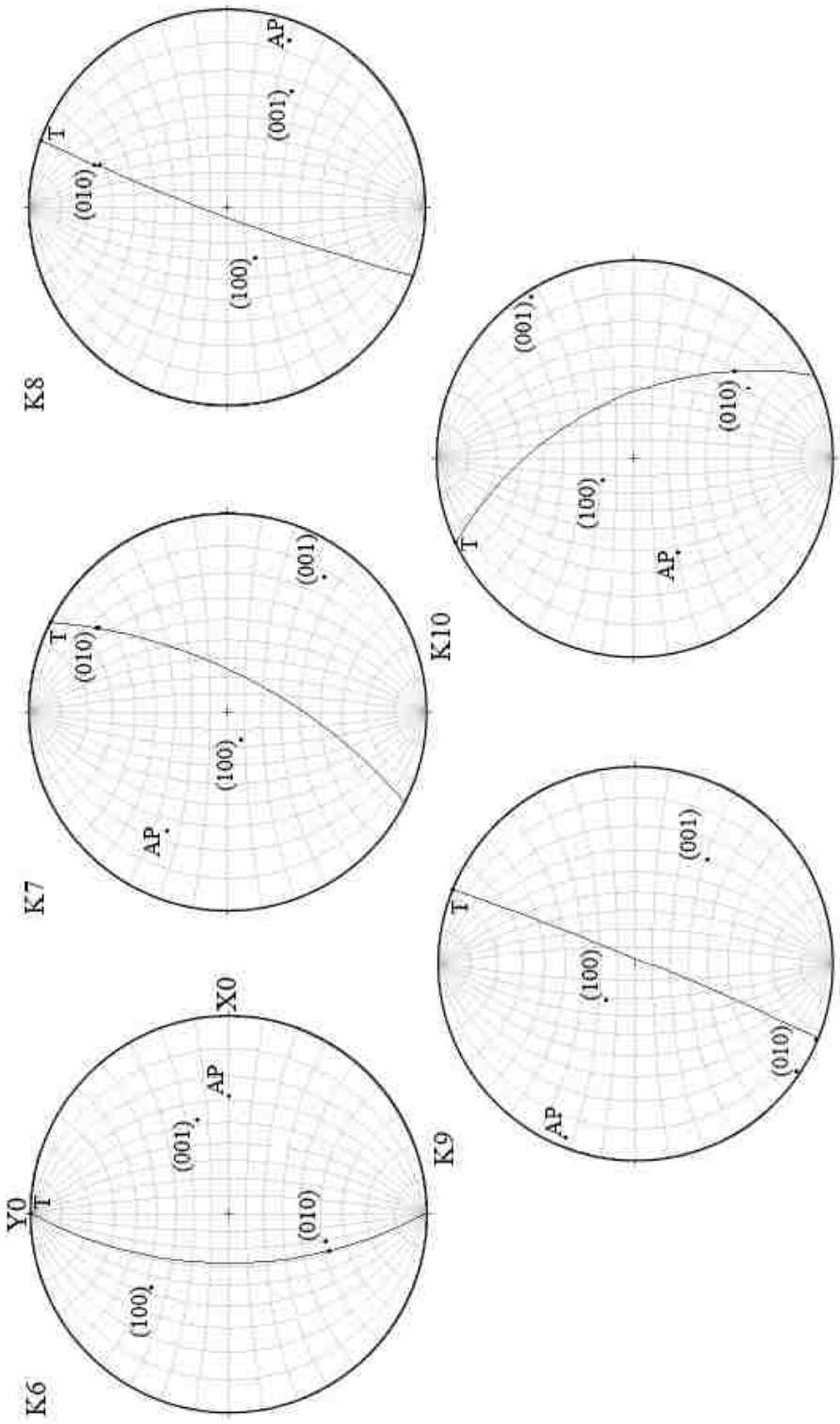

Figure 3.49. Axial poles and crystallographic directions for grains K6-K10.

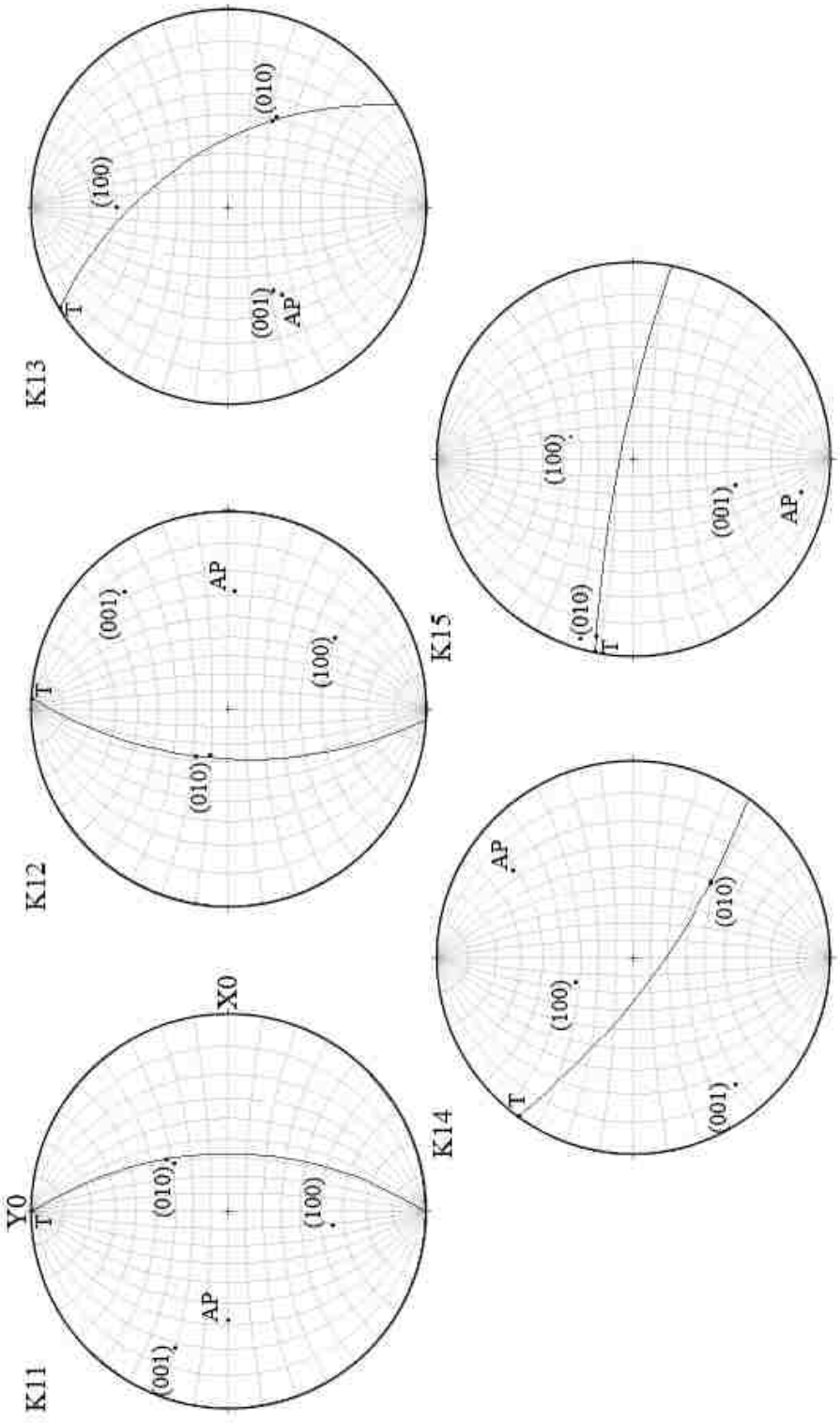

Figure 3.50. Axial poles and crystallographic directions for grains K11-K15.

Misorientation Angle Data

Misorientation data for kinked grains and control grains

The misorientation angle histograms from the kinked grains have a different misorientation distribution compared to control grains without kinking. The misorientation frequency distribution is shown for misorientation angles measured for eight neighboring (correlated) data points for each data point in the kinked grains. The misorientation profiles show frequency vs. misorientation angle. The frequency describes the occurrence of misorientation measurements in 5º bins relative to the total number misorientation measurements within a grain. For each type of grain, the 0º to 5º range has the highest frequency. Figure 3.51 and figure 3.52 show an example of each type of misorientation profile, for grain K7 and grain G1 respectively. All of the misorientation angles for grain G1 are less than 5º, while grain K7 shows some higher misorientation angles. Figure 3.53 shows a cumulative histogram with data points from all of the kinked and control grains. The highest frequency of misorientations is in the 0º to 5º range, while a higher percentage of misorientation angles are in the 0º to 5º range for the control grains compared to the kinked grains. It is unclear at which angular interval the data points along the kink band boundaries start to contribute to the frequency more than the data points that lie in between the kink band boundaries. There is no preferred misorientation angle for higher misorientations in the kinked grains.

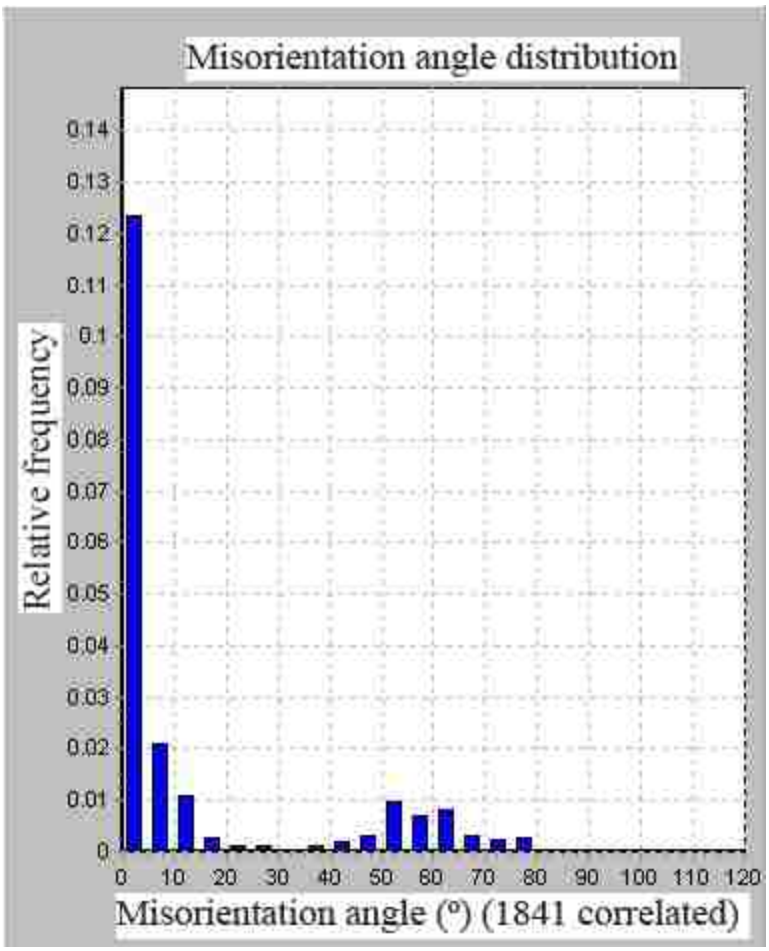

Figure 3.51. Misorientation distribution for correlated data points in grain K7.

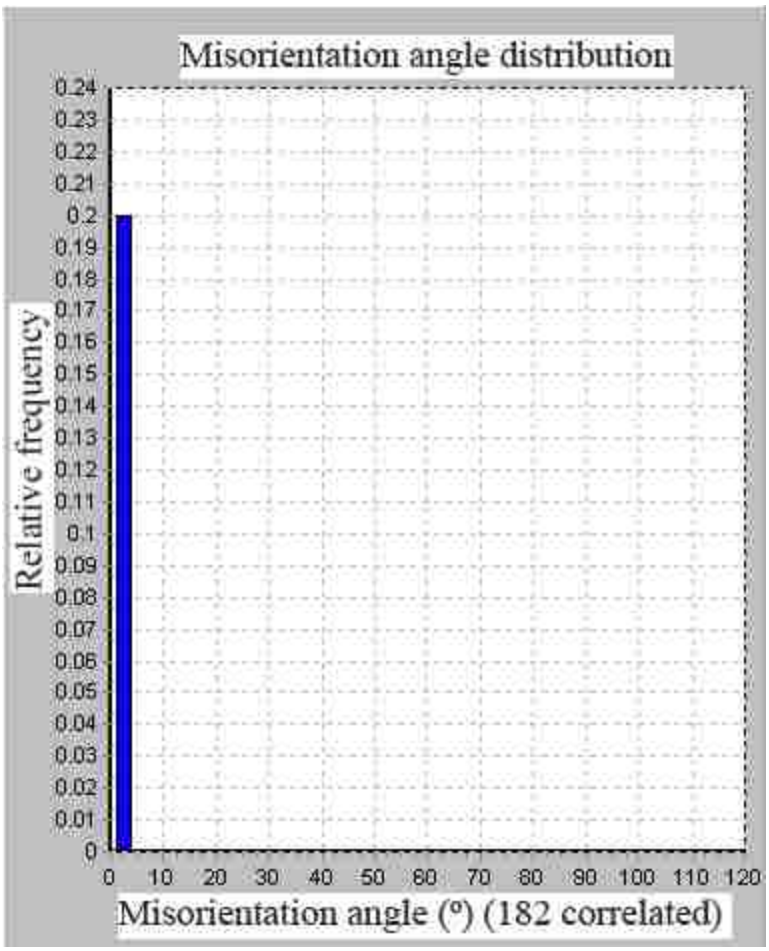

Figure 3.52. Misorientation distribution for correlated data points from control grain G1.

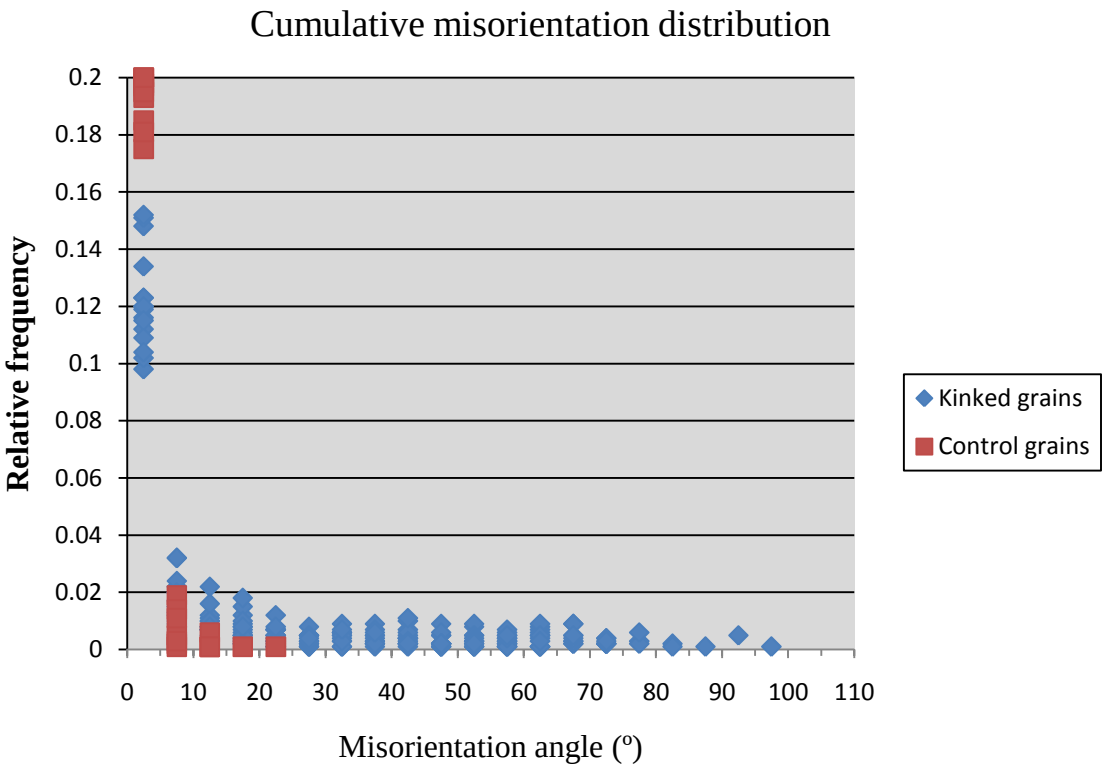

Figure 3.53. Misorientation distribution made from data points collected for all kinked grains and control grains from all of the orientation maps.

Misorientation transect data for kinked grains

The misorientation transects provide a more detailed picture of the misorientation angles along the kink band boundaries. Each kinked grain has transects that are normal to the kink band boundary, which are labeled N in figures of the transects. Transects parallel to each kink band domain are also included in each data set and are labeled P. The misorientation data for each transect type is presented from left to right for normal transects. Parallel transect data is presented from top to bottom. The normal and parallel transects for the kinked grains are shown in figures 3.54-3.63. Tables 3.4-3.13 summarize the transect misorientation values along kink band boundaries for the normal transects.

The normal transects for the kinked grains have the highest misorientation angles between adjacent data points as they cross kink band boundaries. The highest misorientation angles occur along the kink band boundaries, while lower misorientation angles that are typically less than 5º occur for the adjacent data points within the domains for the normal transects. The misorientation angles between kink band domains vary laterally across the kinked grains for the normal transects. For example, in grain K2, the misorientation angle between domains varies from 43º to 65º in transect N1. There is also variability along the same kink band domain boundary from one transect to the next for most kink band boundaries. In some cases there is a trend in the change in the misorientation along the same kink band boundary. For example, the misorientation angle decreases along the kink band domain boundary A1B1 in grain K3 from 30º to 51º for the three normal transects. The average misorientation values for all of the normal transects at kink band boundaries are summarized in table 3.14 for each grain. A histogram is shown in figure 3.64 for the misorientations along kink band boundaries from all of the grains. There is a wide distribution in frequency for the kinked grains with a frequency of .06 or higher from 10º to 70º. The maximum frequency is in the 40º to 45º range. Misorientation profiles for normal transects in grain K5 summarize the variability along kink band boundaries (figure 3.65-figure 3.67).

Misorientation angles are lower along parallel transects than along normal transects. For misorientation profiles measured relative to adjacent data points in the parallel transects, most of the misorientation values fall below 10º. Higher misorientation angles are observed in instances where the parallel transects cross kink band boundaries and subgrain boundaries. There is less variability in the parallel transect data relative to the

normal transect data. The average misorientation values for each parallel transect are shown in table 3.15. For the transects that cross kink band boundaries, the average value is an average of the misorientation angles taken from each domain separately. The average misorientation values are low with a maximum of 3º. Figure 3.68 and figure 3.69 show some of the variation in misorientation along parallel transects for grain K5.

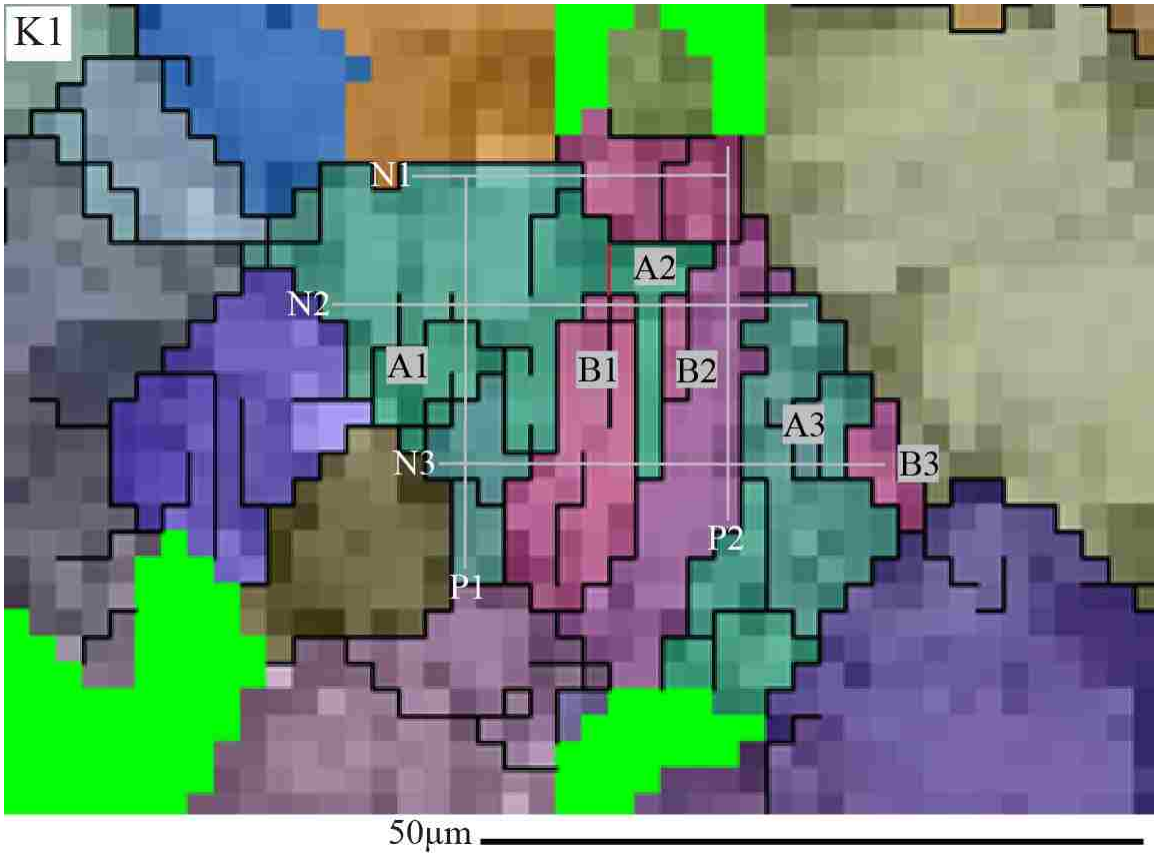

Figure 3.54. Misorientation transects for grain K1 that are normal (N) and parallel (P) to the kink band domains.

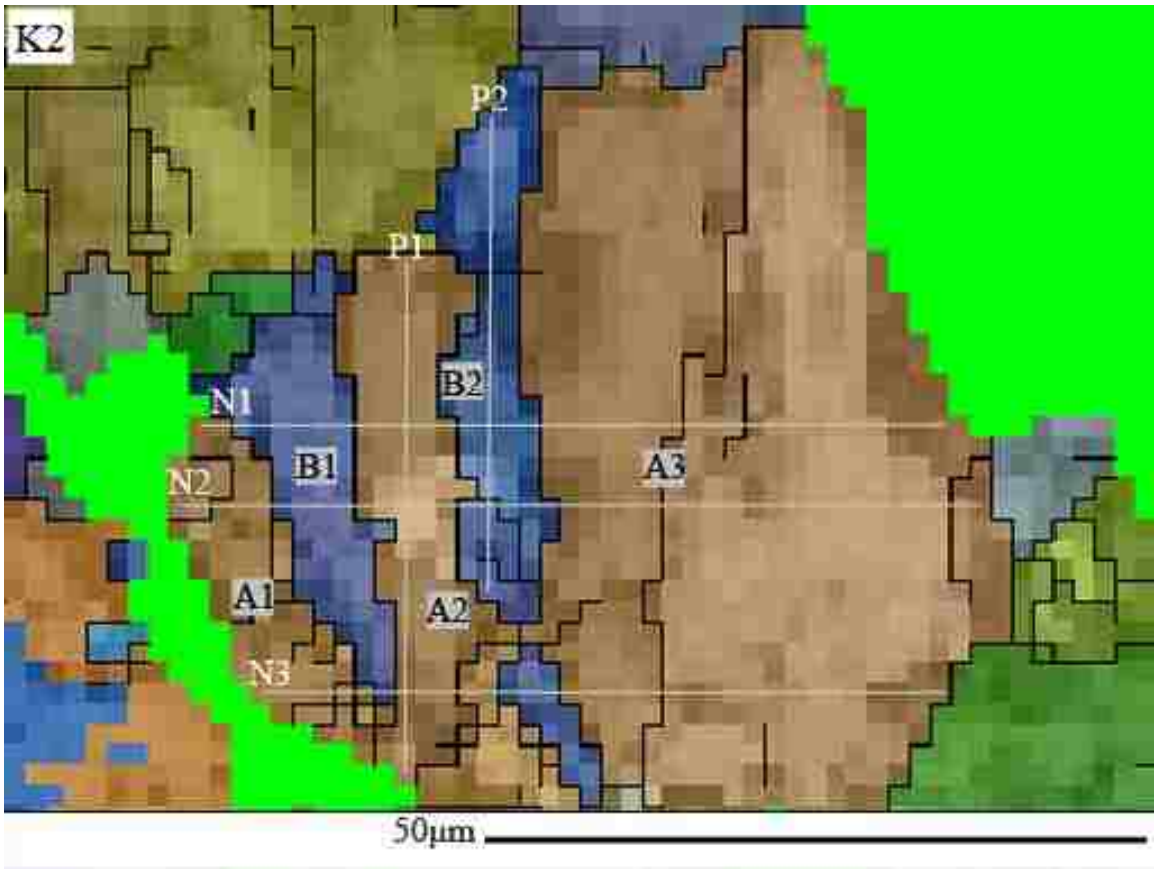

Figure 3.55. Misorientation transects for grain K2 that are normal (N) and parallel (P) to the kink band domains.

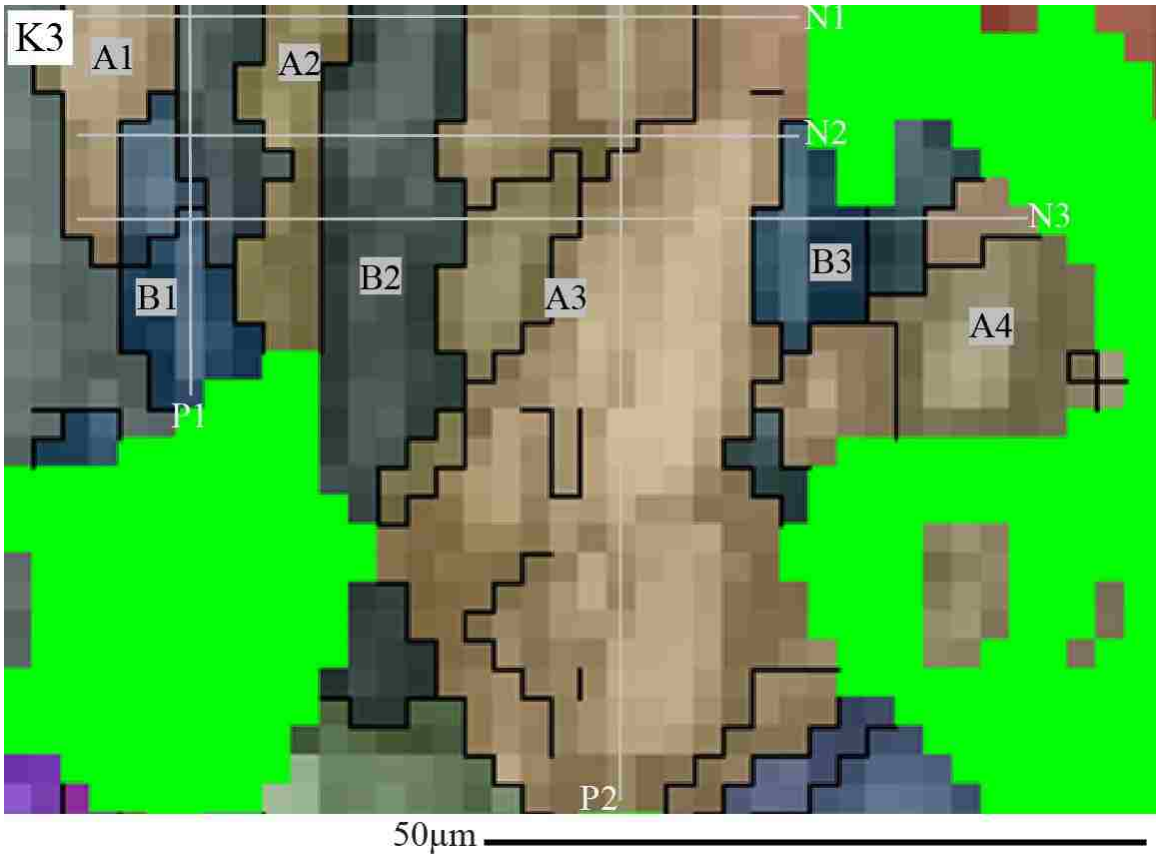

Figure 3.56. Misorientation transects for grain K3 that are normal (N) and parallel (P) to the kink band domains.

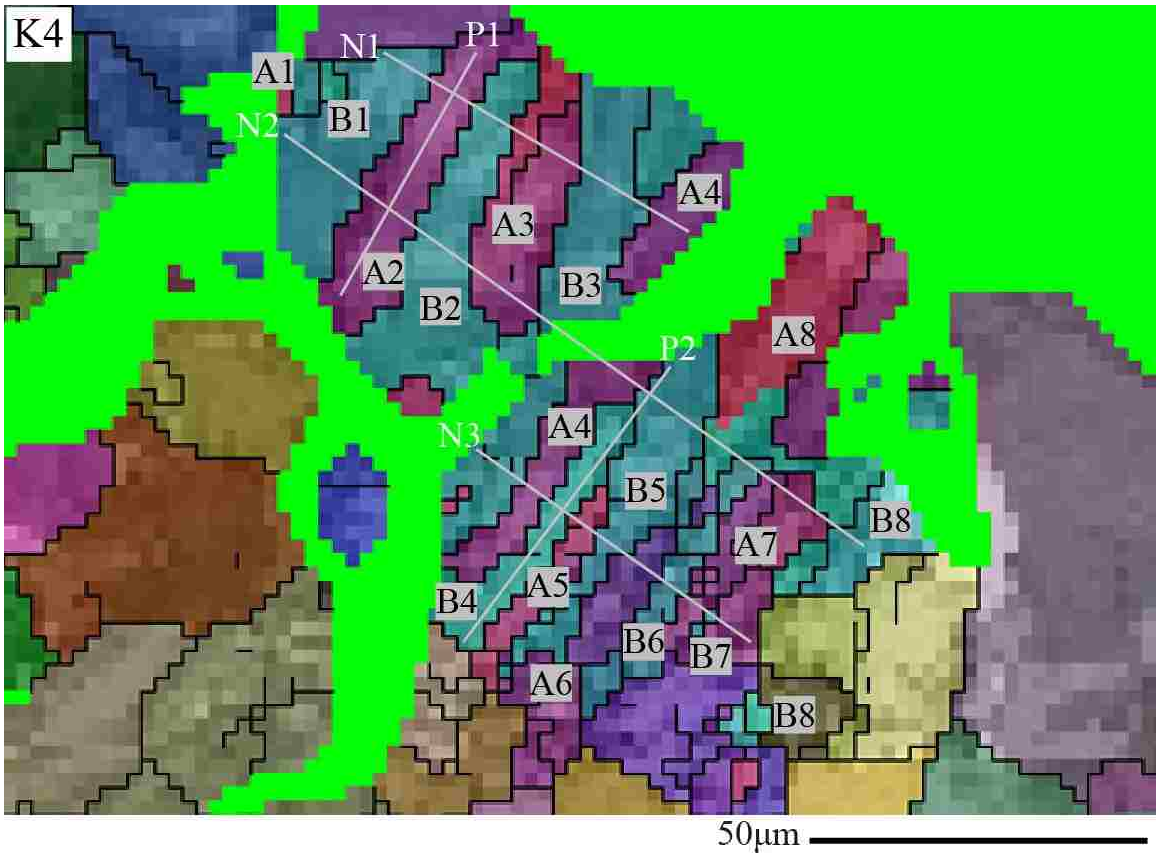

Figure 3.57. Misorientation transects for grain K4 that are normal (N) and parallel (P) to the kink band domains.

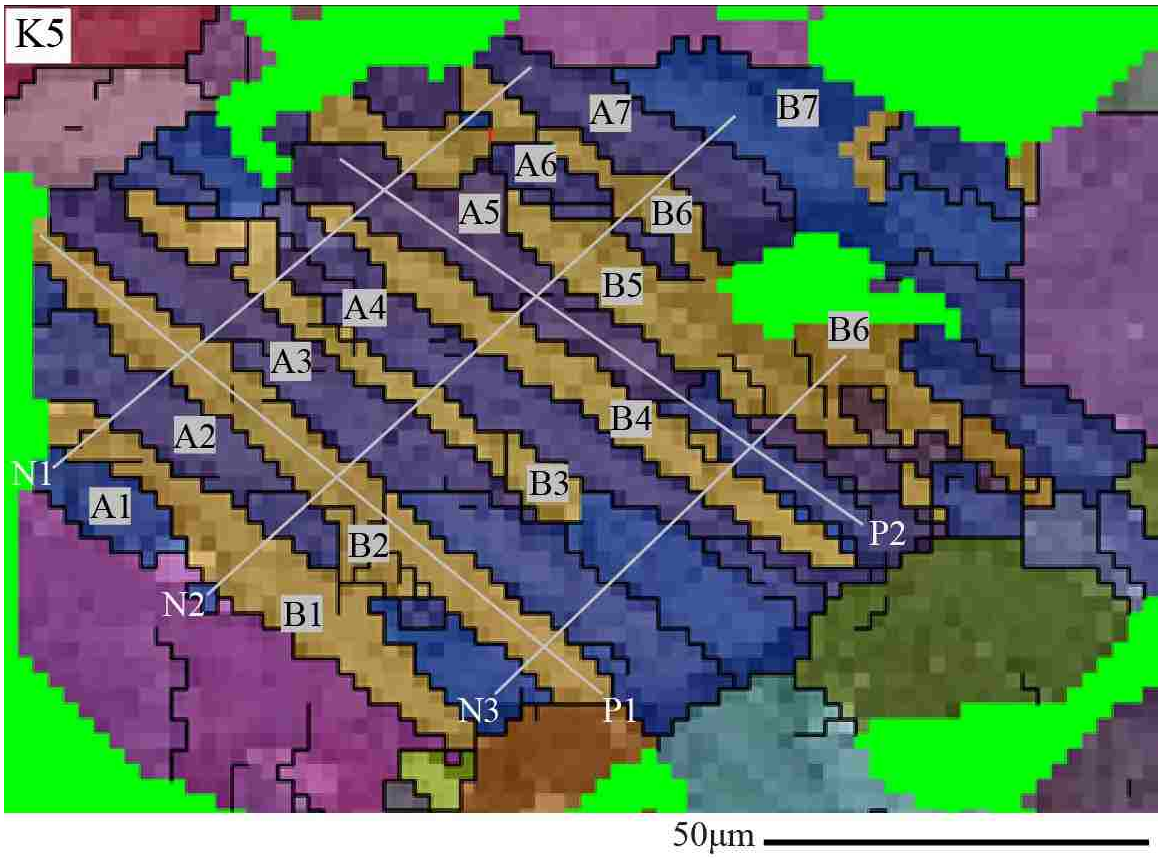

Figure 3.58. Misorientation transects for grain K5 that are normal (N) and parallel (P) to the kink band domains.

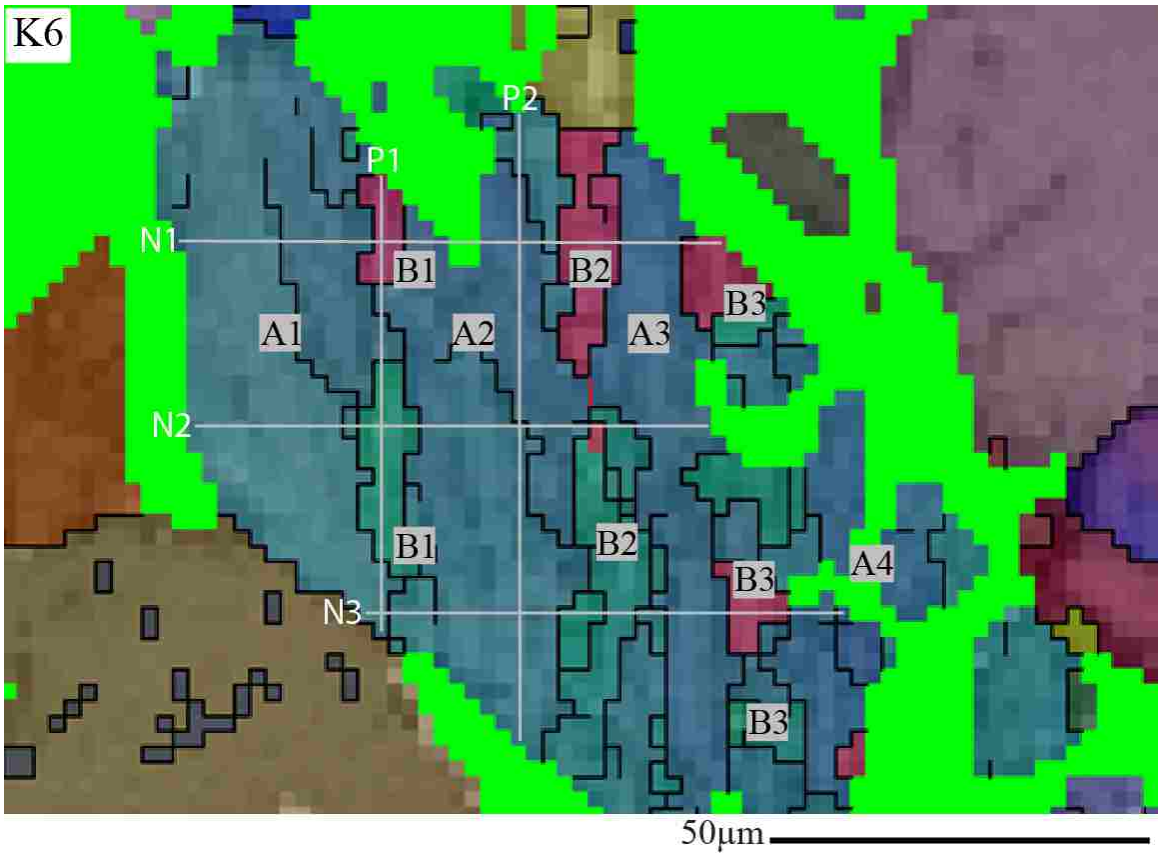

Figure 3.59. Misorientation transects for grain K6 that are normal (N) and parallel (P) to the kink band domains.

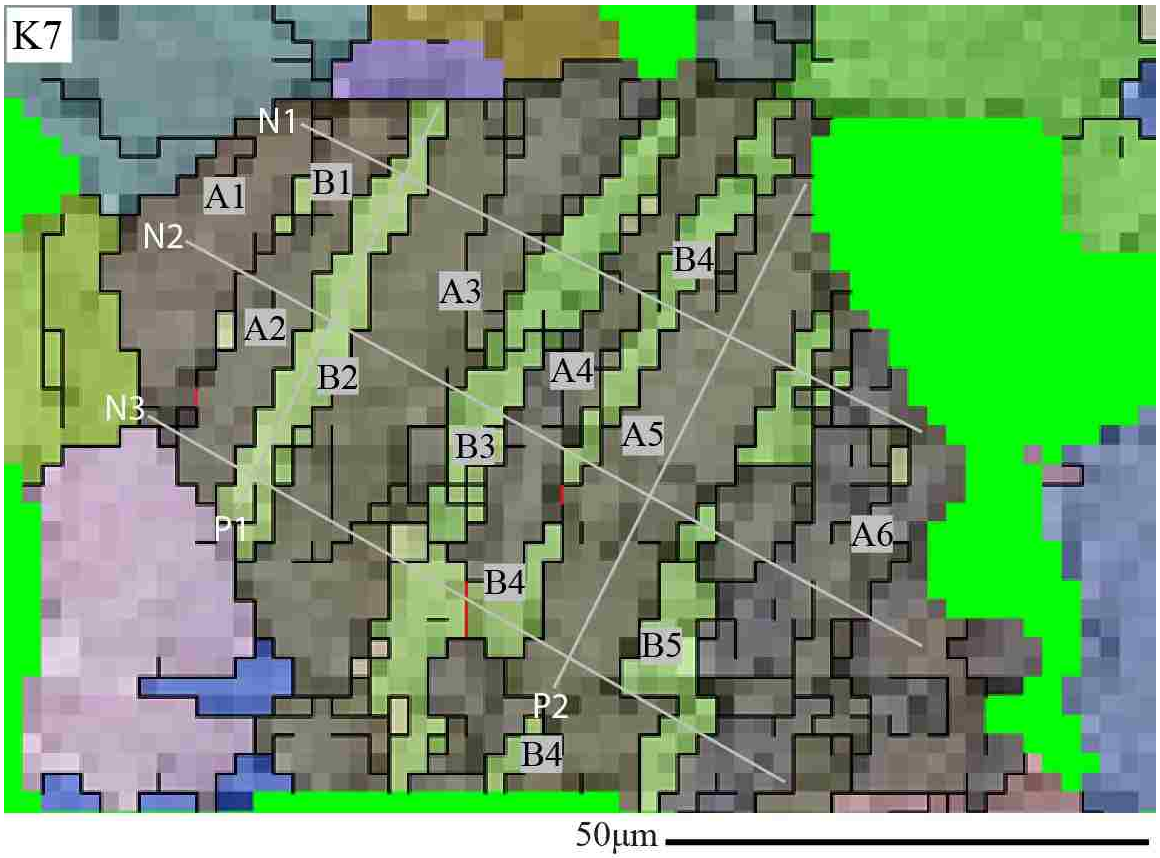

Figure 3.60. Misorientation transects for grain K7 that are normal (N) and parallel (P) to the kink band domains.

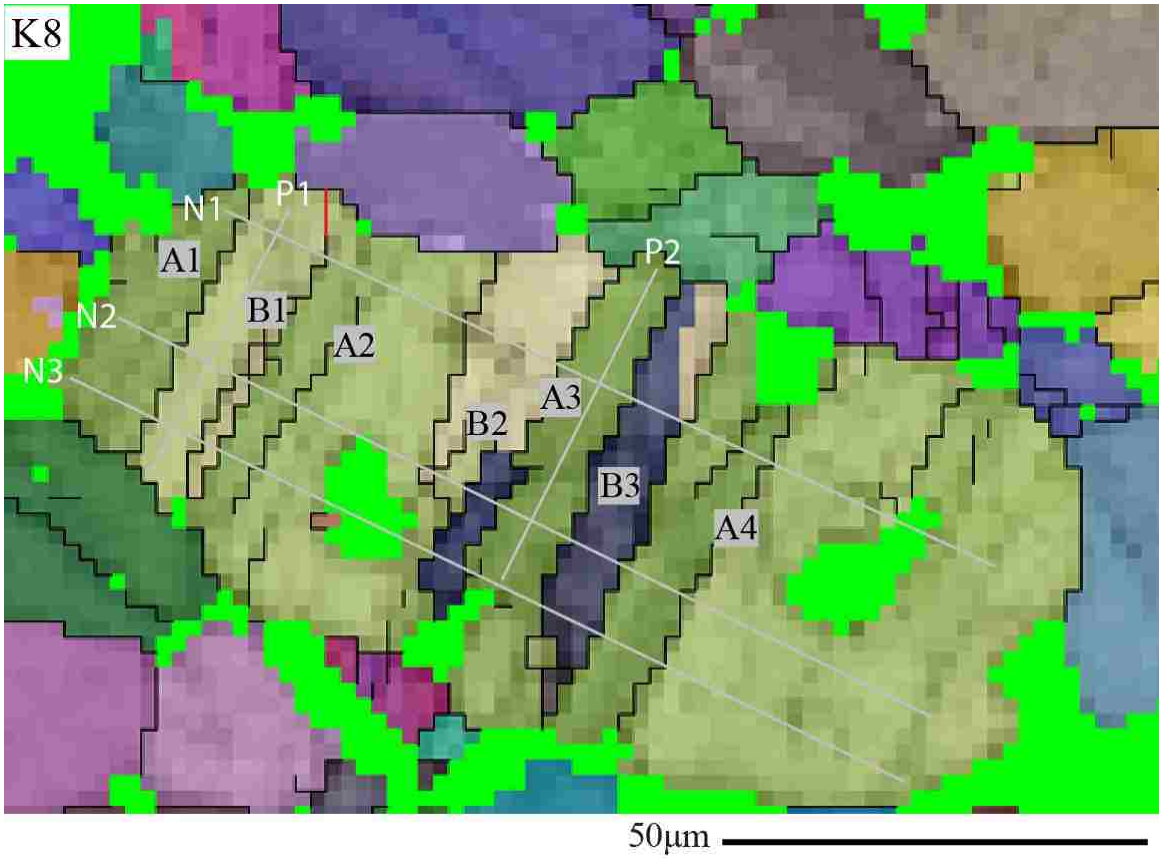

Figure 3.61. Misorientation transects for grain K8 that are normal (N) and parallel (P) to the kink band domains.

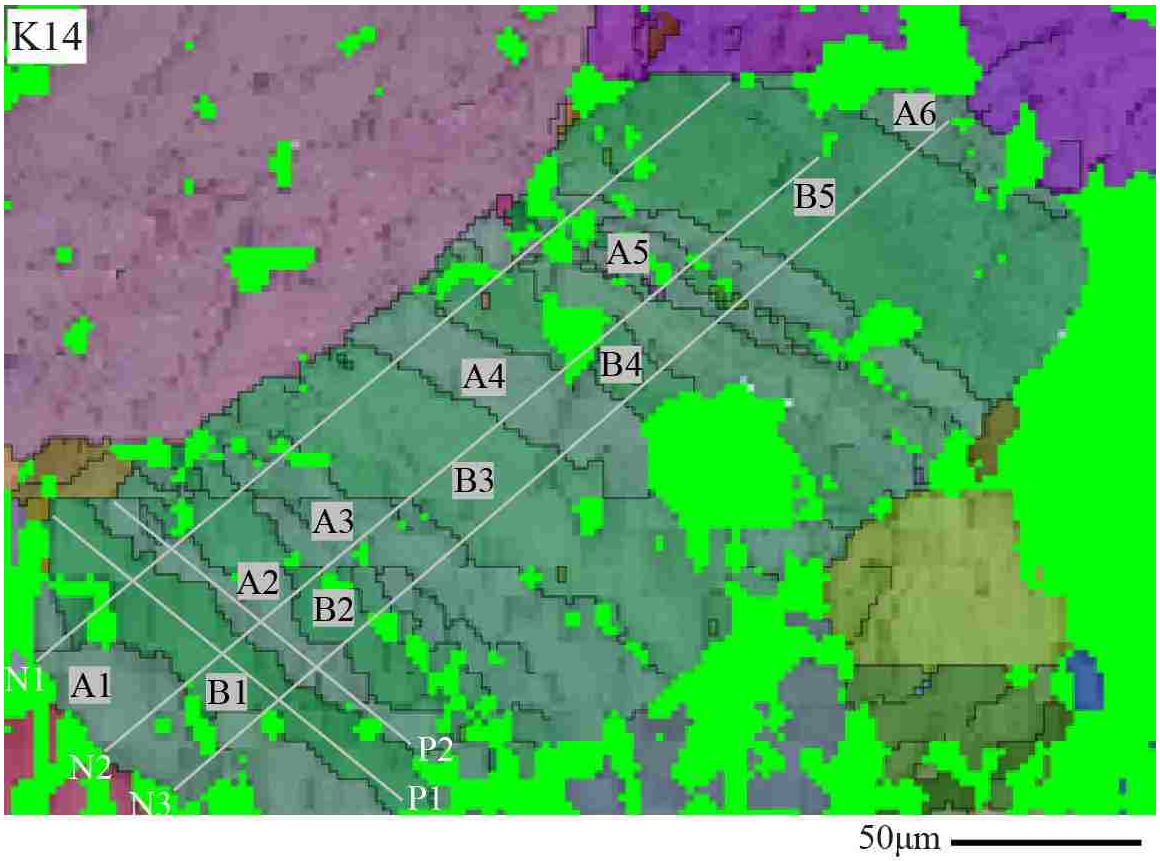

Figure 3.62. Misorientation transects for grain K14 that are normal (N) and parallel (P) to the kink band domains.

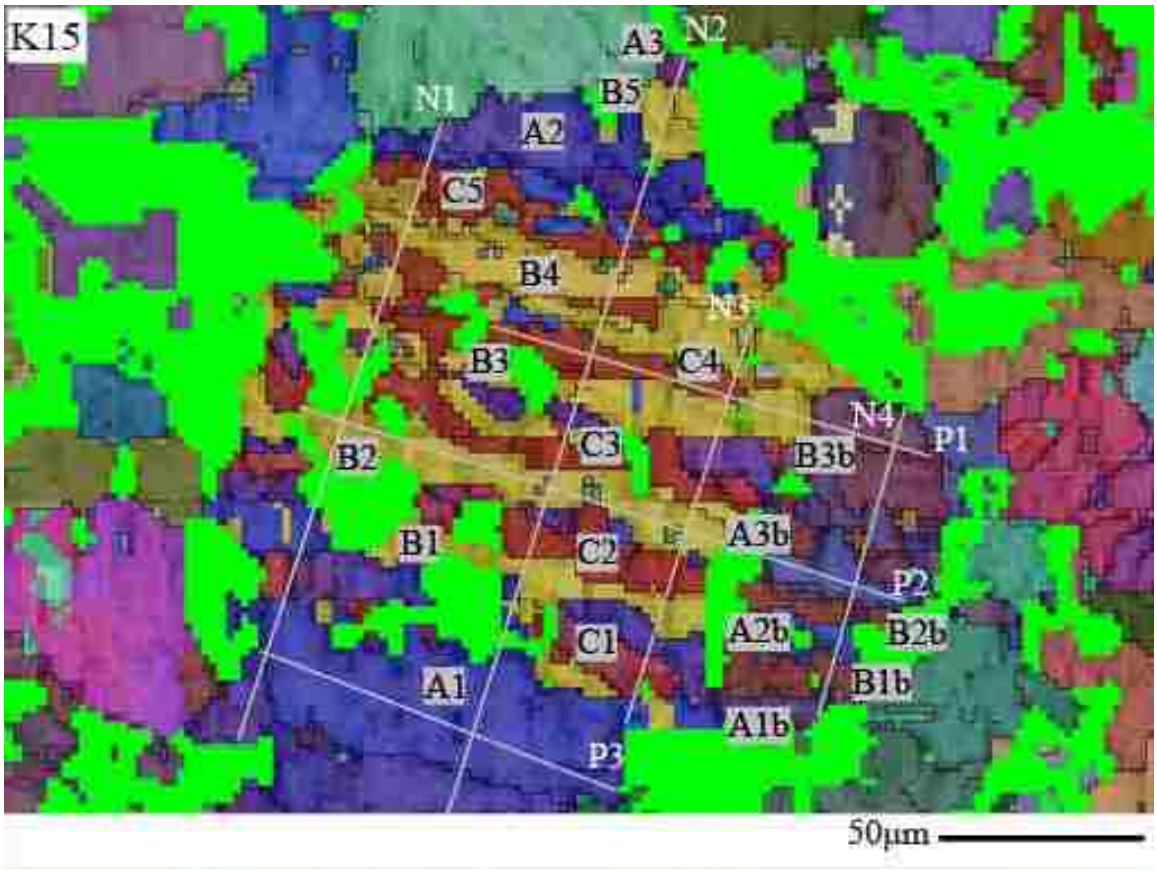

Figure 3.63. Misorientation transects for grain K15 that are normal (N) and parallel (P) to the kink band domains.

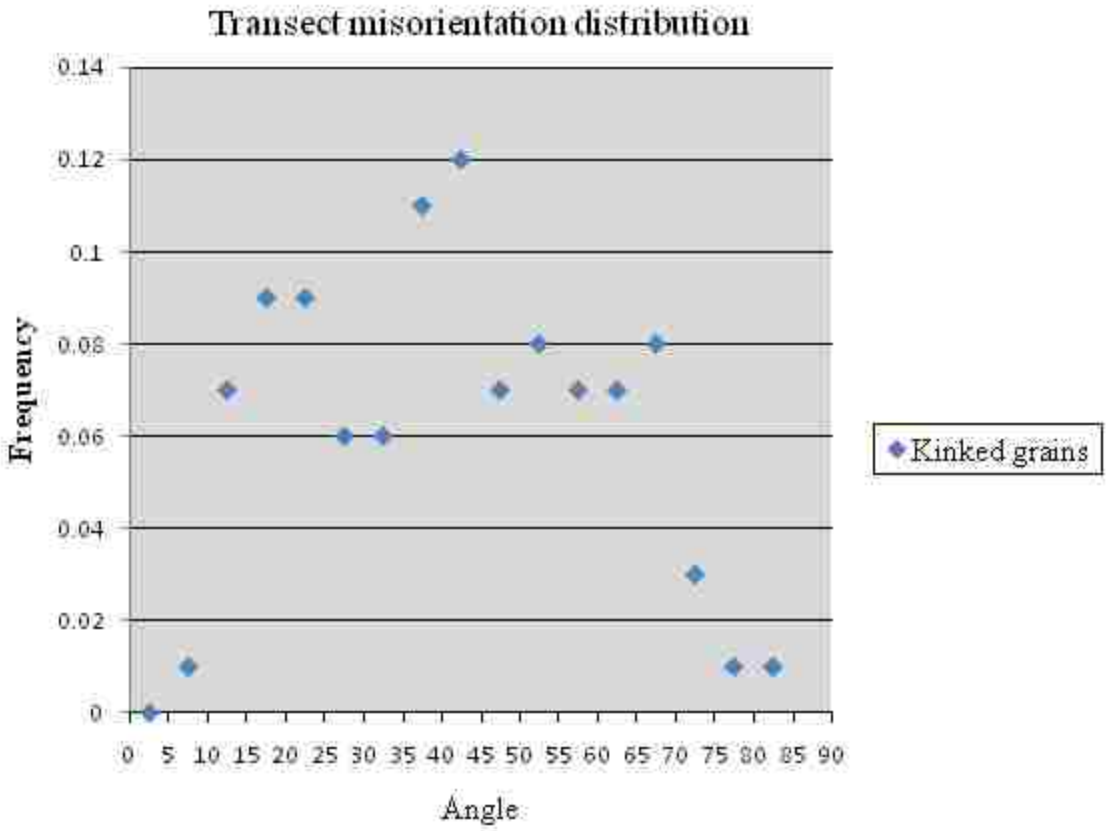

Figure 3.64. Transect misorientations along kink band boundaries.

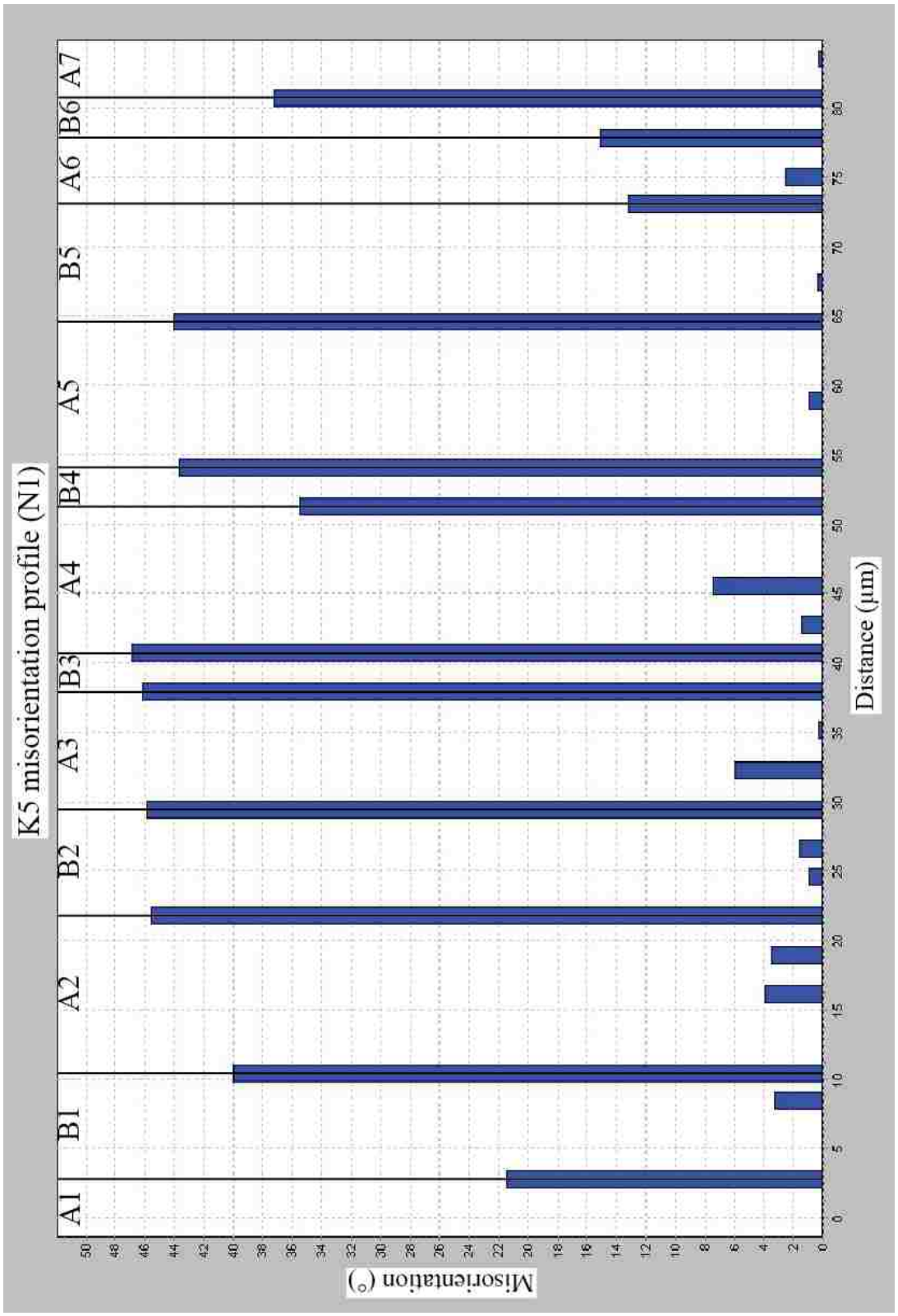

Figure 3.65. Misorientation profile for transect N1 in grain K5.

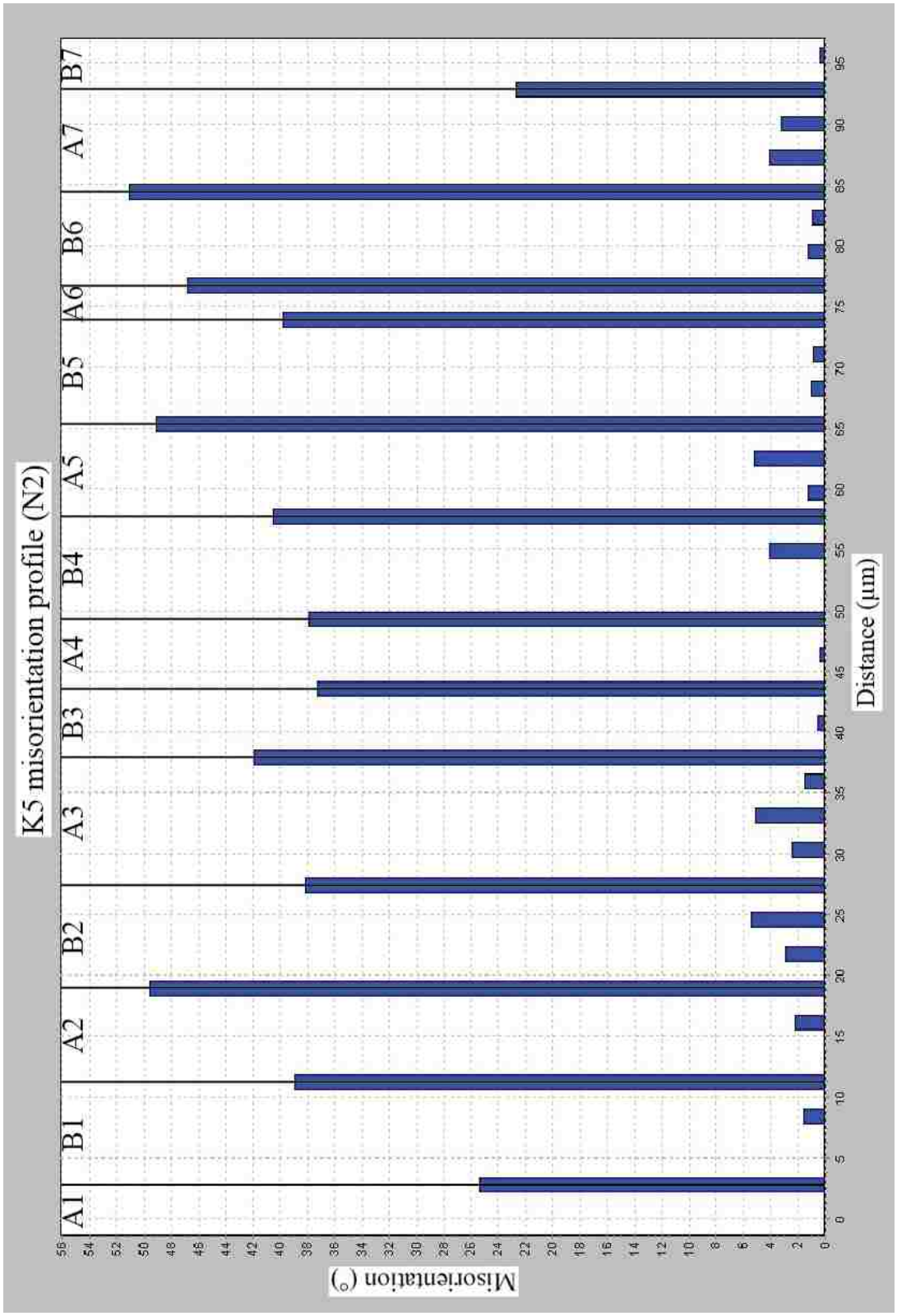

Figure 3.66. Misorientation profile for transect N2 in grain K5.

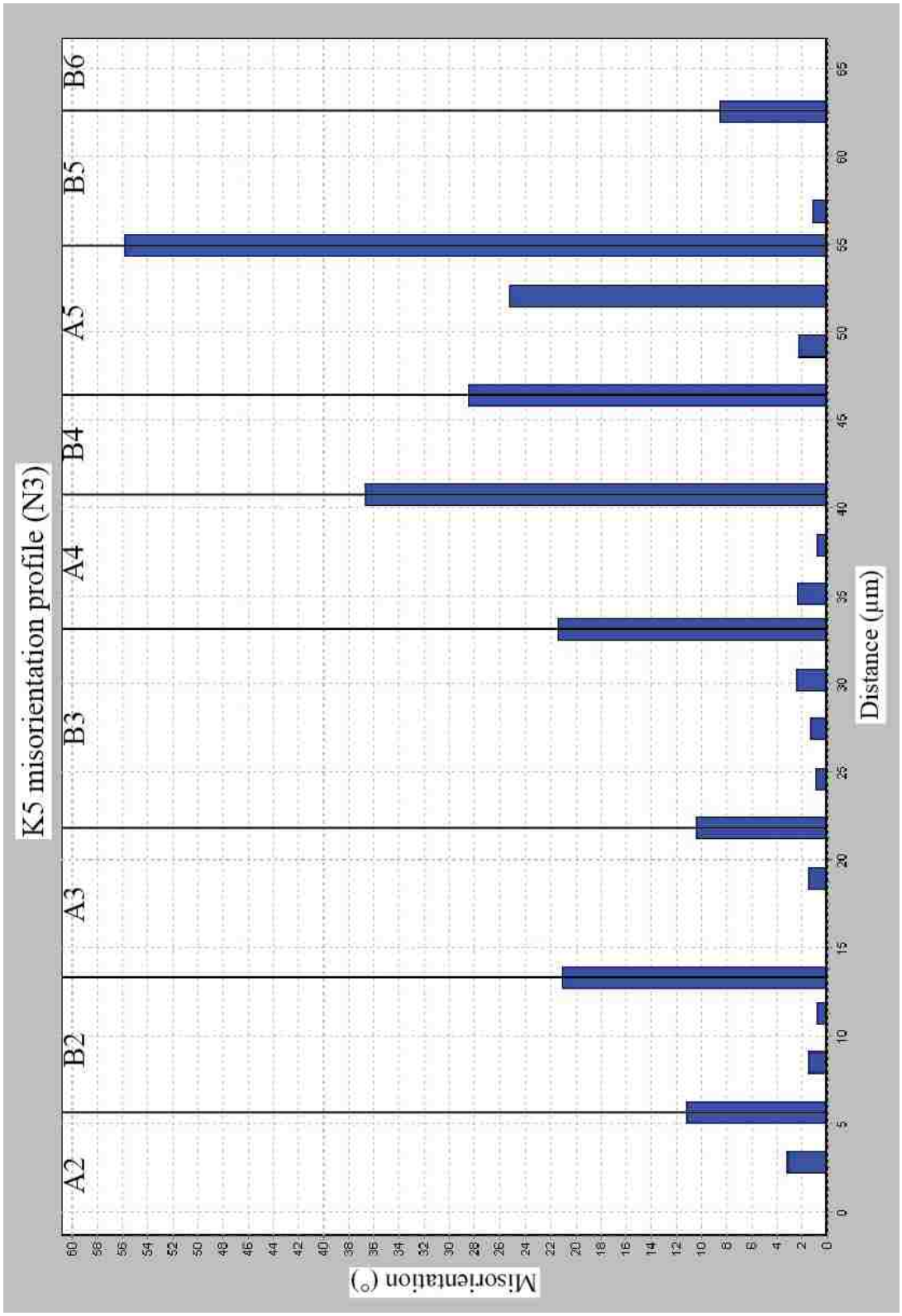

Figure 3.67. Misorientation profile for transect N3 in grain K5.

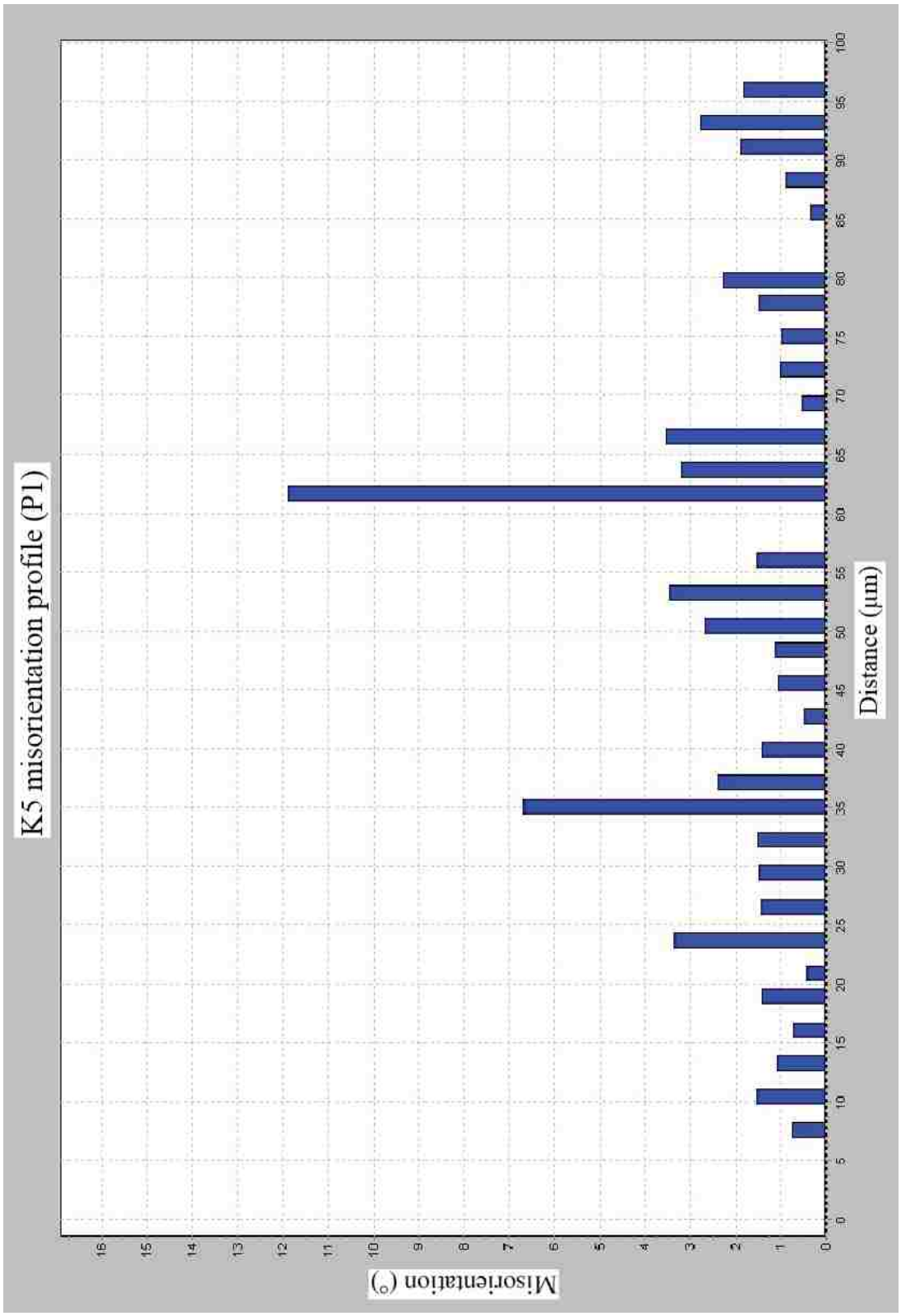

Figure 3.68. Misorientation profile for transect P1 in grain K5.

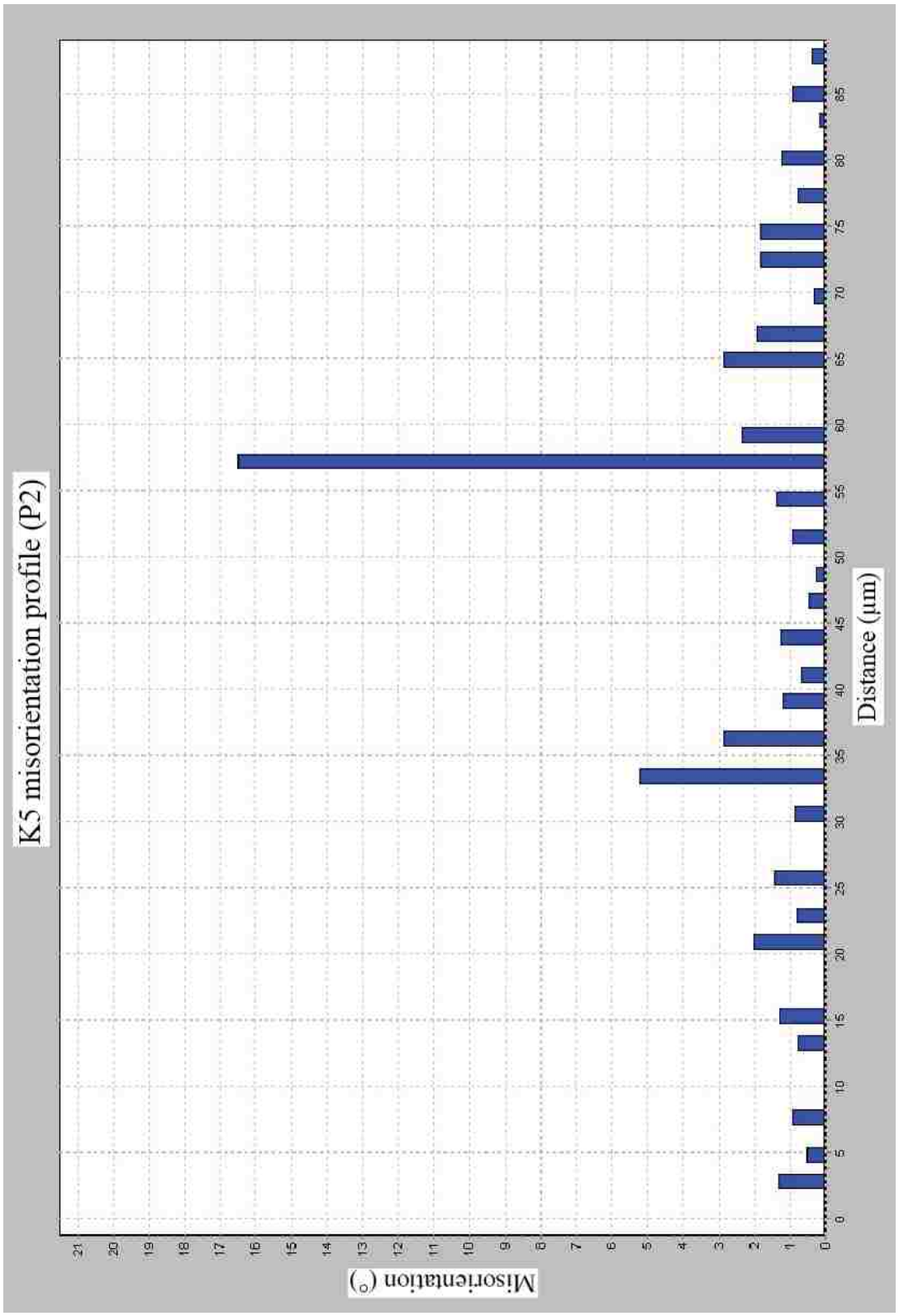

Figure 3.69. Misorientation profile for transect P2 in grain K5.

Table 3.4. Grain K1 misorientation angles at kink band boundaries (°)

TranK1	A1B1	A1B2	A2B1	A2B2	A3B2	A3B3
N1	...	38.23	.....	...	...	...
N2	33	...	...	25.07	68.27	...
N3	52.81	...	12.69	40.68	71.45	41.51

Table 3.5. Grain K2 misorientation angles at kink band boundaries (°)

TranK2	A1B1	A2B1	A2B2	A3B2
N1	51.31	65.22	50.62	42.76
N2	57.13	65.56	60.11	42.17
N3	41.17	57.7	50.32	54.15

Table 3.6. Grain K3 misorientation angles at kink band boundaries (°)

TranK3	A1B1	A2B1	A2B2	A3B2	A3B3	A4B3
N1	51.12	61.27	66.6	62.76	...	...
N2	32.01	59.37	66.55	61.13	14.18	...
N3	29.58	59.401	68.13	66.38	15.55	35.89

Table 3.7. Grain K4 misorientation angles at kink band boundaries (°)

TranK4	A2B1	A2B2	A3B2	A3B3	A4B3	A4B4	A4B5	A5B4	A5B5	A6B5	A6B6	A7B6	A7B7
N1	50.3	36.11	24.67	43.57	51.4	...	...	...	...	...	...	...	...
N2	49.89	44.73	33.96	49.94	...	...	42.5	...	...	...	...	...	...
N3	...	...	...	...	50.33	34.58	...	14.02	44.45	78.44	84.77	61.07	42.35

Table 3.8. Grain K5 misorientation angles at kink band boundaries (°)

TranK5	A1B1	A2B1	A2B2	A3B2	A3B3	A4B3	A4B4	A5B4	A5B5	A6B5	A6B6	A7B6	A7B7
N1	21.47	39.95	45.58	45.85	46.16	46.86	35.5	43.68	43.97	13.27	15.12	37.30	...
N2	25.34	38.96	49.58	38.21	41.93	37.24	37.97	40.5	49.04	39.76	46.77	51.11	22.69
N3	...	...	11.17	21.08	10.44	21.39	36.76	28.51	55.85	...	...	...	...

Table 3.9. Grain K6 misorientation angles at kink band boundaries (°)

TranK6	A1B1	A2B1	A2B2	A3B2	A3B3
N1	57.91	67.62	44.92	65.9	63.67
N2	39.26	39.38	47.51	40.39	...
N3	10.53	6.14	33.72	29.03	54.55

Table 3.10. Grain K7 misorientation angles at kink band boundaries (°)

TranK7	A2B2	A3B2	A3B3	A4B3	A4B4	A5B4	A5B5	A6B5
N1	54.8	61.27	67.09	73.57	67.32	62.31	66.93	...
N2	53.64	59.7	75.79	59.32	53.05	57.47	59.7	53.94
N3	38.84	50.53	47.01	...	...	64.76	56.09	49.33

Table 3.11. Grain K8 misorientation angles at kink band boundaries (°)

TranK8	A1B1	A2B1	A2B2	A3B2	A3B3	A4B3
N1	19.3	7.14	13.74	35.95	40.33	28.85
N2	13.66	24.22	17.68	39.76	45.73	37.85
N3	10.31	22.42	19.72	39.41	41.32	40.02

Table 3.12. Grain K14 misorientation angles at kink band boundaries (°)

TranK14	A1B1	A2B1	A2B2	A3B2	A3B3	A4B3	A4B4	A5B4	A5B5	A6B5
N1	32.51	30.75	21.4	17.66	7.62	18.69	14.54	35.5	18.58	...
N2	36.1	31.72	28.14	28.5	16.33	17.72	23	16.47	16.29	...
N3	30.5	32.8	33.68	11	16.72	20.62	29.55	11.87	20	16.75

Table 3.13. Grain K15 misorientation angles at kink band boundaries (°)

TranK15	A1B1	A1C1	B1C1	B1C2	B2C2	B2C3	B3C3	B3C4	B4C4	B4C5	A2C5	A2B5	A3B5
N1	...	23.77	20.92	...	...	16.73	35.63	62.36	69.08	73.02	45.81	...	...
N2	15.08	...	...	41.85	30.66	58.26	29.01	49.63	68.16	63.73	45.61	...	27.33
	A1C1	B1C1	B1C2	B2C2	B2C3	B3C3	B3C4	B4C4	...	...	...	...	...
N3	16.94	19.55	49.76	56.78	42.66	28.3	61.66	65.54	...	...	...	...	...
K15b	A1bB1b	A2bB1b	A2bB2b	A3bB2b	A3bB2b	...	...	...	...	...	...	...	...
N4	38.73	61.53	73.09	29.44	73.3	...	...	...	...	...	...	...	...

Table 3.14. Average transect values at kink band boundaries (º)

Grain	All transects
K1	40.56
K2	53.19
K3	49.99
K4	46.50
K5	35.59
K6	45.71
K7	58.69
K8	27.63
K14	22.68
K15	47.16
K15b	55.21

Table 3.15. Average parallel transect values for kinked grains (º)

Grain	Transect P1	Transect P2	Transect P3
K1	2.89 (A1)	1.93 (B2)	...
K2	0.84 (A2)	1.58 (B2)	...
K3	2.32(B1)	0.87 (A3)	...
K4	0.89(A2)	1.81 (B4)	...
K5	1.77(B2)	1.58 (A5)	...
K6	0.88 (C1) 0.73 (B1)	1.61 (A2)	...
K7	1.16 (B2)	1.77 (A5)	...
K8	1.06 (B1)	0.66 (A3)	...
K14	0.82 (B1)	1.35 (A2)	...
K15	1.06 (C4)	0.83 (B2)	...
K15b	1.39 (B3b)	1.24 (A3b)	0.88 (A1)

CHAPTER 4

DISCUSSION

The orientation map data, in relation to pole figure data, is particularly useful in comparing the orientation of the domains together to gain insight on the mechanisms that formed the kink bands in the kinked Mg_2GeO_4 olivine grains. Optical images provide additional support for the validity of the orientation data. The kinked grains typically have two prominent domains with distinct Euler orientations that plot in two clusters in pole figures. Crystallographic data indicates that the slip system during kink band formation was (100) [001]. Pole figures that have data clusters from the kink band domains fit a great circle for poles to all lattice planes except (010), because [010] is the rotation axis for the kinks. Kink band angle data indicates that there is a range of rotation angles. The misorientation transects show that there is a limited amount of curvature in kink bands normal to kink band boundaries and parallel to kink bands. The axial planes for the kink bands are steeply inclined to the compression direction.

The kink angle data from the contour maps and the misorientation transects shows that there is a wide range of kink angles from 19º to 68º. Table 4.1 shows a summary of the contoured pole figure measurements and average misorientation angle measurements for the opposite orientations of the two prominent kink band domains in each grain. Most of the grains have a kink angle between 15º and 50º for their conjugate orientations. No grains show kink angles lower than 15º degrees between conjugate orientations and four grains have angles greater than 50º. Histogram data also shows a wide range of kink angles (figure 3.64). The kink angles observed in this study are higher than observed by

Table 4.1. Contour and misorientation measurements of kink angle

Grain	Contour (100)	Misorientation Avg.
K1	37.61	40.56
K2	46.66	53.19
K3	46.32	49.99
K4	47.62	46.50
K5	41.55	35.59
K6	47.13	45.71
K7	54.04	58.69
K8	18.79	27.63
K9	51.13	...
K10	28.20	...
K11	41.10	...
K12	68.20	...
K13	26.04	...
K14	21.36	22.68
K15	46.16	47.16

Ave Lallemont (1985). Ave Lallemont (1985) reported average kink angles up to 45º, but observed a lower frequency of kink angles above 15º.

The kinked grains have well defined kink band domains with conjugate orientations that show some curvature and have limited preservation of the original orientation in most cases, which is in agreement with the model proposed by Barsoum (1999). Barsoum (1999) predicts the development of conjugate orientations as a result of the merger of dislocation walls from two conjugate orientations that are separated by the original orientation (figure 1.6). Grain K5 and K7 also have delamination cracks, which are predicted to form when two kink band boundaries merge together and the dislocation

density is too high. The conjugate orientations of these grains occur in the parts of the grains with the most well developed kink bands, particularly, in the central portion of the grains. Grains with higher kink angles do not preserve the original orientation including grain K7 and grain K12.

The grains that have sub-domains with intermediate orientations are inferred to show orientations with little or no rotation from the original orientation. Grain K15 is inferred to have some of the original orientation preserved. Figure 4.1 summarizes the relationship between (100) poles for grain K15 (figure 4.1a) and the relative orientation of its lattice planes with respect to each other (figure 4.1b). Domain B and Domain C have conjugate orientations in grain K15. In grain K15, the intermediate orientation (A) is found on the outer edges of each grain implying that the original orientation was preserved. The angular spread within each domain (figure 4.1a) is a reflection of the variability in the orientation of kink band domains within a grain as shown from the misorientation angles at kink band boundaries in the transects normal to the kink band boundaries. Contoured pole figures show that the highest density of data points for each domain lie in the central part of the data clusters (figure 3.45). The data points that do plot in intermediate regions between the highest densities for each domain represent the cutoff point between Euler angle orientation color in areas where data points from two different domains plot adjacent to each other. Grain K5 and grain K6 also contain intermediate orientations. Each of these grains show a decrease in the misorientation angle in the normal transects from N1 to N3, thus it is inferred that from N1 to N3, each conjugate orientation is rotated less from the original orientation of the grain. According to the kink band model proposed by Barsoum (1999), conjugate orientations in kink bands are formed by the

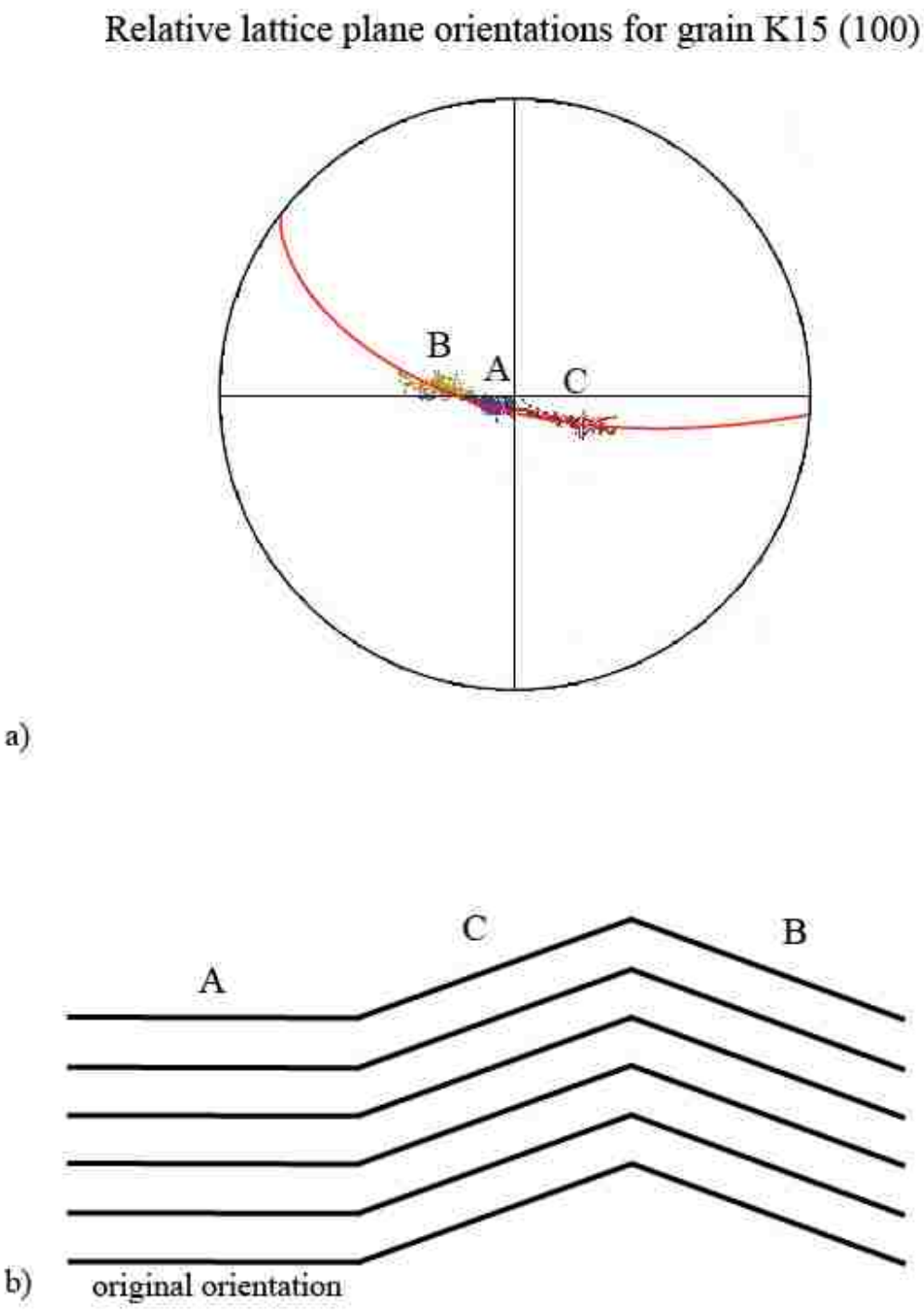

Figure 4.1. Relative orientations. a) Grain K15 orientations in upper hemisphere stereographic projection; b) relative lattice plane orientations for domains.

separation of dislocations of the opposite sign where there is an elastic buckle in the glide plane caused by a local maximum in the stress. A higher differential stress in the elastically buckled glide plane could have increased the rate of dislocation separation, leading to more stacking and higher misorientations in the upper part of grain K5 and grain K6. Grain K8 shows a blue sub-orientation in domain B2 and B3 that was not correlated optically (figure 3-17). In the (001) pole figure of K8B, there is some curvature away from the plane that each of its conjugate domains plot on (figure 3.17). Grains K4, K6, and K14 also have data points that show a significant angular spread in (001) up to 20º normal to the plane that passes through them (figure 3.13b, figure 3.15b, figure 3.23b). This implies that there is twisting of the (001) lattice, which contributes to the misorientation angle.

The misorientation transect data shows the variability in orientation within and between domains that can arise during deformation in kinked grains. The misorientation angle within kink band bandaries along the normal transects shows little variation, typically less than 5º, implying limited curvature across kink band domains. The limited curvature normal to the kink band domains is why the kink angle measurements made using contour misorientation measurements between the kink band domains is similar to the misorientation measurements made along kink band boundaries. The misorientation profiles of data points relative to each other show that there is some curvature and discontinuity parallel to kink band domains. The change in the misorientation angle along parallel transects is gradual (less than 5º) for the most part, however more abrupt changes do occur at subgrain boundaries. Figure 4.2 shows a cross section of grain K5 made using the misorientation angle at kink band boundaries for transect N2. Domain A1 is assumed

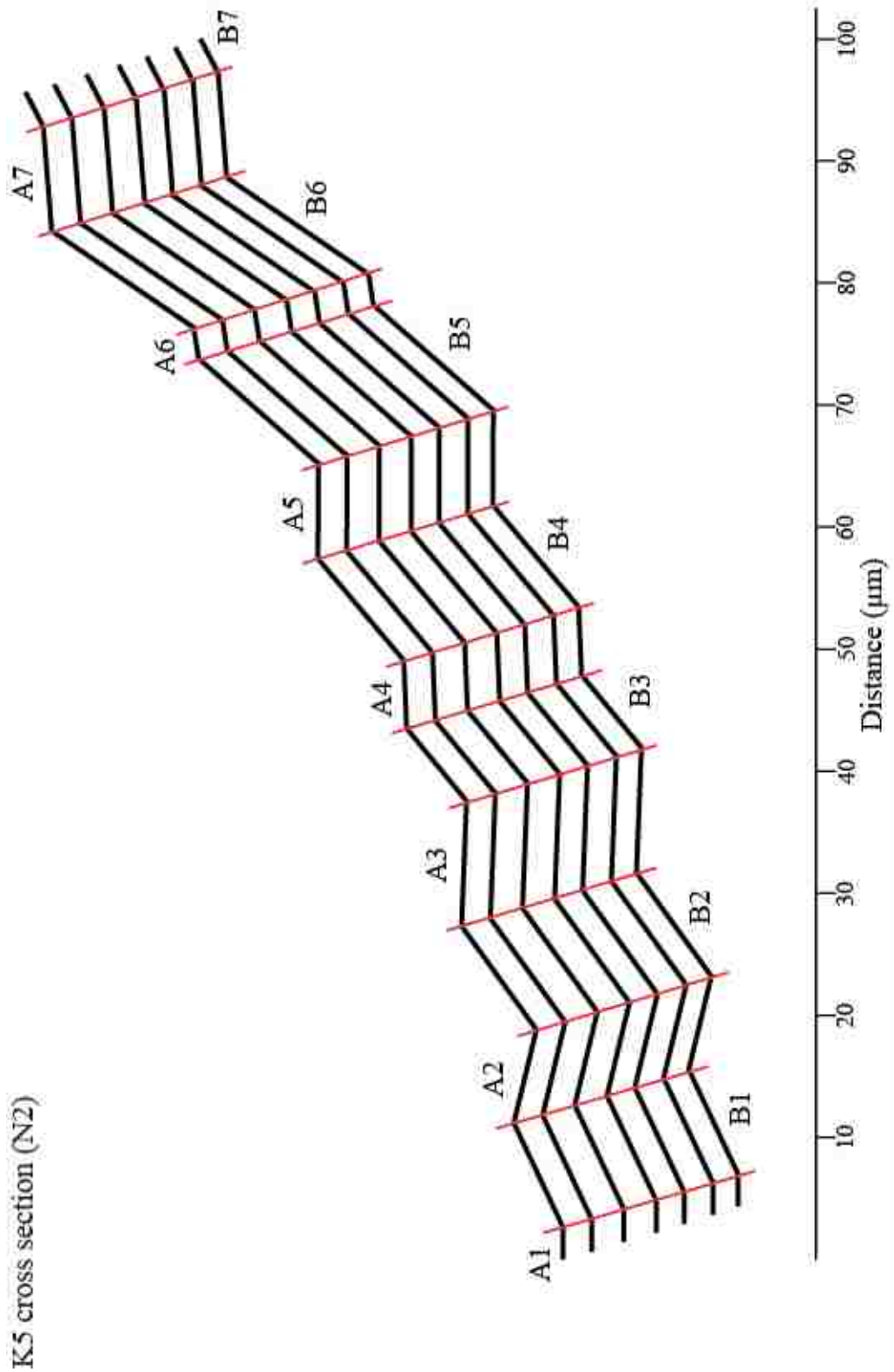

Figure 4.2. Cross section of crystal lattice for grain K5.

to have original orientation preserved in the cross section. The cross section was restored to the original orientation. An accommodation strain of 0.20 is observed in grain K5.

Kinking is in the (100) [001] slip system for the kinked grains. The orientations of the axial planes for the kinked grains are steeply inclined relative to the X0Y0 plane and contain (010) poles that are at least 42º from the compression axis. The axial planes are all oriented within 38º of the X0 axis because it is the most favorable orientation for elastic buckling to occur on. The observed slip system is consistent with the low temperature slip system for olivine (100) [001], which was expected since the kinked grains were deformed in temperatures less than 1000º C at moderate strain rates. The [001] slip direction in this study is not in agreement with the [100] slip direction reported to be the predominate slip direction for kinked Mg_2GeO_4 olivine grains by Vaughn and Coe (1978). In Vaughn and Coe (1978), the orientation measurements for the kinked grains were made using a universal stage to measure the optical indicatrix axes for each grain. Vaughn and Coe (1978) base crystallographic measurements for Mg_2GeO_4 olivine under the assumption that the relationship of the optical indicatrix with the β and γ crystallographic axes is flipped for Mg_2GeO_4 olivine in relation to natural olivine. This flip for Mg_2GeO_4 olivine is not in agreement with other crystallographic data obtained for Mg_2GeO_4 olivine in which the crystallographic axis is interpreted to be the same as olivine in relation to the indicatrix. The data in Vaughn and Coe (1978) should be interpreted with a swap of the [001] direction for [100], which would then make the slip direction observed in this study the same as in Vaughn and Coe (1978). In light of the recent data from high pressure experiments on olivine above 7.6 GPa that show that the low temperature slip systems become active at high pressures for experiments above 1000º C, the data suggests the active slip systems in Mg_2GeO_4 olivine at pressures under

2 GPa may provide a useful analogue for the deformation of olivine at high pressures found in the upper mantle. The spinel phase of Mg_2GeO_4 is already considered a useful analogue for the deformation of olivine in the mantle at higher pressures, because it is stable at ambient conditions. Figure 4.3 shows a phase diagram that shows the relative temperatures and pressures for some of the phases of AB_2O_4. The diagram shows that the Mg_2GeO_4 spinel phase is stable at lower pressures, while the Mg_2SiO_4 spinel phase (forsterite) is not at lower pressures, which is important because the forsterite phase of olivine is the most common phase of olivine in the mantle.

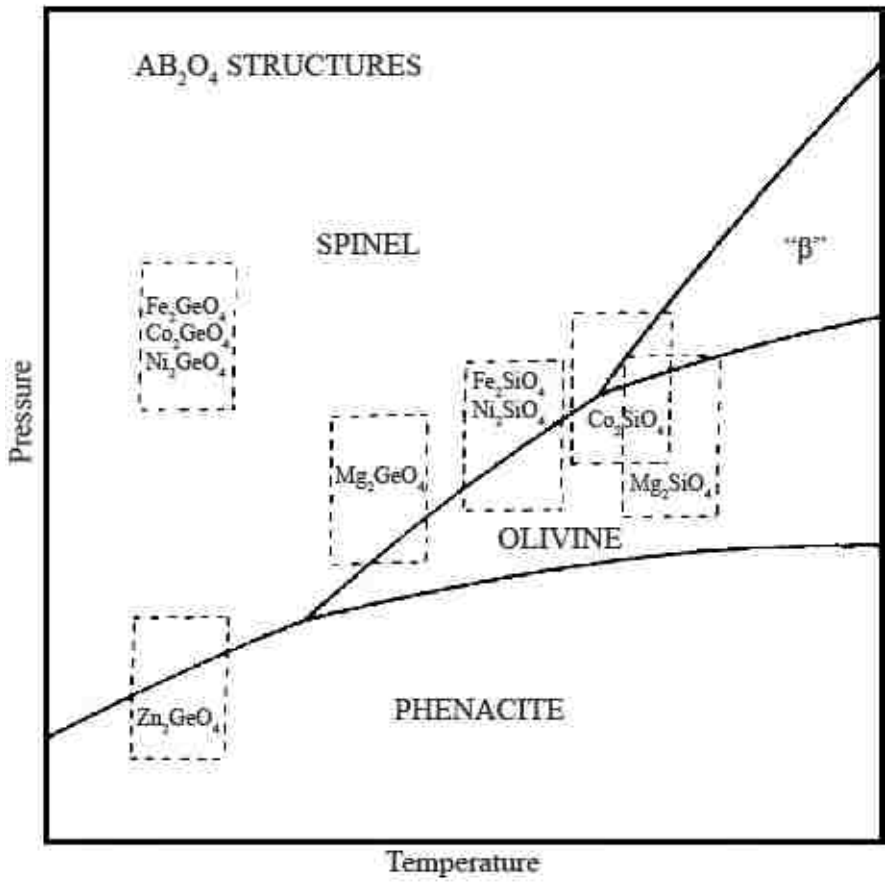

Figure 4.3. Summary of phases for AB_2O_4 structure. Diagram adapted from Navrotsky, 1989.

The formation of conjugate orientations and high kink angles suggests that kinking is an important strain accommodation mechanism in olivine. Kinking has already been recognized as an important strain hardening mechanism in metals (Wollmershauser et al, 2010.). The delamination cracks indicate that there were high dislocation densities during the formation of the kinked grains. Further research is necessary determine the distribution of kink band angles in olivine and relate active slip systems to stress and strain rates in experimental samples for different experimental conditions. A survey also needs to be conducted on xenolith samples in order to determine what percentage of natural grains become kinked in the upper mantle to assess the impact that kinking may have on the flow strength of the upper mantle.

CHAPTER 5

CONCLUSIONS

Kinked Mg_2GeO_4 olivine grains in deformed polycrystals have axial planes that are steeply inclined relative to the X0Y0 plane. There is variation in the orientation of the axial planes, but 12 of 15 grains have axial planes that plot within 30º of X0, which is perpendicular to the compression axis. Contoured pole figure measurements and average misorientation transect measurements show that there is no preferred kink angle for the grains. A range of kink angles is observed from 19º to 68º. The grains in this study have higher kink angles than previously observed in kinked olivine grains, for which most grains had kink angles of 15º or less (Ave Lallemont, 1985). While the misorientation averages and contour measurements provide a useful bulk measurement of the kink angles, each grain shows variability of the kink angle in the misorientation transects. The misorientation angle varies across kinked grains for kink band domains in transects normal to the kink band boundaries and also varies along the same kink band boundary. In grain K5 and grain K6, there is change from high angle conjugate orientations to lower angle conjugate orientations along the kink band boundaries. Misorientation transects show that there is some curvature found along transects within kink band domains parallel and normal to kink band domains. The curvature is limited and irregular, and most misorientations within kink band domains have a value of 5ºor less.

The slip system active for the kinked grains in this study is (100) [001]. The grains were deformed at moderate strain rates in temperatures less than 1000º C at pressures less than 1.5 GPa. The active slip system for the kinked grains is consistent with previous

work on olivine for low temperatures and high pressures above 7.6 GPa found in the upper mantle. Previous work on kinked Mg_2GeO_4 olivine by Vaughn and Coe (1978) indicates slip in the [100] direction, but the universal stage measurements were made with swapped γ and β values for the crystallographic directions compared to natural olivine. When the directions are corrected for, the slip direction associated with the kinked grains in Vaughn and Coe (1978) is [001] in agreement with the current results. The activation of the high pressure slip system for olivine at pressures below 2 GPa in Mg_2GeO_4 olivine suggests that Mg_2GeO_4 olivine may be a useful analogue material for olivine at conditions found in the upper mantle, which would allow research on deformation fabrics in the upper mantle to be performed on Mg_2GeO_4 olivine polycrystals at lower pressures below 2 GPa.

BIBLIOGRAPHY

Ashby, M., Verrall, R., Schloessin, H., Rutter, E., Ashbee, K., White, S., Murrell, S., and Kelly, A., 1978, Micromechanisms of flow and fracture, and their relevance to the rheology of the upper mantle: Philosophical Transactions of the Royal Society of London, v. 288, no. 1350, p. 83-87.

Ave Lallemant, H.,1985, Subgrain rotation and dynamic recrystallization of olivine, upper mantle diapirism, and extension of the Basin and Range Province: Tectonophysics, v. 119, no. 1-4, p. 98-101.

Bai, Q., and Kohlstedt, D., 1992, High temperature creep of olivine single crystals, 2. dislocation structures: Tectonophysics, v. 206, no. 1-2, p. 1-28.

Baldridge, W., 1979, Mafic and ultramafic inclusion suites from the Rio Grande Rift (New Mexico) and their bearing on the composition and thermal state of the lithosphere: Journal of Volcanology and Geothermal Research, v. 6, no. 3, p. 324.

Barsoum, M., Farber, L., and El-Raghy, T., 1999, Dislocations, kink bands, and room-temperature plasticity of Ti_3SiC_2: Metallurgical and Materials Transactions A-Physical Metallurgy and Materials Science, v. 30, no. 7, p. 1727-1737.

Billen, M., and Hirth, G., 2007, Rheologic controls on slab dynamics: Geochemistry Geophysics Geosystems, v. 8, no. 8, p. 1-5, http://www.sciencedirect.com. ezproxy. library.unlv.edu/science/article/pii/S0040195107003186.html (accessed May 13, 2011).

Bird, P., 1998, Testing hypotheses on plate-driving mechanisms with global lithosphere models including topography, thermal structure, and faults: Journal of Geophysical Research, v. 103, no. B5, p. 10115-10118.

Bjerg, E., Ntaflos, G., Kurat, G., Dobosi, G., and Labudia, C., 2005, The upper mantle beneath Patagonia, Argentina, documented by xenoliths from alkali basalts: Journal of South American Earth Sciences, v. 18, no. 2, p. 128.

Burnley, P., 1990, The effect of nonhydrostatic stress on the olivine-spinel transformation in Mg_2GeO_4 [Ph.D thesis]: Davis, University of California.

Burnley, P., Brawner, M., and Hoth G., 2008, Elastic Plastic Self Consistent (EPSC) modeling of plastic deformation in olivine. Abstract MR33G-1864: Eos Trans. AGU. v. 89, no. 53.

Burnley, P., and Zhang, D, 2008, Interpreting *in situ* x-ray diffraction data from high pressure deformation experiments using elastic-plastic self-consistent models: an example using quartz: Journal of Physics-Condensed Matter, v. 20, no. 28, p. 1-10.

Carter, N., and Ave Lallemant, H., 1970, High temperature flow of dunite and peridotite: Geological Society of America Bulletin, v. 81, no. 8, p. 2185-2188.

Chernyshov, A., 2005, Petrostructural signature of olivine in ultramafic rocks of the Paramsky and Shamanskty massifs: Russian Journal of Geology and Geophysics, v. 46, no. 11, p. 1103-1104.

Cordier, P., 2002, Dislocations and slip systems of mantle minerals, *in* Karato, S. and Wenk, H., eds., Plastic deformation in minerals and rocks, Chantilly, Mineralogical Society of America, v. 51., no. 1, p. 137-139.

Couvy, H., Frost, D., Heidelbach, F., Nyilas, K., Ungar, T., Mackwell, S. and Cordier, P., 2004, Shear deformation experiments of forsterite at 11 GPa-1400º C: European Journal of Mineralogy, v. 16, no. 6, p. 887.

Demouchy, S., Schneider, E., Mackwell, S., Zimmerman, M., and Kohlstedt, D., 2009, Experimental deformation of olivine single crystals at lithospheric temperatures: Geophysical Research Letters, v. 36, no. L04304, p. 1-5.

Dupas-Bruzek, C., Tingle, T., Green II, H., Doukhan, N., and Doukhan, J., 1998, The rheology of olivine and spinel magnesium germanate (Mg_2GeO4): TEM study of the defect microstructures: Physics and Chemistry of Minerals, v. 25, no 7, p. 508-509.

Durham, W., Weidner, D., Karato, S., and Wang, Y., 2002, New developments in deformation experiments at high pressure *in* Karato, S. and Wenk, H., eds., Plastic deformation in minerals and rocks, Chantilly, Mineralogical Society of America, v. 51, no. 1, p. 30-40.

Durinck, J., Legris, A., and Cordier, P., 2005, Pressure sensitivity of olivine slip systems: first-principle calculations of generalized stacking faults: Physics and Chemistry of Minerals, v. 32, no. 8-9, p. 646.

Heege, J., De Bresser, J., and Spiers, C., 2004, Composite flow laws for crystalline materials with log-normally distributed grain size: theory and application to olivine: Journal of Structural Geology, v. 26, no. 9, p. 1693-1694.

Hirth, Gregg, 2002, Laboratory constraints on the rheology of the upper mantle *in*, Karato, S. and Wenk, H., eds., Plastic deformation in minerals and rocks, Chantilly, Mineralogical Society of America, v. 51, no. 1, p. 99-104.

Humphreys, F., 2001, Review: grain and subgrain characterization by electron backscatter diffraction: Journal of Materials Science, v. 36, no. 16, p. 3833-3854.

Kaminski, E., and Ribi, N., 2001, A kinematic model for recrystallization and texture development in olivine polycrystals: Earth and Planetary Science Letters, v. 189, no. 3-4, p. 253-257.

Karato, S., 2009, Rheology of the deep upper mantle and its implications for the preservation of continental roots: A review: Tectonophysics, v. 481., no. 1-4, p. 6-7.

Kohlstedt, D., 2006, The role of water in high-temperature rock deformation *in* Keppler, H. and Smyth, J., eds., Water in nominally anhydrous minerals. Chantilly, Mineralogical Society of America, v. 62, p. 379.

Kopylova, M., Russell, J., and Cookenboo, H, 1999, Petrology of peridotite and pyroxenite xenoliths from Jericho Kimberlite: implications for the thermal state of the mantle beneath the Slave Craton, northern Canada: Journal of Petrology, v. 40, no. 1, p. 80.

Manga, M., 1996, Mixing of heterogeneities in the mantle: Effect of viscosity differences: Geophysical Research Letters, v. 23, no. 4, p. 403.

Mei, S., Suzuki, A., Kohlstedt, D., Dixon, N., and Durham, W., 2010, Experimental constraints on the strength of the lithospheric mantle: Journal of Geophysical Research, v. 115, no. B08204, p. 1-9.

Mercier, J., and Nicolas, A., 1975, Texture and fabrics of upper-mantle peridotites as illustrated by xenoliths from basalts: Journal of Petrology, v. 16, no. 2, p. 455-469.

Navrotsky, A., 1989, Silicates and germanates at high pressure: Solid State Ionics, v. 32-33, p. 288-290.

Nicolas, A., Boudier, F., and Boullier, A., 1973, Mechanisms of flow in naturally and experimentally deformed peridotites: American Journal of Science, v. 273, no. 10, p. 857-852.

Ochuchi, T., Kawazoe, T., Nishihara, Y., Nishiyama, N., and Irifune, T., 2011, High pressure and temperature fabric transitions in olivine and variations in upper mantle seismic anisotropy: Earth and Planetary Science Letters, v. 304, no. 1, p. 56-59.

Oxford Instruments A/S , 2007, Hkl software manual.

Randle, V., 1992, Microtexture determination and its applications: London, The Institute of Materials, p. 85.

Ratterron, P., Chen, J., Li, L., Weidner, D., and Cordier, P., 2007, Pressure-induced slip-system transition in forsterite: Single-crystal rheological properties at mantle pressure and temperature: American Mineralogist, v. 92, no. 8-9, p. 1436-1441.

Royden, L., 1993, Evolution of retreating subduction boundaries formed during continental collision: Tectonics, v. 12, no. 3, p. 629-638.

Singh, A., Balasingh, C., Mao, H., Hemley, R., Shu, J., 1998, Analysis of lattice strains measured under non-hydrostatic pressure: Journal of Applied Physics, v. 83, no. 12, p. 7567-7578.

Stewart, I., Sauber, J., and Rose, J., 2000, Glacio-siesmotectonics: ice sheets, crustal deformation, and seismicity: Quaternary Science Reviews, v. 19, no. 14-15, p. 1367-1371.

Tommasi, A., Mainprice, D., Canova, G., and Chastel, Y., 2000, Viscoplastic self-consistent and equilibrium based modeling of olivine lattice preferred orientations: implications for the upper mantle seismic anisotropy: Journal of Geophysical Research-Solid Earth, v. 105, no. B4, p. 7893.

Tullis, T, and Tullis, J.,1986, Experimental rock deformation techniques *in* Hobbs, B. and Heard, H., eds. Mineral and Rock Deformation: Laboratory Studies. Washington, D.C.: American Geophysical Union, v. 36, 324 p.

Vaughn, P., and Coe, R., 1978, Geometric flow properties of the germanate analog of forsterite: Tectonophysics, v. 46, no. 1-2, p. 187-196.

Wang, Q., 2010, A review of water contents and ductile deformation mechanisms of olivine: implications for the lithosphere-asthenosphere boundary of the continents: Lithos, v. 120, no. 1-2, p. 35-37.

Wang, Y., Liebermann, R., and Boland, J., 1988, Olivine as an *in situ* piezometer in high pressure apparatus: Physics and Chemistry of Minerals, v. 15, no. 5, p. 493-497.

Warren, J., Hirth, G., and Kelemen, P., 2008, Evolution of olivine lattice preferred orientation during simple shear in the mantle: Earth and Planetary Science Letters, v. 272, no. 3-4, p. 504.

Wells, M. and Hoisch, T., 2008, The role of mantle delamination in widespread Late Cretaceous extension and magmatism in the Cordilleran orogen, western United States, v. 120, no. 5-6, p. 515-526.

Wenk, H., 2002., Texture and anisotropy *in* Wenk, H., ed., Plastic deformation in minerals and rocks, Chantilly, Mineralogical Society of America, v. 51, no. 51, p. 303-304.

Wollmershauser, J., Neil, C., and S., Agnew, 2010, Mechanisms of ductility in CoTi and CoZr B2 Intermetallics: Metallurgical and Materials Transactions A-Physical Metallurgy and Materials Science, v. 41A, no. 5, p. 1217-1279.

Wurzner, S., Helbig, R., Funke, C., and Moller, H., The relationship between microstructure and dislocation density distribution in multicrystalline silicon: Journal of Applied Physics, v. 108, no. 8, p. 1-6.

VITA

Graduate College
University of Nevada, Las Vegas

Alex Gregory Drue

Degrees:
Bachelor of Science, Earth and Planetary Sciences, 2008
University of New Mexico, Albuquerque

Thesis Title: Microstructural Characterization of Kinked Germanate Olivine Grains

Thesis Examination Committee:
Chairperson, Pamela Burnley, Ph.D.
Committee Member, Michael Wells, Ph.D.
Committee Member, Sean Mulcahy, Ph.D.
Graduate Faculty Representative, Andrew Cornelius, Ph.D.